

AD-A235 713



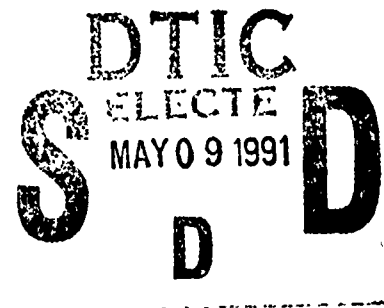
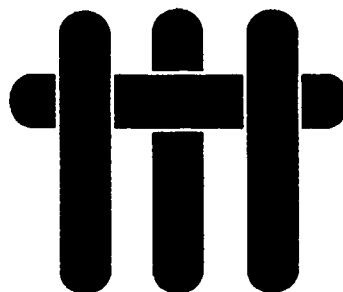
2

**ANNUAL REPORT**  
**Office of Naval Research**

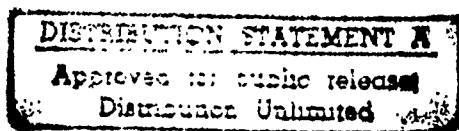
Contract No.: N00014-89-J-1764

March 15, 1989 - March 15, 1991

**M A T E R I A L S**



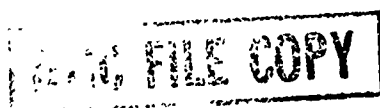
**METAL/CERAMIC INTERFACES:  
RELATIONSHIPS BETWEEN STRUCTURES,  
CHEMISTRY AND INTERFACES**



by

A. G. Evans  
Materials Department  
College of Engineering  
University of California  
Santa Barbara, California 93106

Sponsored by: Office Of Naval Research



91 4 30 059

REPORT DOCUMENTATION PAGE			Form Approved OMB No. 0705-0188	
1. AGENCY USE ONLY (Leave blank)		2. REPORT DATE  030191	3. REPORT TYPE AND DATES COVERED  ANNUAL REPORT 3/1/89-3/1/91	
4. TITLE AND SUBTITLE  "METAL/CERAMIC INTERFACES: RELATIONSHIPS BETWEEN STRUCTURE, CHEMISTRY AND INTERFACES"			5. FUNDING NUMBERS  N00014-89-J-1764	
6. AUTHOR(S)  A. G. EVANS				
7. PERFORMING ORGANIZATION NAME(S) AND ADDRESS(ES)  MATERIALS DEPARTMENT COLLEGE OF ENGINEERING UNIVERSITY OF CALIFORNIA SANTA BARBARA, CA 93106			8. PERFORMING ORGANIZATION REPORT NUMBER	
9. SPONSORING/MONITORING AGENCY NAME(S) AND ADDRESS(ES)  OFFICE OF NAVAL RESEARCH MATERIALS DIVISION 800 NORTH QUINCY STREET ARLINGTON, VA 22217-5000			10. SPONSORING/MONITORING AGENCY REPORT NUMBER	
11. SUPPLEMENTARY NOTES				
12A. DISTRIBUTION/AVAILABILITY STATEMENT			12B. DISTRIBUTION CODE	
13. ABSTRACT (Maximum 300 words)  SEE ATTACHED EXECUTIVE SUMMARY				
14. SUBJECT TERMS  METAL/CERAMIC BONDS, INTERMETALLIC INTERFACES, MATRIX COMPOSITES, PLASTICITY, CRACK PROPAGATION			15. NUMBER OF PAGES  130	
			16. PRICE CODE	
17. SECURITY CLASSIFICATION OF REPORT  UNCLASSIFIED	18. SECURITY CLASSIFICATION OF THIS PAGE  UNCLASSIFIED	19. SECURITY CLASSIFICATION OF ABSTRACT  UNCLASSIFIED	20. LIMITATION OF ABSTRACT	

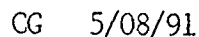
91 4 30 059

## **EXECUTIVE SUMMARY**

	<b><u>TITLE</u></b>	<b><u>AUTHOR</u></b>
Article 1.	Residual Stress Cracking of Metal Ceramic Bonds	A. G. Evans A. Bartlett
Article 2.	The Strength and Fracture of Metal/Ceramic Bonds	A. G. Evans M. Y. He
Article 3.	The Fracture Resistance of Model Metal/Ceramic Interface	A. G. Evans I. E. Reimanis
Article 4.	The Fracture Resistance of Metal/Ceramic/Intermetallic Interfaces	A. G. Evans A. Bartlett J. B. Davis B. D. Flinn M. Turner I. E. Reimanis
Article 5.	Powder Processing of Ceramic Matrix Composites	A. G. Evans F. F. Lange D. C. Lam O. Sudre B. D. Flinn C. Folsom B. V. Velamakanni F. W. Zok
Article. 6.	Effects of Plasticity of the Crack Propagation Resistance of a Metal/Ceramic Interface	A. G. Evans I. E. Reimanis B. J. Dalgleish M. Brahy M. Rühle

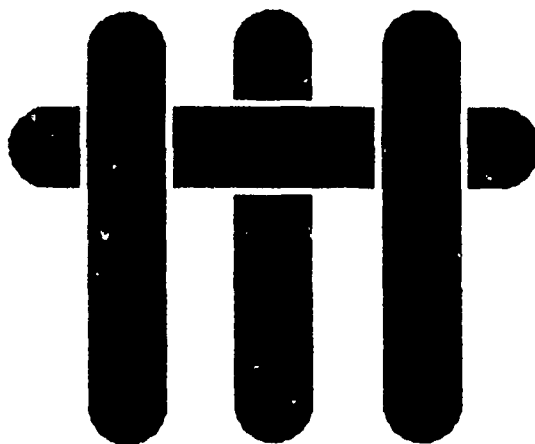
1. The first step in the process of creating a new product is to identify a market need. This involves conducting market research to understand what consumers want and what problems they are facing. Once a need is identified, the next step is to develop a concept that addresses that need. This is often done through brainstorming sessions with a team of designers and engineers. The concept is then refined through prototyping and testing, with feedback from potential users being used to make improvements. Finally, the product is launched into the market, and its success is monitored through sales data and customer feedback.

Stress corrosion has been found to occur at oxide/metal interfaces, leading to substantial reductions in the fracture resistance. The phenomenon is governed by water vapor and is similar to, but more pronounced than, that found in oxides.



Approved For		J
Date: 01-01-84		J
Class: 1000		21
Under the Code		21
Justification		
By		
Distribution/		
Availability Codes		
Dist	Avail and/or Special	
A-1		

M A T E R I A L S



**RESIDUAL STRESS CRACKING  
OF METAL/CERAMIC BONDS**

by

A. Bartlett and A. G. Evans

Materials Department  
College of Engineering  
University of California  
Santa Barbara, California 93106

and

M. Rühle

Max Planck Institut für Metallforschung  
Stuttgart, Germany

## ABSTRACT

Metal/ceramic bonds subject to residual stress caused by thermal expansion misfit have been investigated in an  $\text{Al}_2\text{O}_3/\text{Ta}(\text{Ti})$  system. The residual stresses cause cracking of either the  $\text{Al}_2\text{O}_3$  or the interface, dependent on the magnitude and sign of the residual stress. The observed locations, orientations, and trajectories of the cracks have been rationalized on the basis of residual stress fields, energy release rates and fracture energies for the ceramic and the interface.

### 1. INTRODUCTION

Most metal/ceramic bonds are subject to residual stress. This stress can cause cracking of either the ceramic or the interface. The residual stresses may also degrade the mechanical strength of the bonded system. Some aspects of residual stress induced cracking have been analyzed previously,<sup>1,2,3</sup> but a comprehensive description of this phenomenon has not yet been presented. The intent of the present investigation is the experimental characterization of cracking and correlation with the results of stress analysis and of fracture mechanics.

A model system consisting of sapphire diffusion bonded to Ta(Ti) alloys is used for the experimental study. This system has several attributes. The alloy compositions used in this study (20-50% Ti) show solid solubility, such that the coefficient of thermal expansion,  $\alpha$ , can be continuously varied between  $\approx 10 \times 10^{-6} \text{ K}^{-1}$  (pure Ti) to  $\approx 7 \times 10^{-6} \text{ K}^{-1}$  (pure Ta), compared with  $\approx 8 \times 10^{-6} \text{ K}^{-1}$  for sapphire.\* Consequently, alloys can be prepared that have either smaller or larger thermal expansions than sapphire. It will be shown that a

---

\* The coefficient of thermal expansion is a function of temperature.

second advantage of this system is that a thin multiphase reaction product layer forms during diffusion bonding having composition relatively insensitive to the original alloy composition within the range of interest. The "interface" thus has relatively consistent mechanical characteristics.

The fracture behavior can be rationalized by invoking various solutions for residual stresses and for stress intensity factors associated with bonds. To facilitate interpretation, it is also noted that, within homogeneous brittle solids, crack propagation occurs along a trajectory in which the mode II stress intensity factor,  $K_{II}$ , is zero.<sup>4,5</sup> However, cracks on interfaces can extend subject to mixed mode conditions with fracture energy  $\Gamma_i$  influenced by the phase angle,  $\psi$ .<sup>6,7</sup>

## 2. EXPERIMENTS

### 2.1 Diffusion Bonding

Sapphire discs having random orientation were mechanically polished to provide surfaces with good planarity. Foils of Ta(Ti) alloy 0.8 - 1.9 mm thick were placed between two of the sapphire discs and located within a compression loading fixture in a vacuum furnace. A normal compression of 3-5 MPa was applied and the system heated to 1100°C, held at that temperature for 1/2 hour and cooled at a rate of 5°C/min. Both symmetric and asymmetric specimens were produced (Fig. 1).

### 2.2 Interface Properties

In all bonds, reaction products were formed, as elaborated elsewhere<sup>8</sup> and summarized here. In general, three distinct reaction products formed, as established by cross-section TEM. A PEELS spectrum revealed that *within detectable limits* ( $\approx 5\%$ ) no oxygen was present in any of the reaction products (Fig. 2).

Consequently, use of a preliminary Ta-Ti-Al ternary phase diagram<sup>9</sup> (Fig. 3) suggests that the phases are:  $\gamma$ ,  $\alpha_2$ , and  $\sigma$ . Electron diffraction results (Fig. 4) combined with EDS and with lattice parameters obtained from X-Ray data confirm the identity of these phases.

Asymmetric specimens with one thin layer of sapphire allowed measurement of the interface fracture energy.<sup>10-12</sup> Alloy compositions giving zero residual stress were chosen in order to simplify measurements. These samples were prepared by careful diamond sawing of the diffusion bonded discs into flexural beams having dimension  $\sim 28 \times 1 \times 1$  mm. A precrack was introduced into the thin sapphire layer using a Knoop indenter. Thereafter, loading in three-point bending extended the precrack to the interface. Subsequent fracture energy measurements on the precracked specimens were conducted in four-point bending.<sup>10,11</sup> *In situ* testing in the SEM allowed detailed observations of crack evolution. These observations revealed that the precrack propagated unstably through the sapphire and reaction product layers and then arrested at the reaction product/alloy interface, accompanied by blunting (Fig. 5a). Upon subsequent loading the crack extended along the sapphire/reaction product interface. In addition, periodic branch cracks were observed in the reaction layer (Fig. 5b). The load at which the crack extended gave a fracture energy for the interface between the sapphire and reaction layer,  $\Gamma_i = 17 \pm 3 \text{ Jm}^{-2}$  ( $\psi \approx 50^\circ$ ). For comparison, the fracture energy of the  $\sigma$ -phase reaction product<sup>13</sup>  $\Gamma \approx 40 \text{ Jm}^{-2}$ , and that for sapphire on non-basal planes<sup>14</sup>  $\Gamma \approx 12 \text{ Jm}^{-2}$ .

### 2.3 Cracking Observations

A general observation is that positive misfit systems ( $\alpha_{\text{alloy}} > \alpha_{\text{Al}_2\text{O}_3}$  made with alloys having  $< 67$  at.% Ta at  $1100^\circ\text{C}$ ) crack predominantly within the sapphire,



although the details depend on sample geometry and history. Conversely, systems subject to negative misfit ( $\alpha_{\text{alloy}} < \alpha_{\text{Al}_2\text{O}_3}$ ) crack along the interface. Systems with *positive* misfit when inspected with light microscopy revealed continuous *perimeter cracks* with no sign of internal cracking. In order to observe the trajectory of these cracks in detail, the samples were sectioned, polished and characterized by SEM, revealing the morphology detailed in Fig 6. (The bonding geometry was such that the sapphire extended beyond the edge of the metal.) Crack initiation did not occur at the ceramic/metal interface, but instead *nucleated in the ceramic* at a distance  $\approx 15 \mu\text{m}$  from the interface. The crack angle  $\phi$  with respect to the interface was consistently in the range  $62\text{--}64^\circ$ . Following initiation, the cracks curved in a continuous trajectory, turning parallel to the interface at a distance on the order of the metal layer thickness, before arresting.

Sectioning and polishing led to additional cracking having the features illustrated in Fig. 6. Two types of cracks were present. Periodic small *zone cracks* were apparent near the interface (within  $10 \mu\text{m}$ ), but did not extend into the reaction product layer. The initial inclination  $\phi$  of these cracks decreased with distance from the specimen edge. *Edge cracks* occurred in the ceramic parallel to the interface at distances of  $50\text{--}100 \mu\text{m}$  from the interface and extended almost continuously over the cross-section. Further sectioning and polishing revealed that these cracks, which are traces of new perimeter cracks, formed at the new surface introduced by sectioning and initiated at a "stand off" distance from the interface  $\approx 50 \mu\text{m}$ .

For systems having *negative* misfit (misfit strain,  $\epsilon_T \approx 5 \times 10^{-4}$ ) no cracking was observed in the as-cooled samples. However, sectioning introduced flaws that, in some cases, initiated visible cracks. These cracks formed near the edge and propagated *along both interfaces* (Fig. 7). *No cracking was observed in the ceramic.* The cracks propagate on a variety of interface paths: within the reaction product

layer, along the reaction product/sapphire interface, and along the reaction product/alloy interface.

### 3. SOME RELATED MECHANICS

Information about the *initiation* of cracks can be gained from the principal tensile stress. Crack *trajectories* are addressed by evaluation of the crack path along which the mode II stress intensity factor is zero. The stress field information<sup>1,15</sup> is summarized in Fig. 8. In the ceramic close to the interface, the *principal tensile stress* is essentially normal to the interface near the center but around the perimeter is inclined at  $\beta \approx 30^\circ$ . Along the periphery, the principal stresses are tensile within a narrow boundary layer near the interface. This stress is high but the stress gradient is also large. A crack in this layer experiences an energy release rate  $\mathcal{G}$  that reflects both the stress amplitude and gradient (Fig. 9). Consequently,  $\mathcal{G}$  exhibits a maximum at a characteristic stand-off distance proportional to the metal layer thickness.

When cracks develop into a length comparable to a characteristic specimen dimension (such as either the metal or ceramic layer thickness) interaction with the boundaries occurs.<sup>4,16,17,19</sup> These interactions tend to deflect the crack into a  $K_{II} \approx 0$  path parallel to the relevant boundary, at a distance proportional to the layer thickness. The most comprehensively analyzed examples involve cracks in a brittle substrate induced by residually stressed thin films.<sup>16,17</sup> The energy release rate  $\mathcal{G}$  for the example of a crack extending along *both* interfaces of a symmetric specimen has the non-dimensional form<sup>1,18</sup>

$$\mathcal{G}/\bar{E}\epsilon_T^2 d = \Omega_c \quad (1)$$

where  $2d$  is the metal layer thickness,  $\epsilon_T$  is the misfit strain,  $\bar{E}$  is a composite modulus and  $\Omega_c$  is a cracking number  $\approx 1$ .

#### 4. ANALYSIS OF CRACKING

The general cracking features can be related to the sign of the misfit strain. *Positive* misfit ( $\alpha_{\text{alloy}} > \alpha_{\text{Al}_2\text{O}_3}$ ) leads to a *negative*  $K_I$  for interfacial edge cracks.<sup>1</sup> Such cracks are thus suppressed and fracture would occur preferentially in the sapphire. Conversely, for *negative* misfit ( $\alpha_{\text{alloy}} < \alpha_{\text{Al}_2\text{O}_3}$ ), edge cracks experience a *positive*  $K_I$  along the interface<sup>1</sup> and interface failure would be encouraged. Further details are sensitive to the overall geometry and the crack location. For *positive* misfit the initiation of the crack in the sapphire reflects the above stress field and energy release rate information. The *perimeter* and *edge* cracks appear to be dominated by the stress in the tensile boundary layer (Fig. 8), whereupon their nucleation at a stand-off distance from the interface is in accordance with energy release rate considerations (Fig. 9). The subsequent extension of these cracks into a trajectory parallel to the interface is consistent with the known characteristics of  $K_{II} = 0$  trajectories.<sup>16,17</sup>

The formation of the *zone* cracks reflects the characteristics of the principal tensile stress in the sapphire, near the interface (Fig. 8). The variation in the orientation of these cracks with distance from the edge is consistent with the principal tensile stress trajectories. However, the absence of such cracking, into the interface is not understood, given the comparable values of the fracture energies of the interface and the sapphire. It is presumed that the  $\sigma_{rr}$  compression in the sapphire near the interface (Fig. 8) prevents the zone cracks from reaching the interface.

For *negative* misfit, the interface near the edge experiences residual tension and cracking would be expected to occur preferentially at the edge. The available energy release for this process, based on Eqn. (1) is  $G \approx 25 \text{ Jm}^{-2}$ . Comparison with the measured value of the interface fracture energy  $\Gamma_i \approx 17 \text{ Jm}^{-2}$ , confirm that this  $G$  is sufficient to induce interface cracks. Undulating cracks paths within the reaction product layer suggest detailed interactions involving elastic mismatch and residual stress due to the presence of the reaction layer.<sup>19</sup>

## 5. CONCLUDING REMARKS

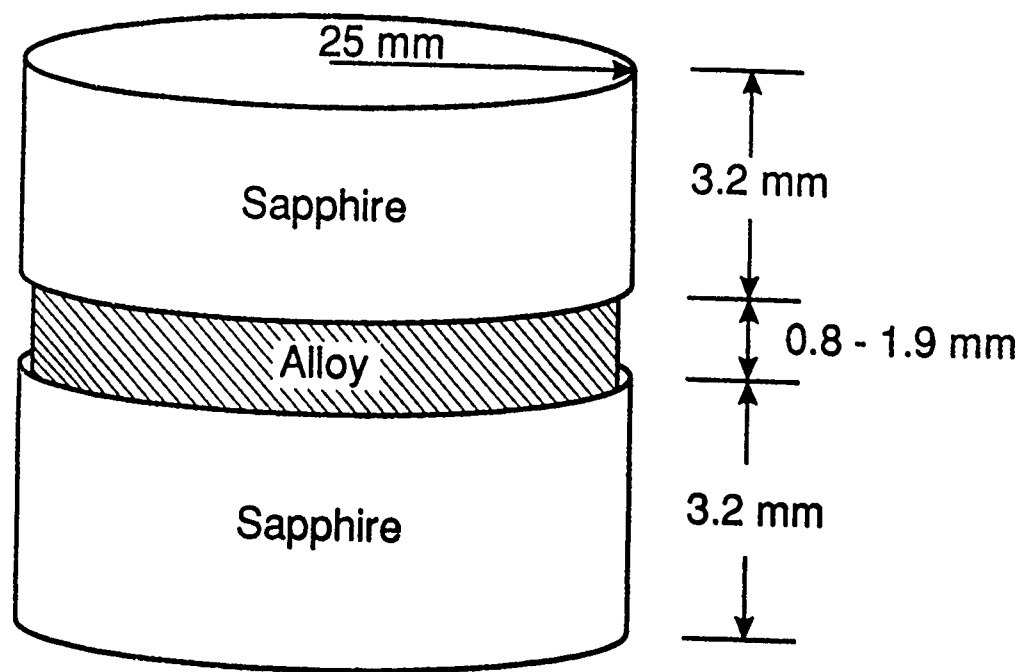
Residual stresses have been shown to lead to cracking of a metal/ceramic bonded system. Systems subject to a positive misfit ( $\alpha_{\text{alloy}} > \alpha_{\text{Al}_2\text{O}_3}$ ) crack in the ceramic, while those with negative misfit ( $\alpha_{\text{alloy}} < \alpha_{\text{Al}_2\text{O}_3}$ ) fail along the interface. Based on information about the residual stress field, as well as the fracture energies of the sapphire and the interface, most of the cracking features have been rationalized. The effects of specimen boundaries on crack trajectories within the sapphire have also been shown to be in agreement with existing understanding.

## REFERENCES

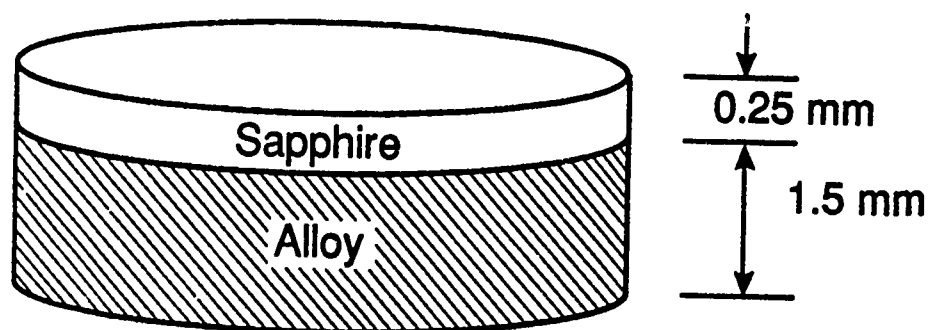
- [1] H. C. Cao, M. D. Thouless and A. G. Evans, *Acta metall.*, **36** (1988) 2037.
- [2] K. Burger, W. Schulte and G. Petzow, *Z Zahnarztl Implantologie*, **4** (1988) 22.
- [3] K. Suganuma, T. Okamoto, M. Koizumi and M. Shimaoa, *J. Am. Ceram. Soc.*, **68** (1985) C334-C335.
- [4] M. D. Thouless, A. G. Evans, M. F. Ashby and J. W. Hutchinson, *Acta Metall.*, **35** (1987) 1333.
- [5] M. D. Drory, M. D. Thouless and A. G. Evans, *Acta Metall.*, **36** (1988) 2019.
- [6] J. R. Rice, *J. Appl. Mech.*, **55** (1988) 98-103.
- [7] J. W. Hutchinson, Metal/Ceramic Interfaces, *Acta/Scripta Metall. Proceedings*, Vol. 4 (Ed. M. Rühle, et al.) Pergamon (1990) p. 295.
- [8] A. Bartlett and A. G. Evans, to be published.
- [9] C. McCullough, J. J. Valencia, C. G. Levi and R. Mehrabian, *Acta Metall.*, to be published.
- [10] P. G. Charalambides, J. Lund, R. M. McMeeking and A. G. Evans, *J. Appl. Mech.*, **111** (1989) 77.
- [11] I. E. Reimanis, B. J. Dalgleish and A. G. Evans, *Acta Metall.*, to be published.
- [12] A. G. Evans, *Acta/Scripta Metall. Proceedings*, Vol. 4 (Ed. M. Rühle et al.) Pergamon (1990) p. 345.
- [13] H. Dève, G. R. Odette, R. Mehrabian, A. G. Evans, R. Emiliani and R. Hecht, *Acta Metall.*, in press.
- [14] S. M. Wiederhorn, *J. Am. Ceram. Soc.*, **52** (1969) 485.
- [15] M. Y. He and A. G. Evans, to be published.
- [16] Z. Suo and J. W. Hutchinson, *Intl. J. Solids and Structures*, **25**, (1989) 1337.
- [17] M. D. Drory and A. G. Evans, *J. Am. Ceram. Soc.*, **73**, (1990) 634.
- [18] Z. Suo, *App. Mech. Rev.*, **43** (1990) 5276.
- [19] N. Fleck, Z. Suo and J. W. Hutchinson, *Intl. Jnl. Solids Structures*, in press.

## FIGURE CAPTIONS

- Fig. 1. Schematic of the geometries used in the experiments.
- Fig. 2. PEELS spectra for the metal and reaction product layers revealing the absence of oxygen *within detectable limits*.
- Fig. 3. Ternary Ti-Ta-Al phase diagram.
- Fig. 4. Calculated and observed electron diffraction pattern: a)  $\gamma$  phase b)  $\alpha_2$  phase c)  $\sigma$  phase.
- Fig. 5. a) A precrack that penetrates the reaction product layer and blunts at the alloy interface.  
b) Crack trajectory when testing to obtain the fracture energy: note the periodic branch cracks in the reaction product layer and the roughness of the interface.
- Fig. 6. A summary of cracking patterns observed in the sapphire for systems with positive misfit.
- Fig. 7. Crack in the reaction product layer for a system with negative misfit ( $\epsilon_T \approx 5 \times 10^{-4}$ ).
- Fig. 8. Principal tensile stress fields for a system subject to positive misfit.
- Fig. 9. A schematic of trends in the energy release rate for cracks in the sapphire near the interface. The stand-off distance is given by the location at which  $G$  attains its maximum value.



a) Symmetric geometry



b) Asymmetric geometry

Fig. 1

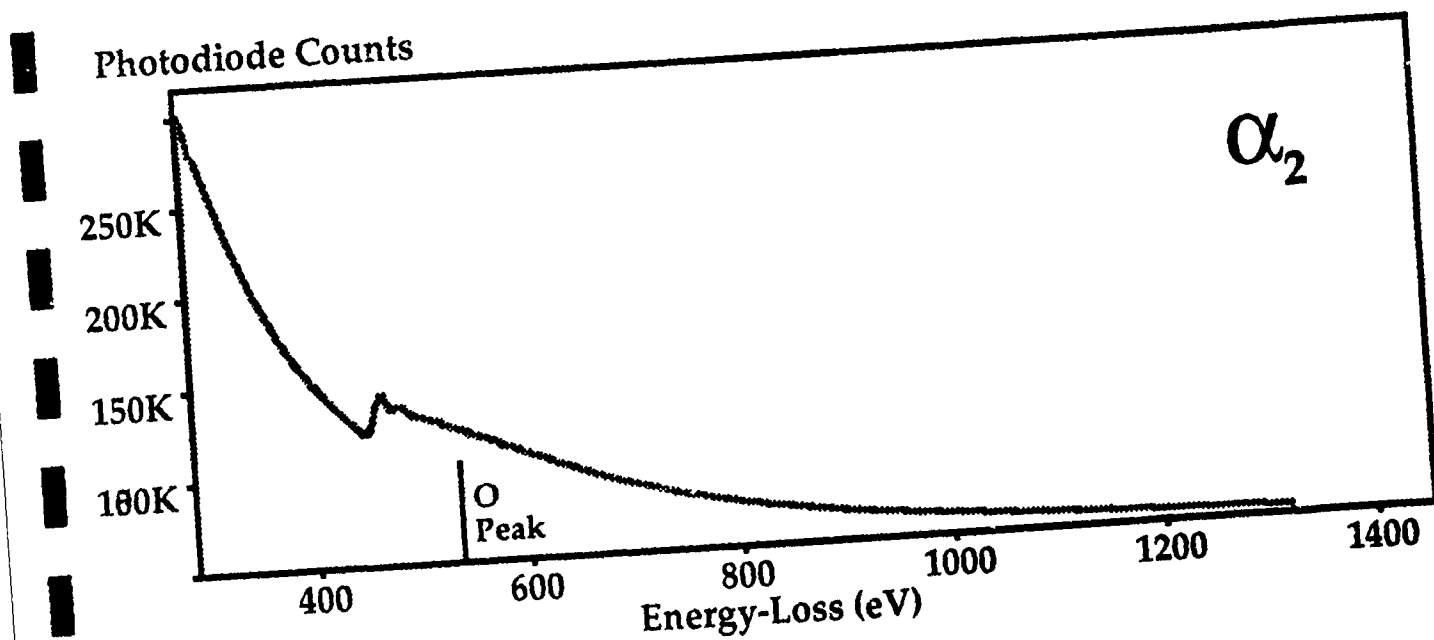
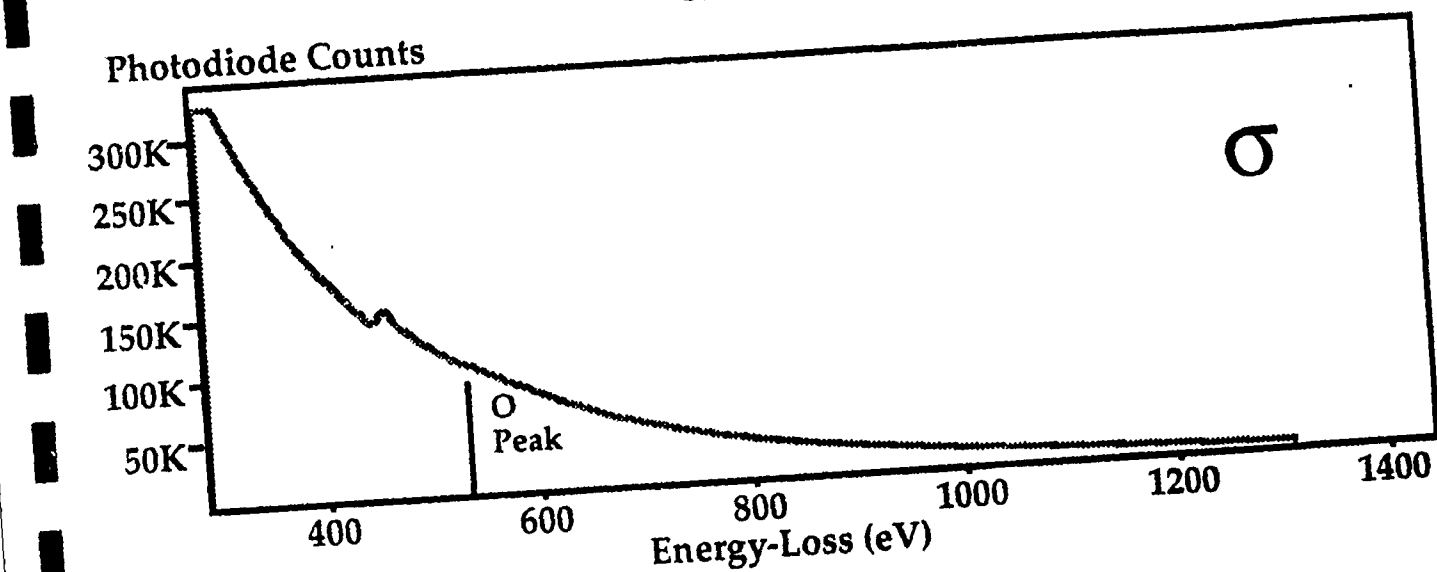
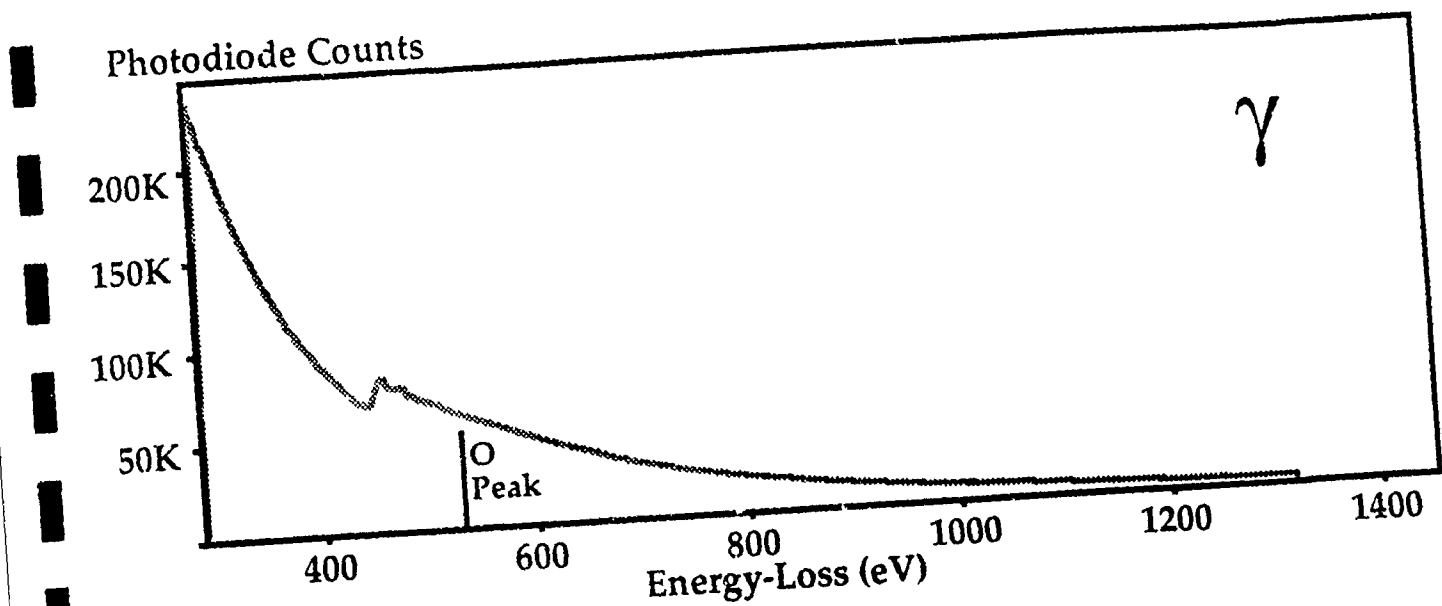


Fig. 2



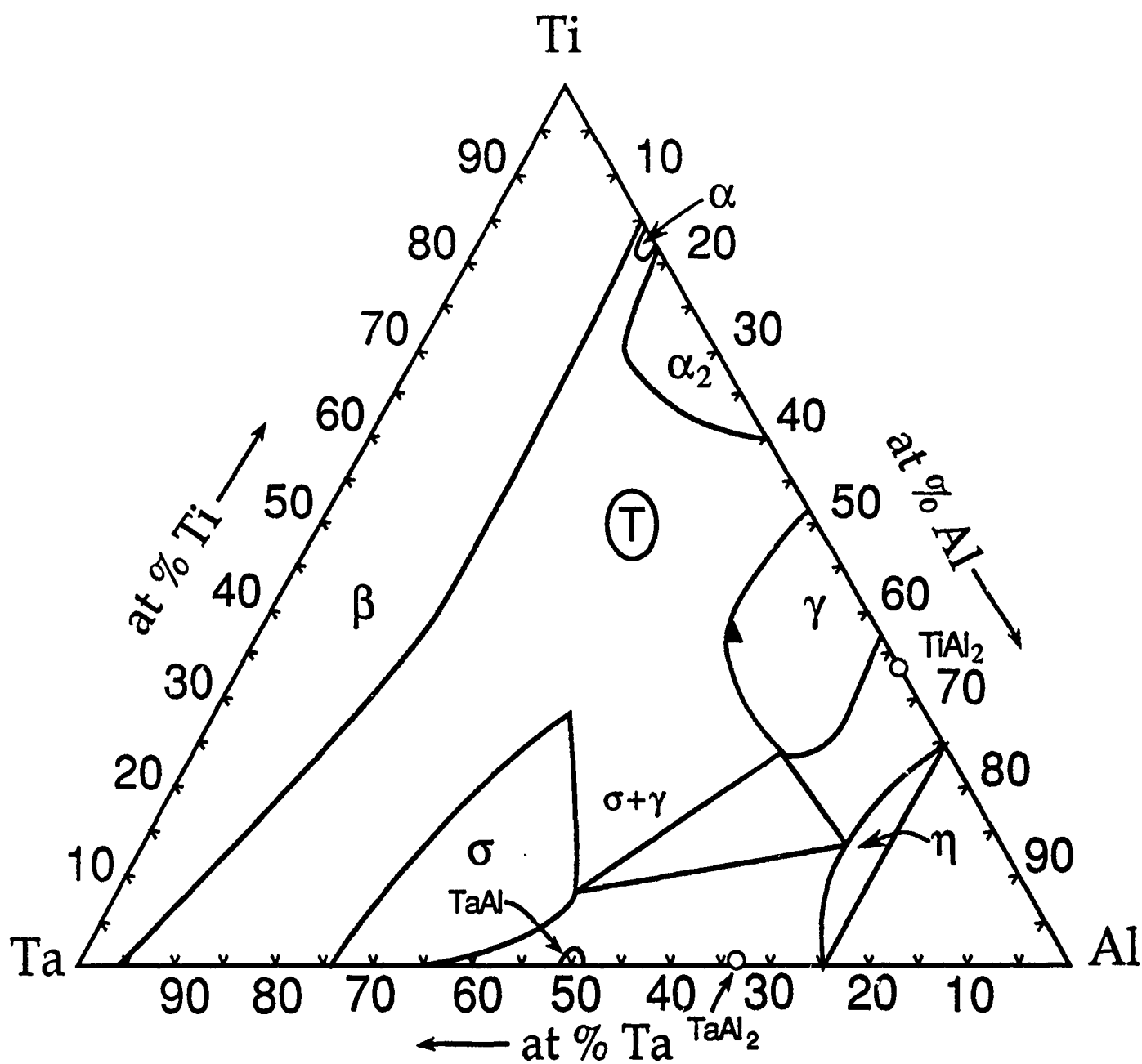
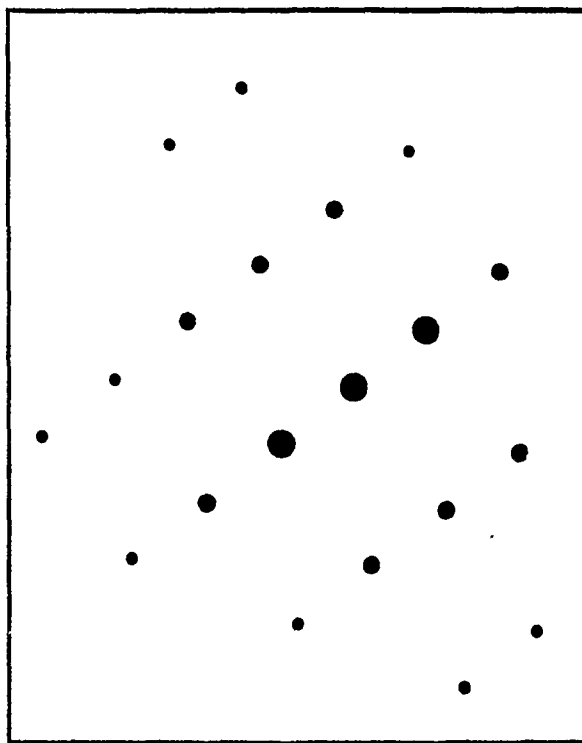


Fig. 3

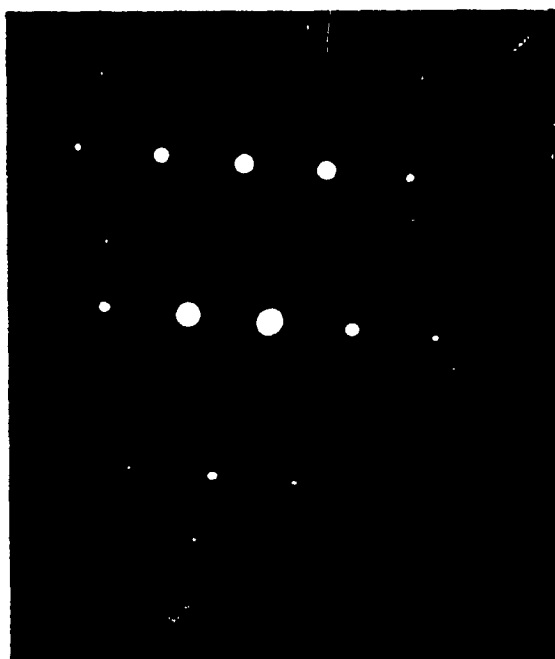


Experimental

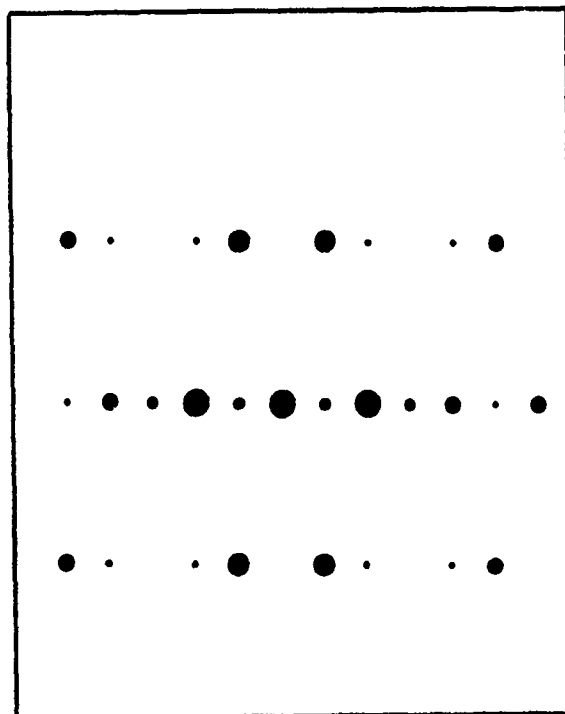


Calculated  $\bar{1}21$  Zone

Fig. 4a



Experimental

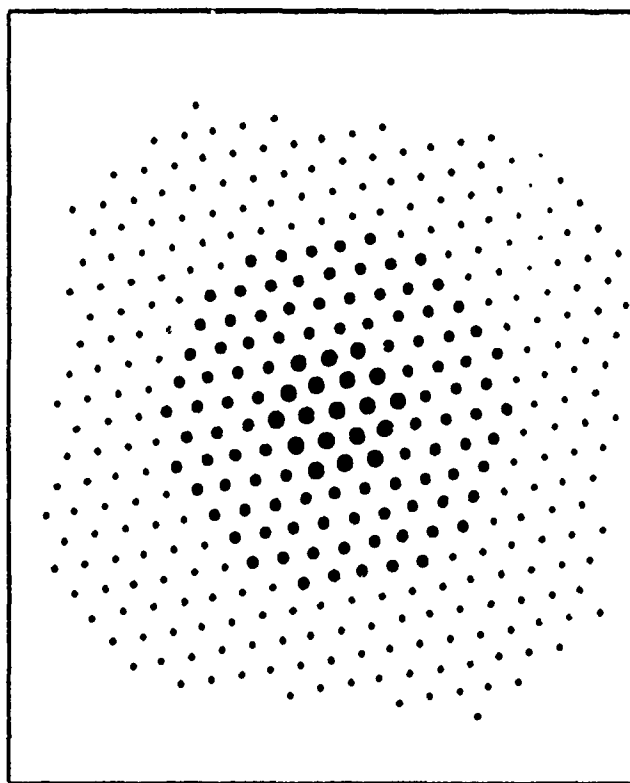


Calculated  $\bar{1}2\bar{1}2$  Zone

Fig. 4b



Experimental



Calculated  $1\bar{1}1$  Zone

Fig. 4c



Fig. 5a

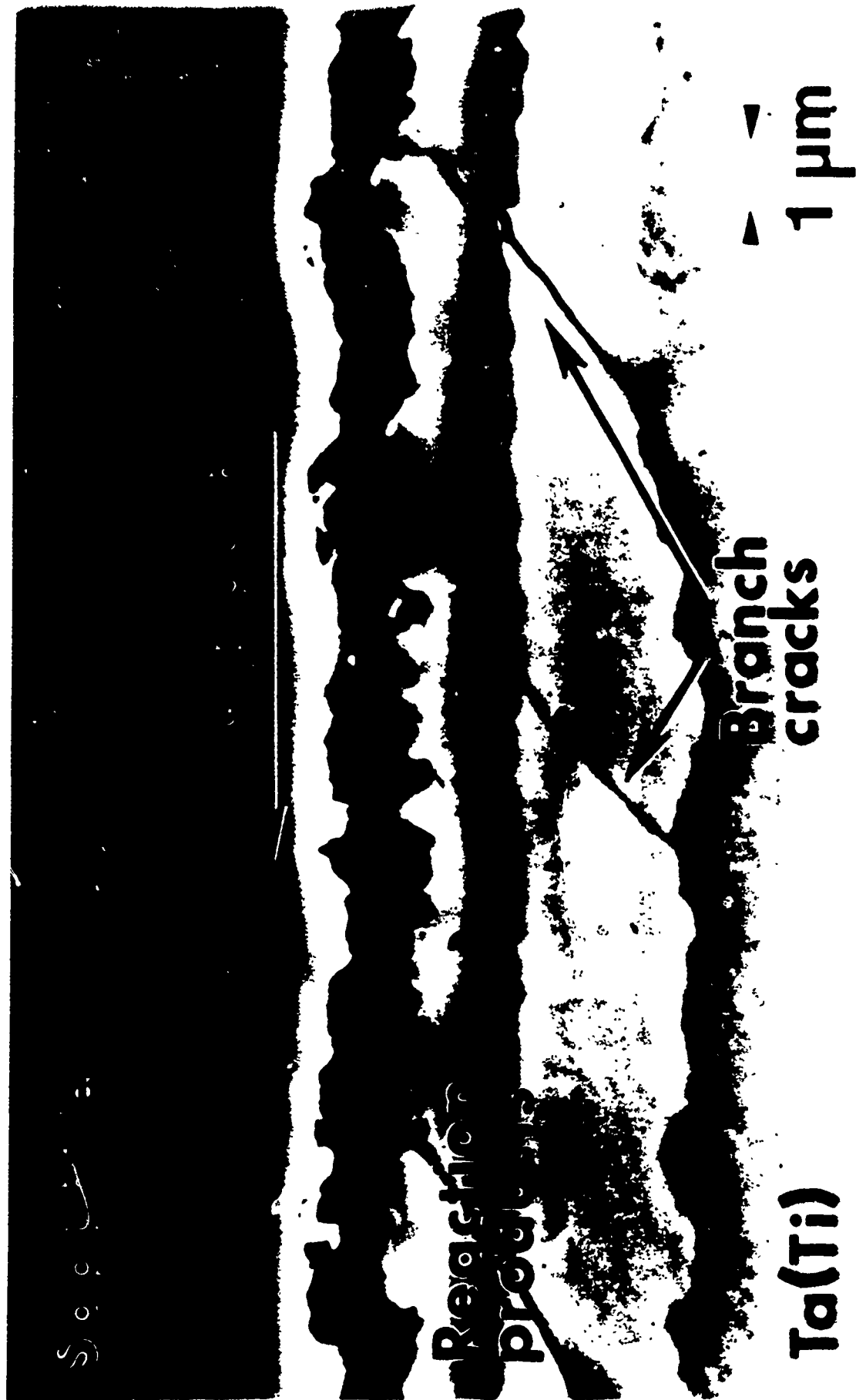
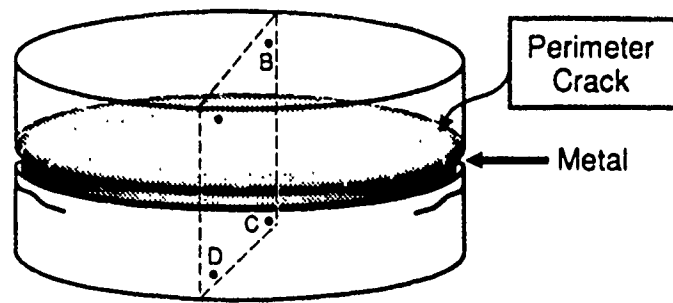
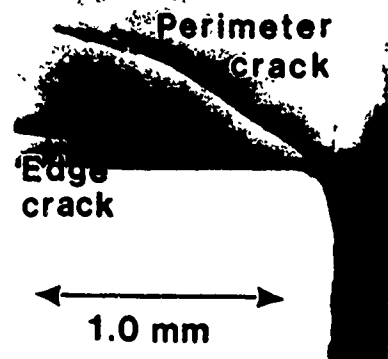
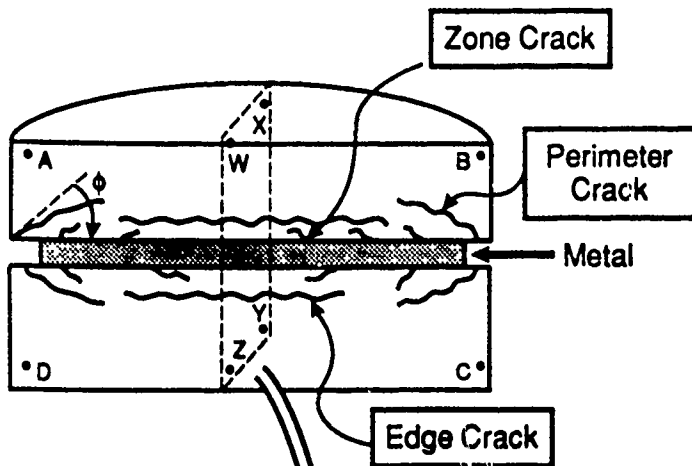


Fig. 5b

a) As - Bonded



b) Center Section



c) Quarter Section

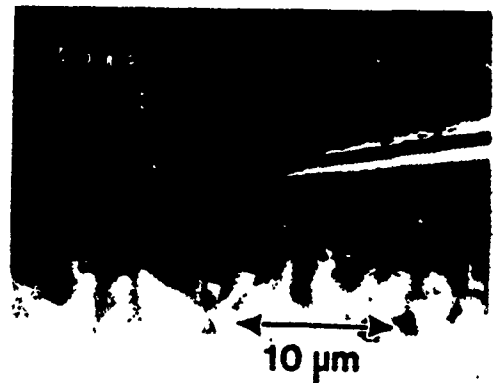
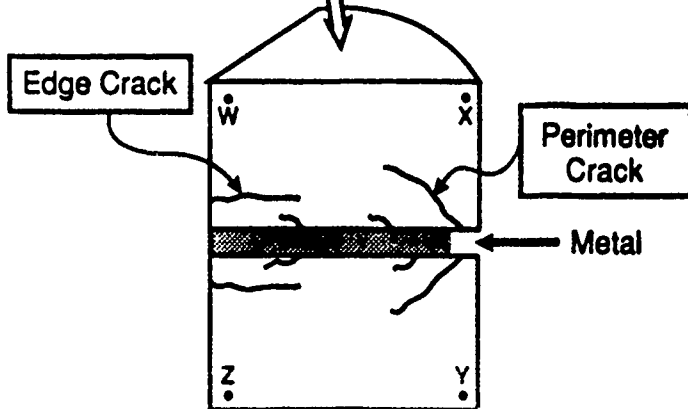


Fig. 6

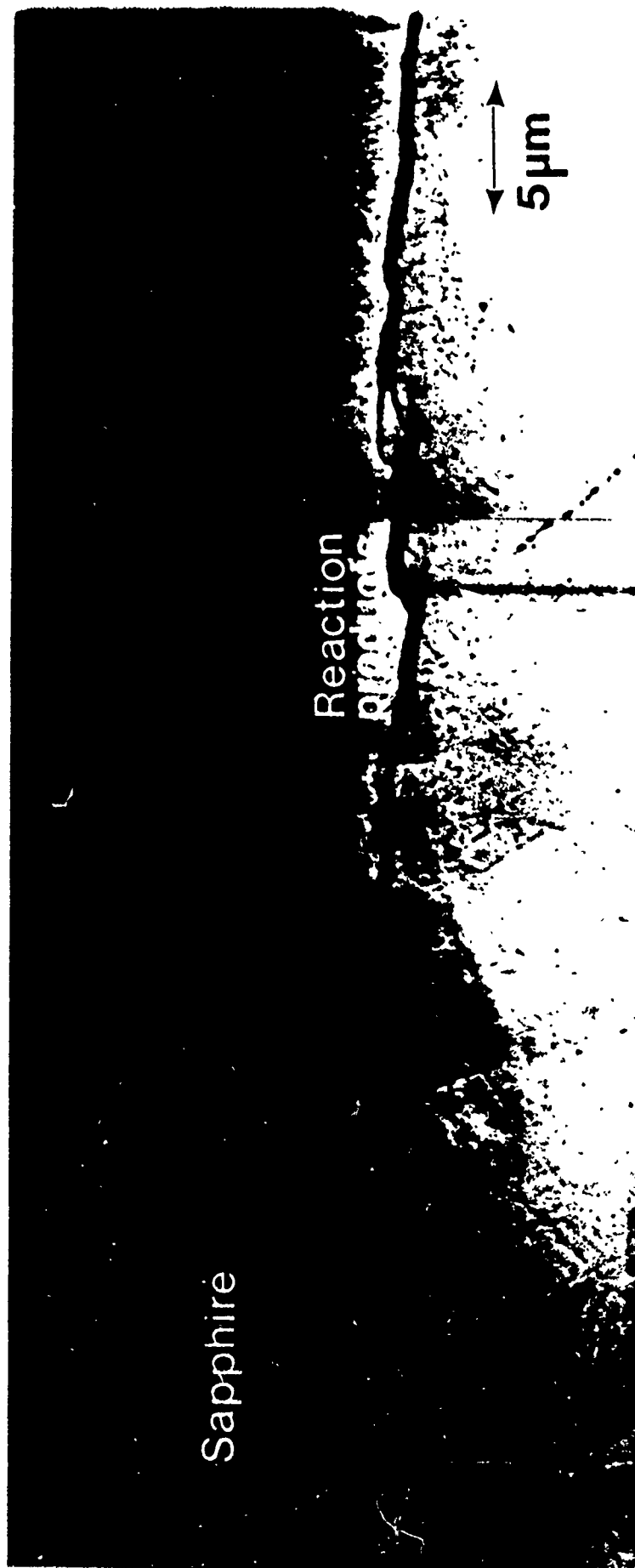


Fig. 7



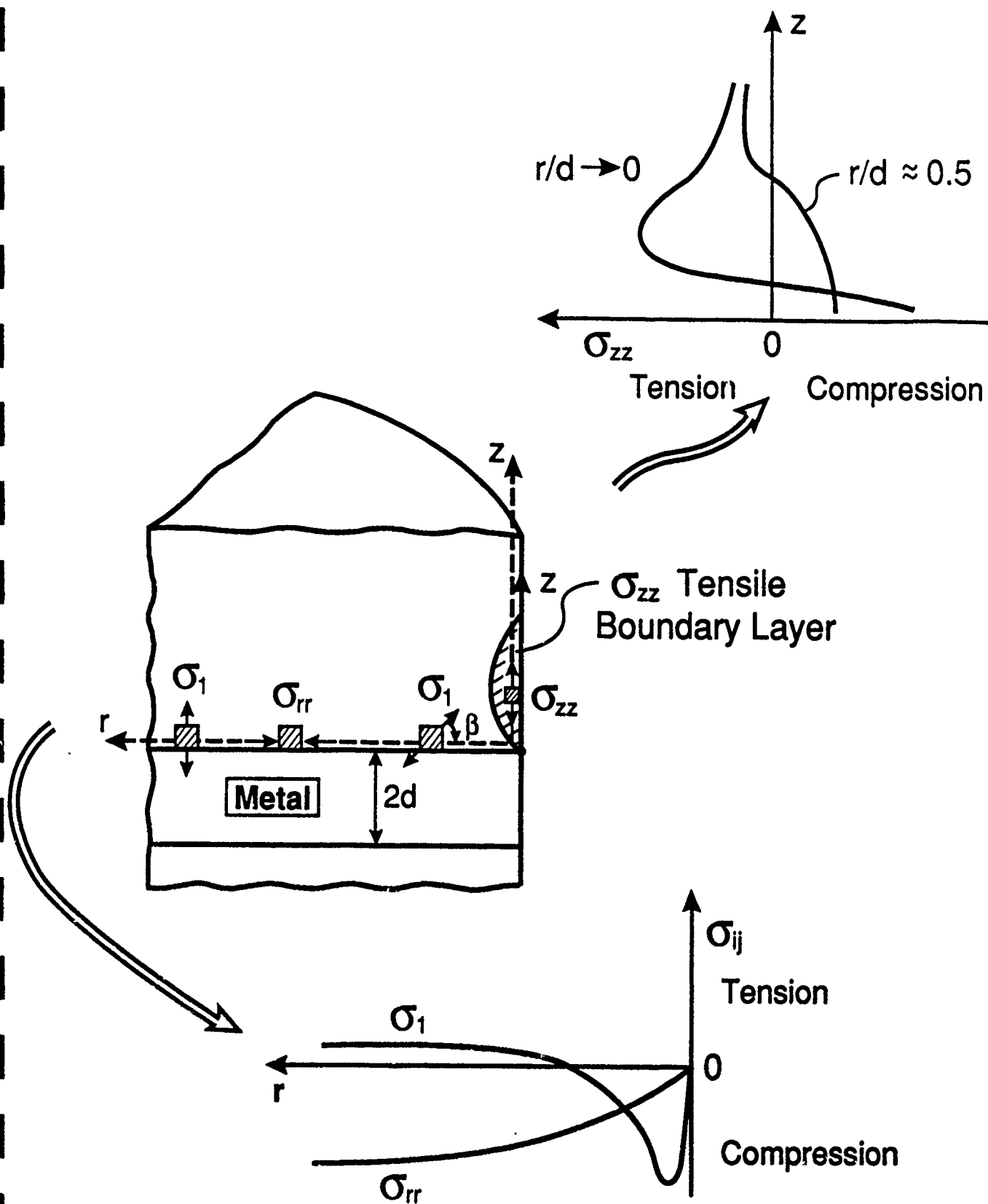


Fig. 8

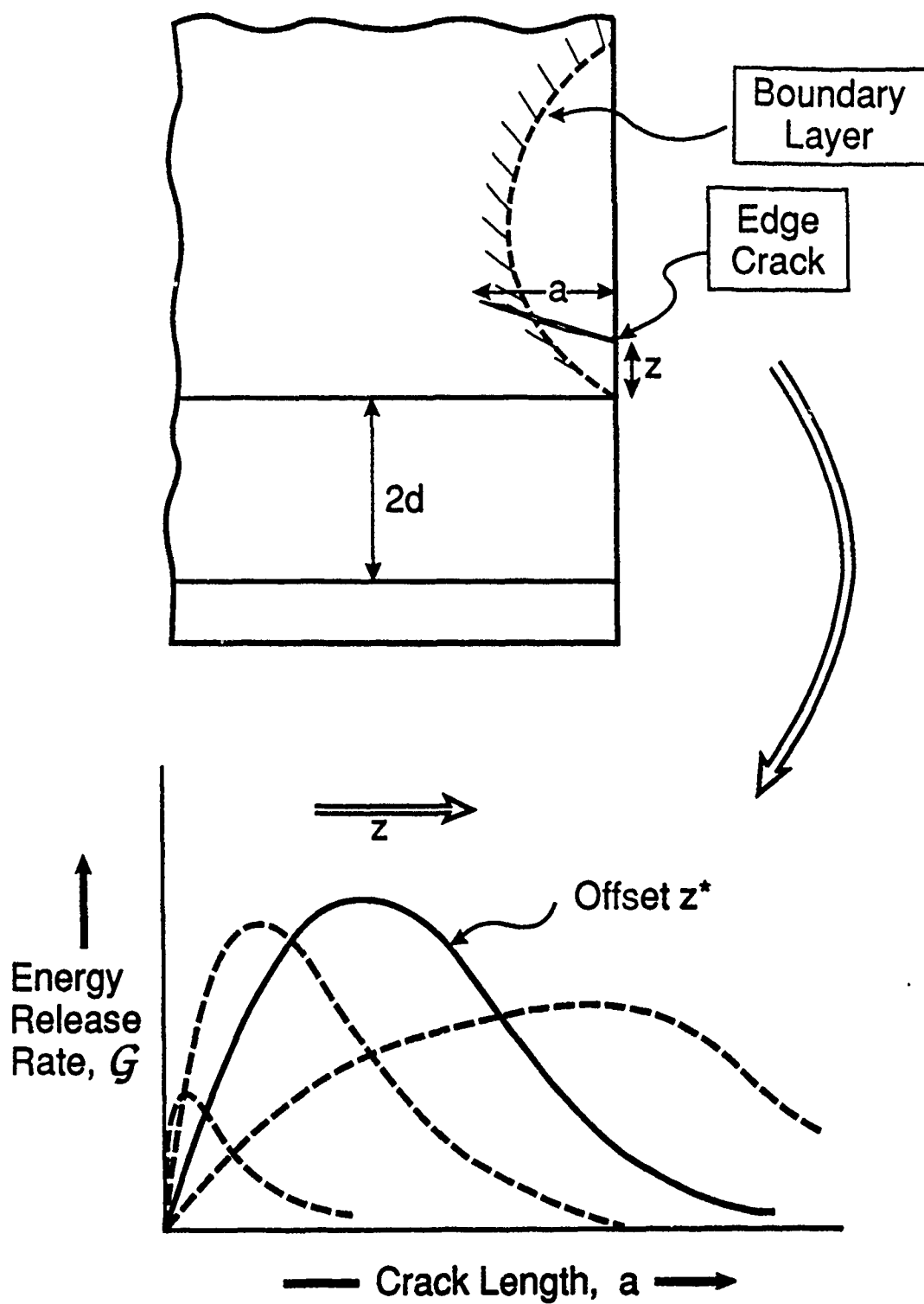
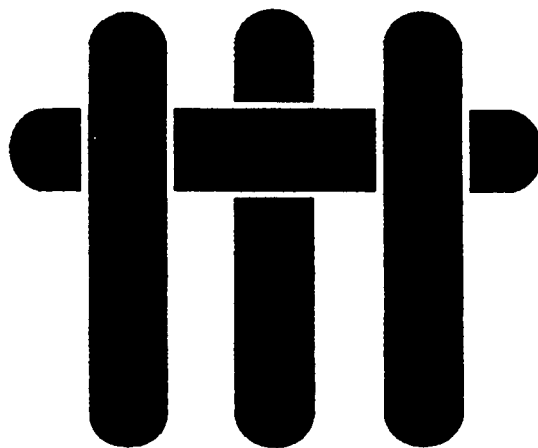


Fig. 9

**M A T E R I A L S**



**THE STRENGTH AND FRACTURE OF  
METAL/CERAMIC BONDS**

by

M. Y. He and A. G. Evans  
Materials Department  
College of Engineering  
University of California  
Santa Barbara, California 93106

Submitted to *Acta Metall. Mater.*, November 1990

## ABSTRACT

The fracture strength of ceramics bonded with metals is limited by the presence of stress concentrations that arise around the bond, especially near edges. Yet, in some cases, fracture can be induced to occur in the ceramic away from the bond. Analysis of the combined effect of elastic mismatch, plasticity and thermal expansion misfit is presented in this paper, to provide understanding of the trends in bond strength. Important influences of plastic relaxation and thermal expansion misfit are identified and some general fracture characteristics are described.

## 1. INTRODUCTION

There are several reported instances in which the fracture of ceramic/metal bonds originates in the ceramic *near the interface*, rather than *at the interface*.<sup>1-4</sup> Such behavior is most likely when i) the bond is relatively thin, such that the limit load is substantially higher than the yield strength of the metal<sup>4</sup> and ii) when the bond is relatively devoid of flaws.<sup>1</sup> When these conditions are achieved, it is of interest to understand the behavior of flaws near the interface. Three important factors are involved in the behavior of these flaws: the mismatch in elastic properties, plastic flow in the metal and residual strain caused by thermal expansion mismatch. Each of these factors is included in the present study. Testing experience indicates that fracture typically originates from flaws near the interface, especially at the edge of the bond. The emphasis of the analysis will thus be on stress concentrations and flaws in this locale. In some cases, fracture occurs in the ceramic well away from the bond, suggesting that stress concentrations can be suppressed when the system has the appropriate properties.

Previous studies have given an indication of some of the salient issues.<sup>1-6</sup> The elastic mismatch causes the energy release rate  $G$  at edge flaws near the interface to become larger than that expected for an elastically homogeneous material.<sup>1,2</sup> This elevation in  $G$  at edge flaws is mitigated by the development of a plastic zone in the metal layer. Residual stress also exerts an influence on fracture and can, indeed, cause fracture in the absence of applied loads. Some aspects of the residual stress have been analyzed,<sup>5,6</sup> but there has been no attempt at *combining the effects of residual and applied loads in the presence of plasticity in the metal*. Analysis of this coupled problem is needed to provide a comprehensive understanding of the overall behavior.

## 2. STATEMENT OF THE PROBLEM

The geometry (Fig. 1) consists of a thin metal bond between two ceramics with a crack in the ceramic near the interface. Initially, the crack is considered to be parallel to the interface, but effects of crack orientation are also addressed. The materials are chosen to have elastic properties representative of many metal/ceramic systems with the Young's modulus  $E$  of the metal being substantially less than that of the ceramic. The metal is considered to yield and work harden such that the uniaxial stress-strain curve satisfies,

$$\varepsilon = \sigma/E + A\varepsilon_0(\sigma/\sigma_0)^n \quad (1)$$

where  $\varepsilon_0$  is the yield strain,  $\sigma_0$  the uniaxial yield strength,  $n$  is a work hardening parameter and  $A$  is a coefficient of order unity. Residual strain in the system is motivated by a mismatch in thermal expansion coefficient, between the metal  $\alpha_2$  and the ceramic,  $\alpha_1$  ( $\Delta\alpha = \alpha_2 - \alpha_1$ ) and a cooling temperature,  $\Delta T$ .

The problem is solved using the following approach. A mismatch strain  $\Delta\alpha\Delta T$  is imposed on the bond to simulate cooling and the resultant development of residual stress calculated. In most cases, the mismatch strain is taken to be sufficiently large compared with the yield strain that the metal has fully yielded during this process. Subsequently, loads are applied and the energy release rate,  $G$ , as well as the phase angle of loading,  $\psi$ , associated with cracks in the ceramic are calculated by finite elements, using the ABAQUS code. The finite element meshes used to conduct the calculations are summarized in Fig. 2. Eight-node biquadratic plane strain elements were used with nine integration points for each element.

### 3. RESULTS

#### 3.1 Stresses for Bonds Without A Crack

The stress field characteristics of interest to the above cracking phenomenon occur in the ceramic either on a plane near the interface (AA' in Fig. 1) or on a plane near the edge (BB' in Fig. 1). The stresses of particular importance are  $\sigma_{yy}$  and  $\sigma_{xy}$ , which govern the mode I and mode II components of the energy release rate. Some preliminary results for a bond without a crack, summarized in Fig. 3, indicate the general trends in  $\sigma_{yy}$  when the expansion misfit is positive ( $\alpha_2 > \alpha_1$ ). In particular, the  $\sigma_{yy}$  residual stresses exhibit a tensile boundary layer in the ceramic along the edge (Fig. 3a). This layer often dominates the formation of *edge* cracks in the ceramic.<sup>7</sup> Under applied loading in the absence of thermal mismatch, contours of this  $\sigma_{yy}$  stress near the interface (Fig. 3b) reveal that a new deformation field becomes established which eventually eliminates the residual field and results in a concentrated  $\sigma_{yy}$  stress near the corner. The explicit effects of yield strain  $\epsilon_0$  and of the mismatch strain,  $\Delta\alpha\Delta T$ , can be expressed through the parameter,

$$\lambda = \Delta\alpha\Delta T/\epsilon_0 \quad (2)$$

Notably, the width of the  $\sigma_{yy}$  tensile boundary layer (Fig. 4) diminishes as  $\lambda$  increases, confirming the beneficial role of yielding (lower  $\epsilon_0$ ) on the tensile residual stresses in the ceramic. These effects are further illustrated from plots of the residual stresses along BB' in the non-dimensional form  $\sigma_{yy}/\sigma_0$  (Fig. 5), which reveal that the stress amplitudes for two substantially different values of  $\lambda$  are similar upon using  $\sigma_0$  as the normalizing stress. Consequently, the magnitudes of the tensile stresses in the boundary layer also *diminish* as the yield strength decreases.

The stress along AA' near the interface which is primarily of interest with regard to cracking in the ceramic is the principal stress  $\sigma_1$ , and its orientation with respect to the interface,  $\phi$ . A plot of the stress (Fig. 6) indicates that it is tensile near the center of the bond and almost normal to the interface. Cracks that form in response to this stress are observed in metal/ceramic bonds.<sup>7</sup>

### 3.2 Energy Release Rates

Aspects of the bond strength manifest in the energy release rate for cracks near the interface are best expressed in terms of the non-dimensional energy release rate,  $G/G_h$ , where  $G_h$  is the energy release rate for homogeneous material (i.e., no bond layer). Furthermore, since only those bonds having high strength are of technological interest, the calculations emphasize stresses  $\sigma/\sigma_0$  in the range 1-6.\* The general trends that have become apparent from the calculations are schematically illustrated in Fig. 7. It is first noted that at small  $\sigma/\sigma_0$ ,  $G/G_h$  increases as  $\sigma/\sigma_0$  increases, followed by a behavior at large  $\sigma/\sigma_0$  wherein  $G/G_h$  then decreases with further increase in the stress. The rising segment is attributed to *elastic mismatch* across the interface which increases the relative elastic energy between the crack and the interface as the stress increases, as indicated by the dotted line in Fig. 7. At larger  $\sigma/\sigma_0$ , the elasticity effect is counteracted by *plasticity* in the metal which, as noted above, tends to suppress the tensile boundary layer in the ceramic near the interface (Figs. 4, 5). Plastic relaxation tends to diminish  $G/G_h$  as  $\sigma/\sigma_0$  increases, as indicated by the second dotted line in Fig. 7. The net effect in the presence of both *elastic mismatch* and *plasticity* is a curve wherein  $G/G_h$  initially increases and then decreases as  $\sigma/\sigma_0$  increases.

---

\* Bonds fail by ductile rupture at stresses  $\sigma \gtrsim 6\sigma_0$ .<sup>8</sup>



The thermal expansion misfit and the relative crack length also have an important influence on  $G/G_h$ . As already noted, positive misfit suppresses the tensile boundary layer and thus, at smaller values of  $\sigma/\sigma_0$ , when the misfit is important,  $G/G_h$  systematically *reduces*, provided that the cracks are relatively long ( $a/h \lesssim 0.1$ ). However, when the cracks are short ( $a/h \lesssim 0.1$ ) and located within the boundary layer, misfit tends to increase  $G/G_h$  at small stresses. Consequently, misfit may have either detrimental or beneficial effects on bond strength, depending on the crack size.

Specific results obtained for  $G/G_h$ , summarized in Figs. 8, 9 and 10, elaborate on these trends. For *short cracks*, it is apparent that *plastic relaxation* is the most important factor (Figs. 8, 9) such that, at high stress level ( $\sigma/\sigma_0 \gtrsim 4-5$ ),  $G$  can be less than  $G_h$  when the dominant flaws in the ceramic are not immediately adjacent to the interface. However, a complete understanding of bond strength and of the benefits of plastic relaxation would require a full statistical analysis in the presence of a distribution of edge flaws near the interface. Conversely, for *large cracks*, expansion misfit has the greatest effect on fracture suppression, such that  $G$  can be less than  $G_h$  at large  $\lambda$ , but only when the stresses are low (Fig. 10). This behavior may be important for *crack arrest* in some cases, such as thermal loading.

Calculations of the phase angle of loading  $\psi$  associated with cracks parallel to the interface (Fig. 11) indicate that, in the absence of misfit, the phase angle is *negative* at all stress levels and the cracks would tend to deviate *toward* the interface. However, for significant positive misfit, the phase angle changes sign and becomes positive, especially at smaller  $\sigma/\sigma_0$ , indicative of a tendency for cracks to direct *away* from the interface, as found experimentally.<sup>7</sup>

The general mixed-mode nature of cracks parallel to the interface suggests that the energy release rate may be larger for edge flaws inclined to the interface. To address this possibility,  $G$  has been calculated for flaws having various inclinations  $\theta$

(Fig. 12), within a range around the  $K_{II} = 0$  plane suggested by the phase angle calculations. The results reveal that  $G$  is relatively orientation insensitive, especially at lower stresses, provided that the crack is defined in terms of the length projected parallel to the interface (Fig. 12).

#### 4. IMPLICATIONS AND CONCLUSIONS

The preceding calculations have the following principal implications for the strength of ceramics bonded with thin metal layers, when the metal has the larger thermal expansion coefficient (positive misfit).<sup>\*</sup> When the interface has a sufficiently high fracture energy that failure does not occur at the interface, the major limitation on the strength concerns stress concentrations in the ceramic near the edge. These stress concentrations arise because of elastic mismatch between the metal and the ceramic. The magnitude of the stress and of the energy release rate at edge flaws is modified by thermal expansion misfit and by plastic relaxation. Two basic behaviors have been identified. For *strong bonds*, wherein the edge *flaws are small* and the *stresses are large*, plastic relaxation effects dominate. Notably, edge failures in the ceramic near the bond can be suppressed by using a metal with a low yield strength. In this regime, expansion misfit effects, although small, are detrimental.

Very different characteristics obtain when the cracks are relatively large and the stress small, as appropriate for the assessment of *crack arrest*, e.g., when the loadings are displacement dominated. In this regime, the energy release rate is diminished by having large (positive) expansion misfit, because of the compressive residual stresses generated near the interface.

---

<sup>\*</sup> Negative misfit induces edge cracking along the interface.<sup>5</sup>

## ACKNOWLEDGEMENT

This work was supported by the DARPA University Research Initiative (Sub agreement P. O. No. UB38639-0 with the University of California, Santa Barbara, ONR Prime Contract No. N00014-86-K-0753). Provision of the ABAQUS finite element code by Hibbitt, Karlsson and Sorensen, Inc. of Providence, Rhode Island is gratefully acknowledged. The calculations on the FPS 500 EA computer were made possible by FPS Computing through the UCSB Industrial Liaison Program.

## REFERENCES

- [1] B. J. Dalgleish, M. C. Lu and A. G. Evans, "The Strength of Ceramics Bonded with Metals," *Acta Metall.*, **36**, 2029 (1988).
- [2] A. G. Evans, M. C. Lu, M. Rühle and S. Schmauder, "Some Aspects of the Mechanical Strength of Ceramic/Metal Bonded Systems," *Acta Metall.*, **34**, 1643 (1986).
- [3] W. Mader and M. Rühle, *Acta Metall.*, **37**, 853 (1989).
- [4] B. J. Dalgleish, K. P. Trumble and A. G. Evans, "The Strength and Fracture of Alumina Bonded with Aluminum Alloys," *Acta Metall.*, **37**, 1923 (1989).
- [5] H. C. Cao, M. D. Thouless and A. G. Evans, "Residual Stresses and Cracking in Brittle Solids Bonded with a Thin Ductile Layer," *Acta Metall.*, **36**, 2037 (1988).
- [6] A. G. Evans, M. Rühle and M. Turwitt, "On the Mechanics of Failure in Ceramic/Metal Bonded Systems," *Journal de Physique*, **C4** (1985) C4-613-C4-625.
- [7] A. Bartlett, M. Rühle and A. G. Evans, "The Effects of Residual Stress On Cracking In Metal/Ceramic Bonds," submitted to *Acta Metall. Mater.*
- [8] V. Tvergaard and J. W. Hutchinson, to be published.

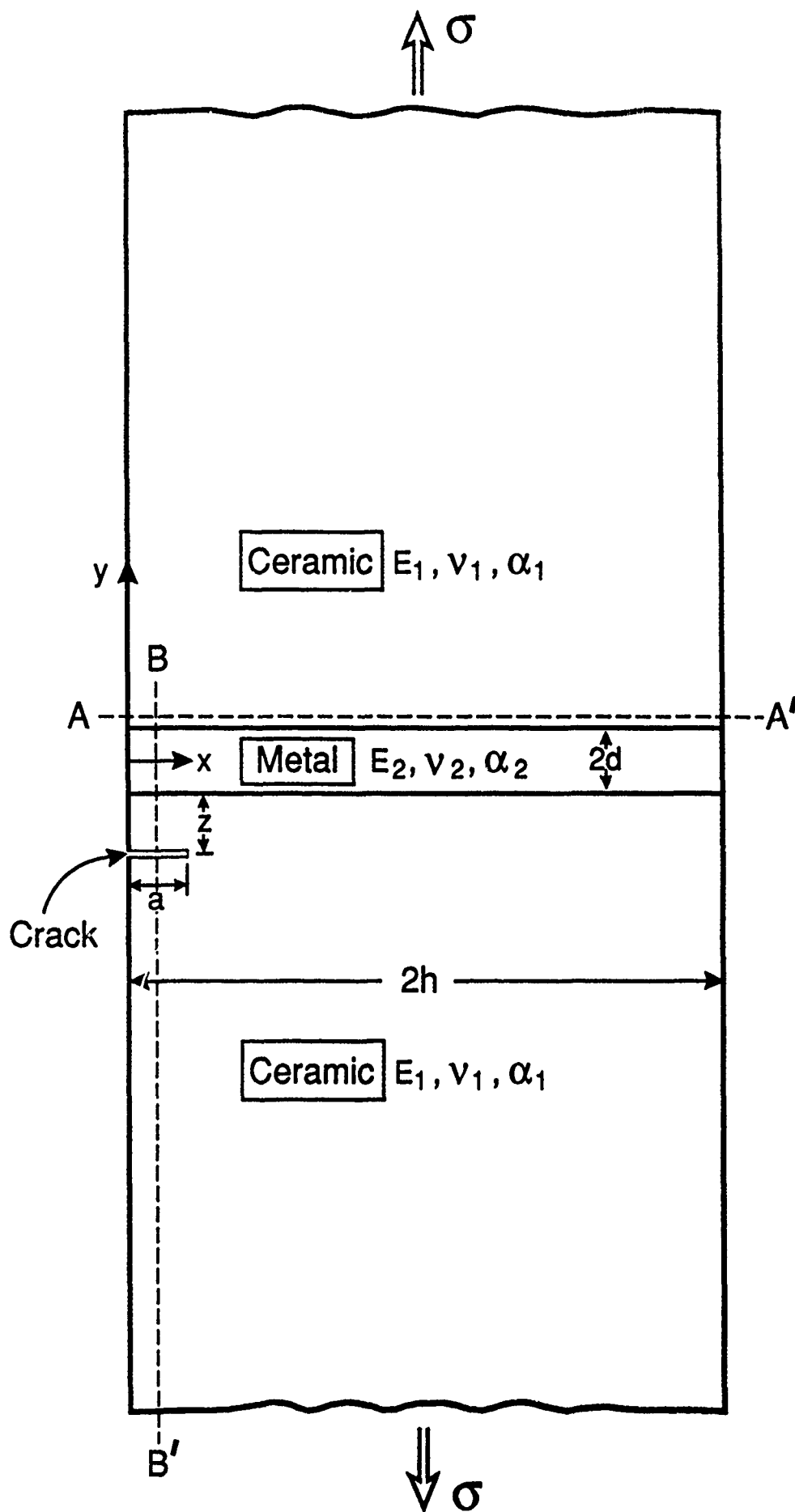


Fig. 1. The thin bond geometry used to conduct the calculations.

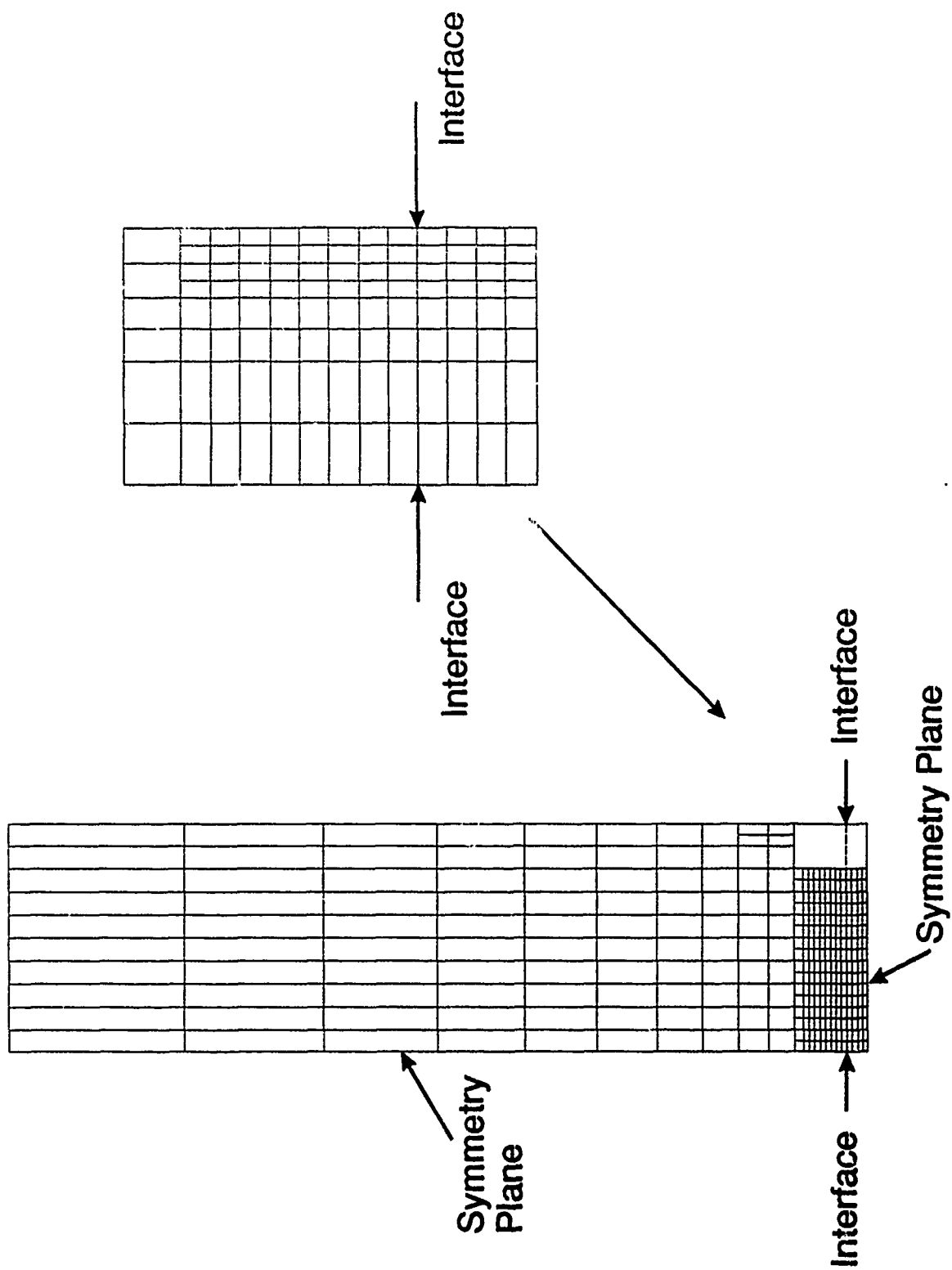


Fig. 2. Typical finite element meshes a) without a crack

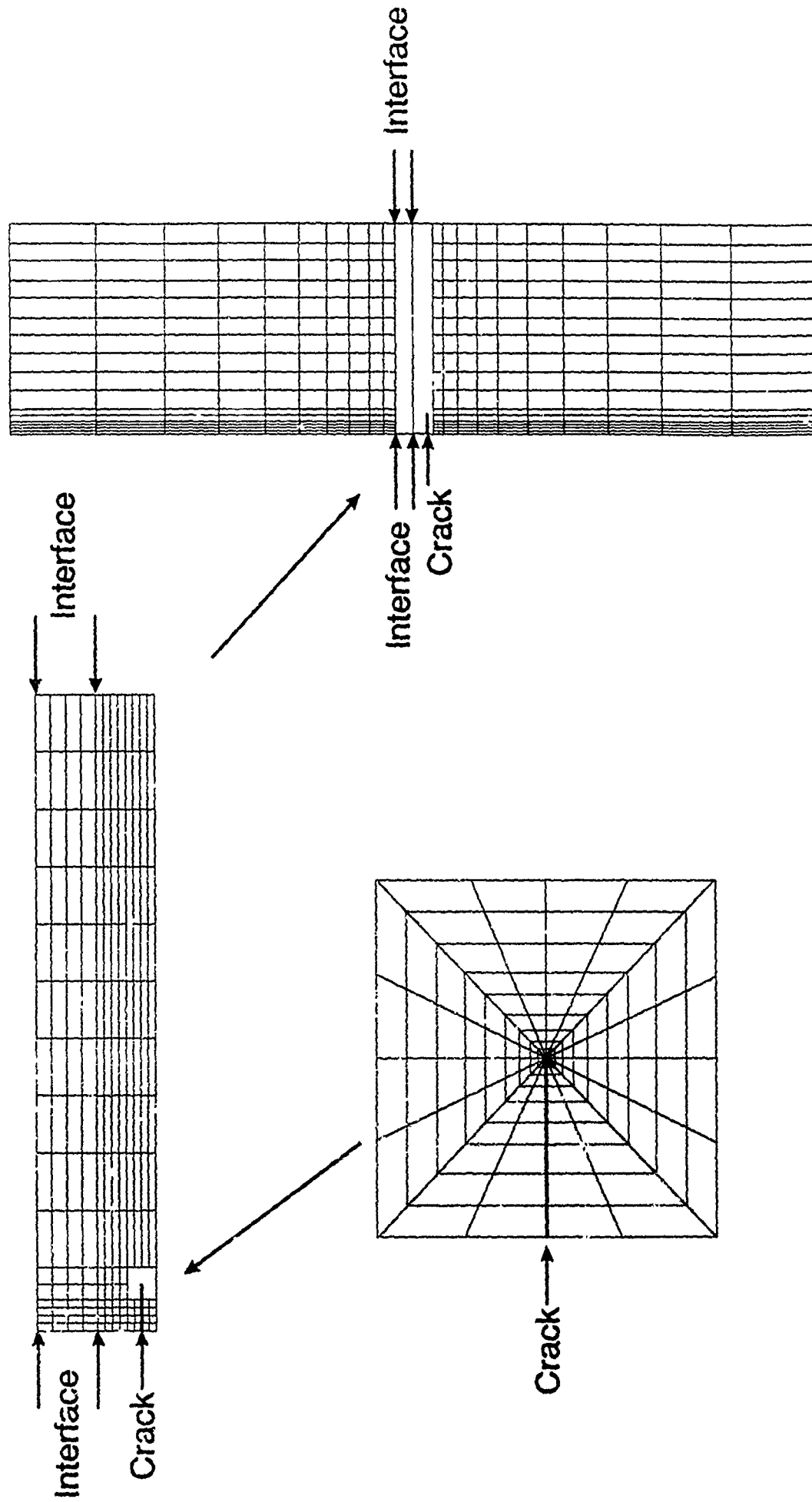


Fig. 2. Typical finite element meshes b) with a crack parallel to the interface

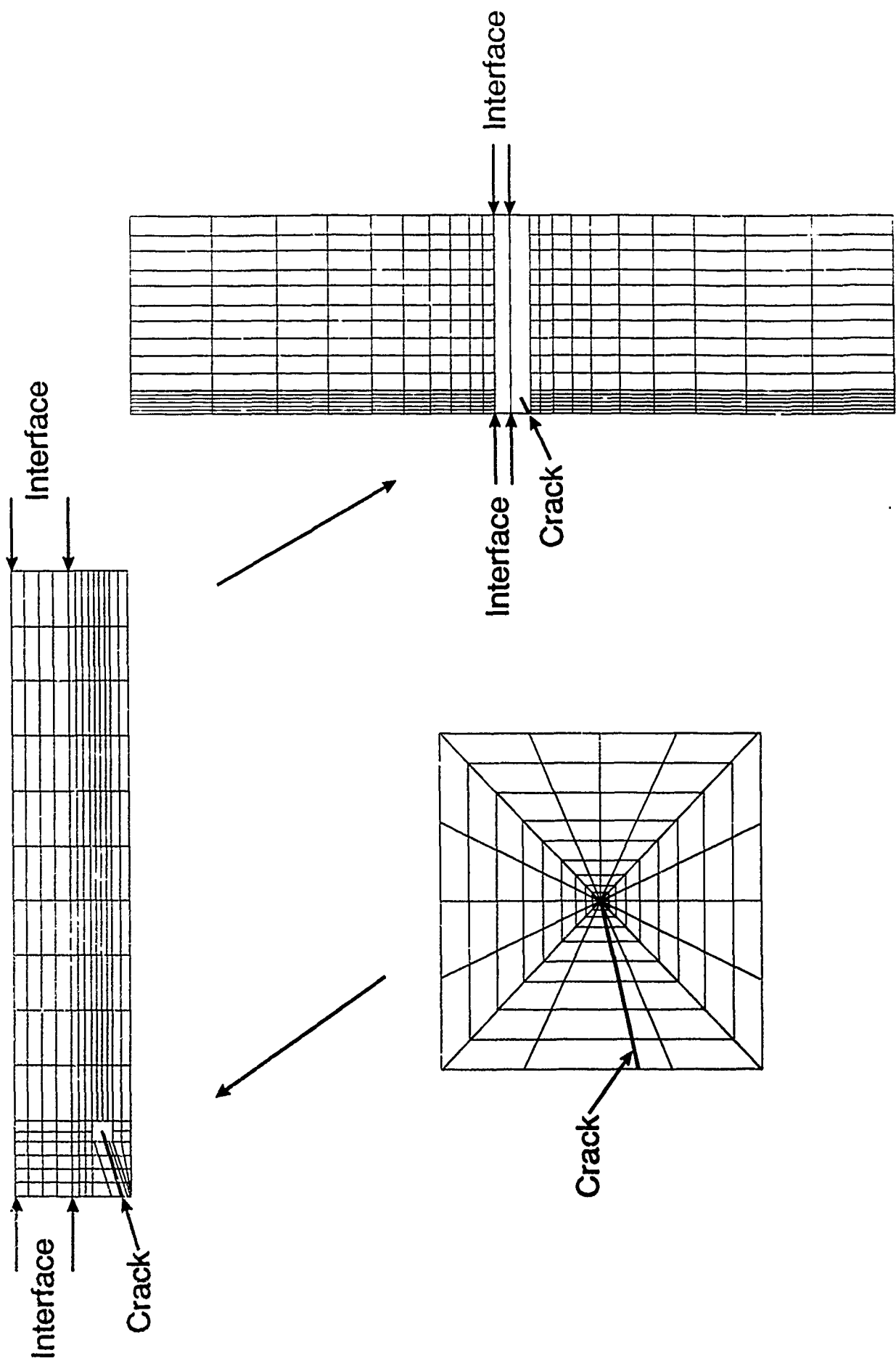
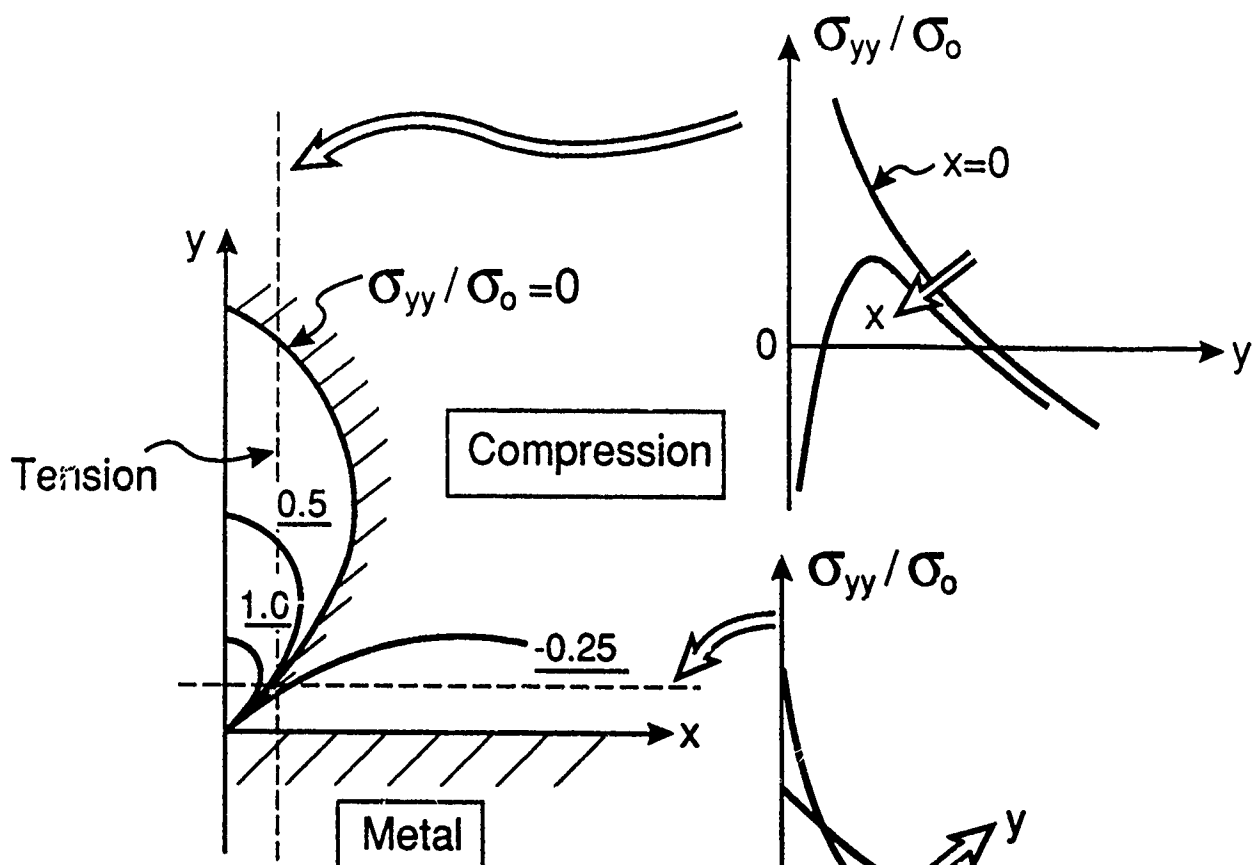


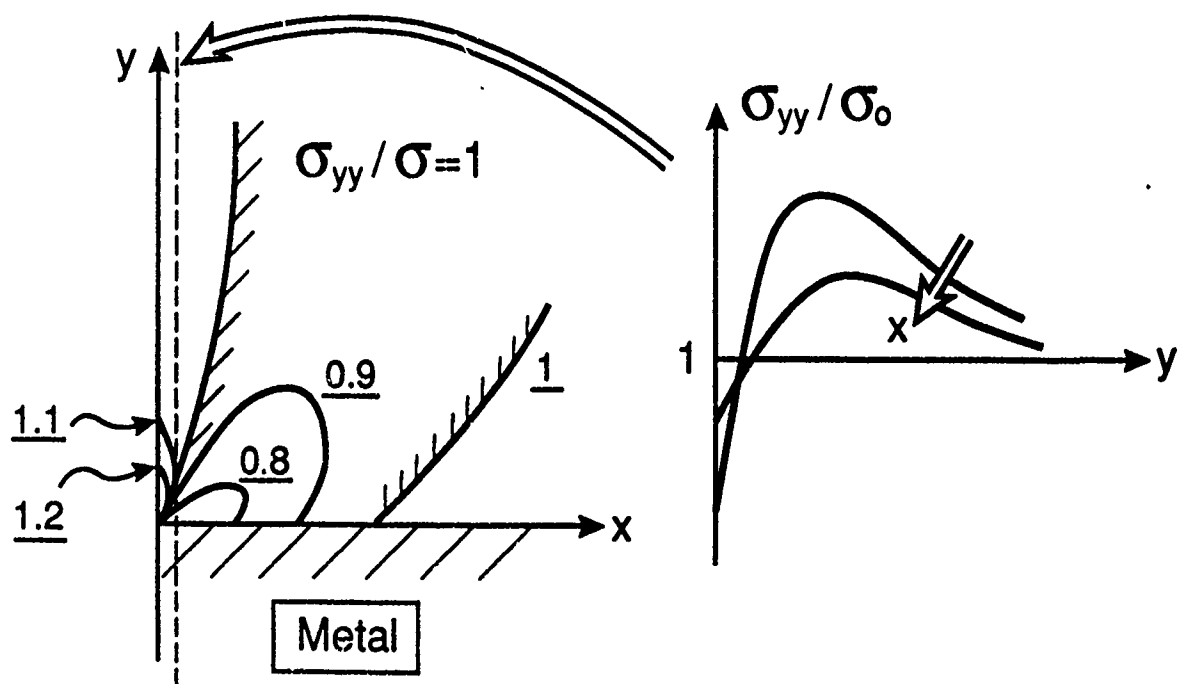
Fig. 2. Typical finite element meshes

c) with a crack inclined to the interface.





a) Residual Field ( $\lambda=3$ )



b) Applied Field ( $\sigma/\sigma_0=2$ )

Fig. 3. A schematic indicating the general characterization of the  $\sigma_{yy}$  stress  
a) residual stress caused by positive misfit b) applied loads.

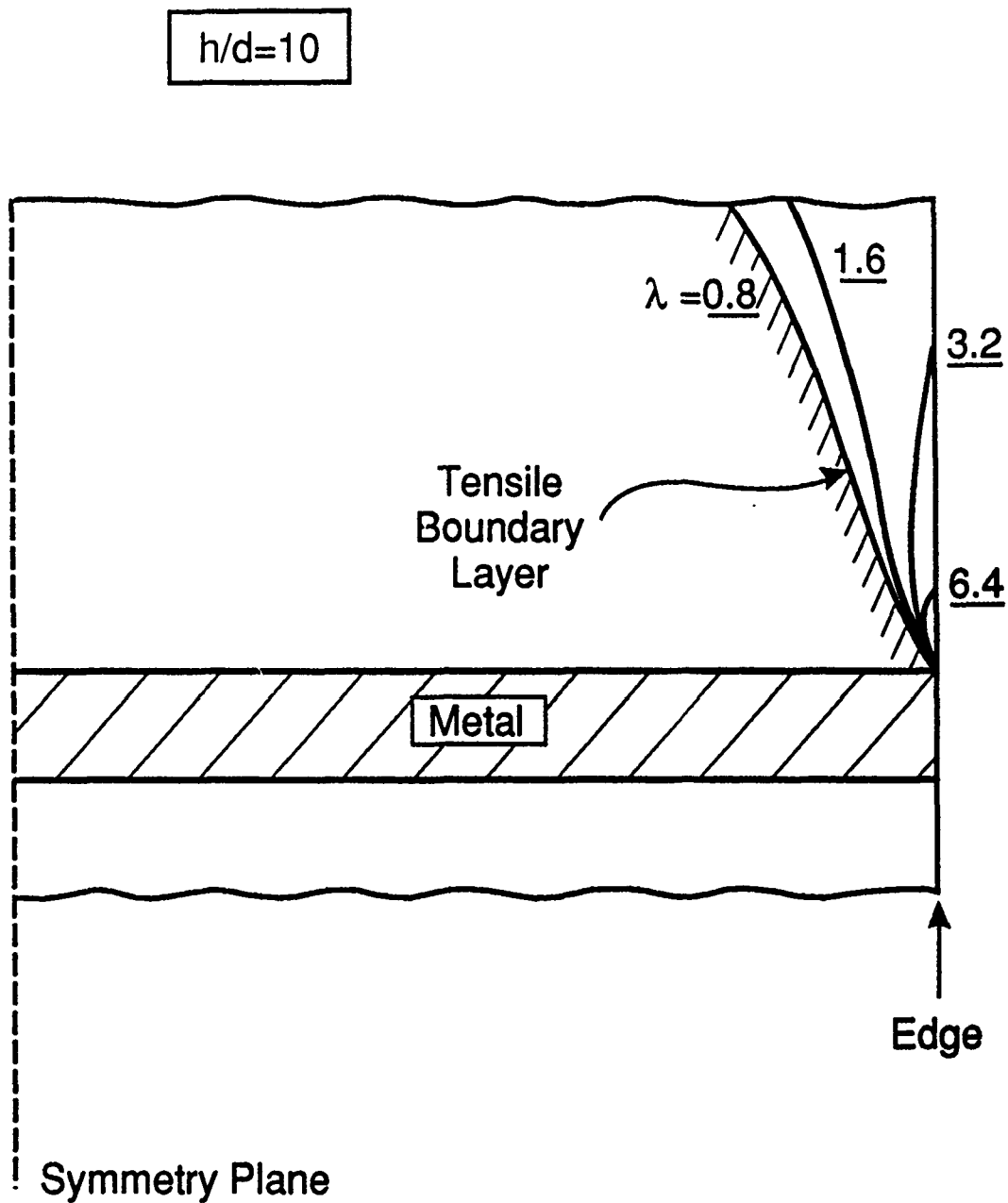


Fig. 4. The  $\sigma_{yy}$  tensile boundary layer caused by the residual field and the effect of the expansion misfit coefficient,  $\lambda = \Delta\alpha\Delta T/\epsilon_0$ .

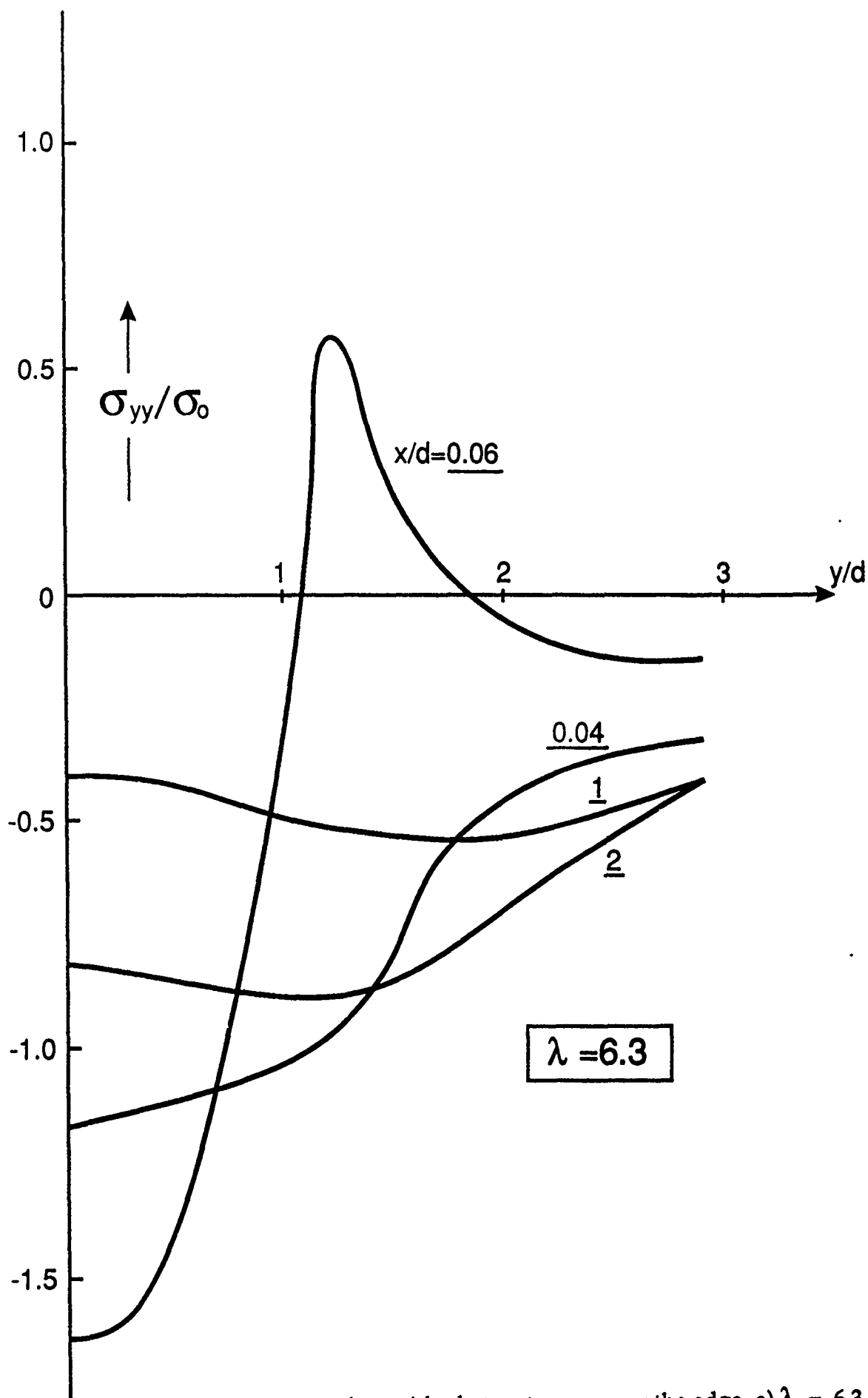


Fig. 5. The residual  $\sigma_{yy}$  stresses near the edge a)  $\lambda = 6.3$

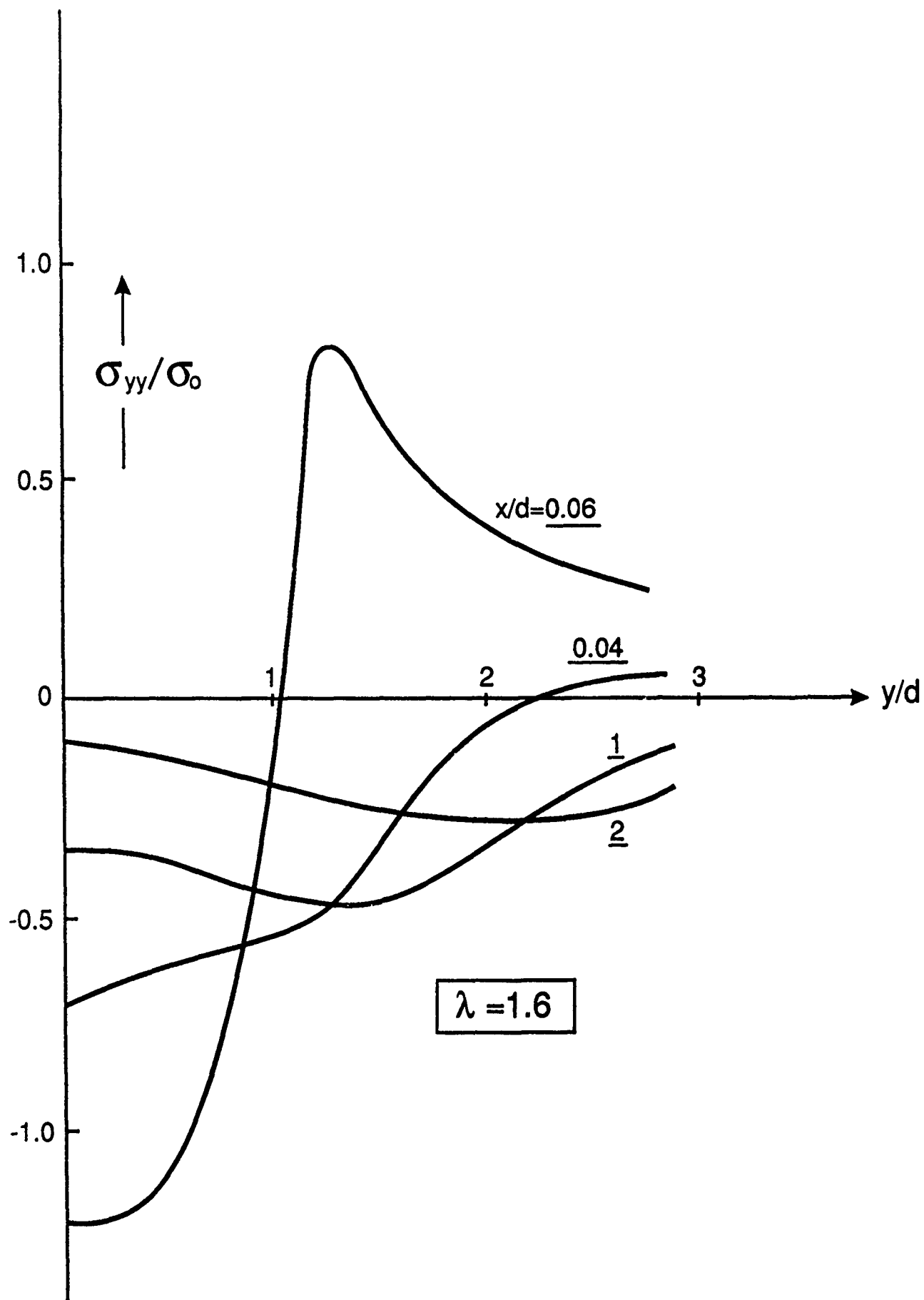


Fig. 5. The residual  $\sigma_{yy}$  stresses near the edge

b)  $\lambda = 1.6$ .

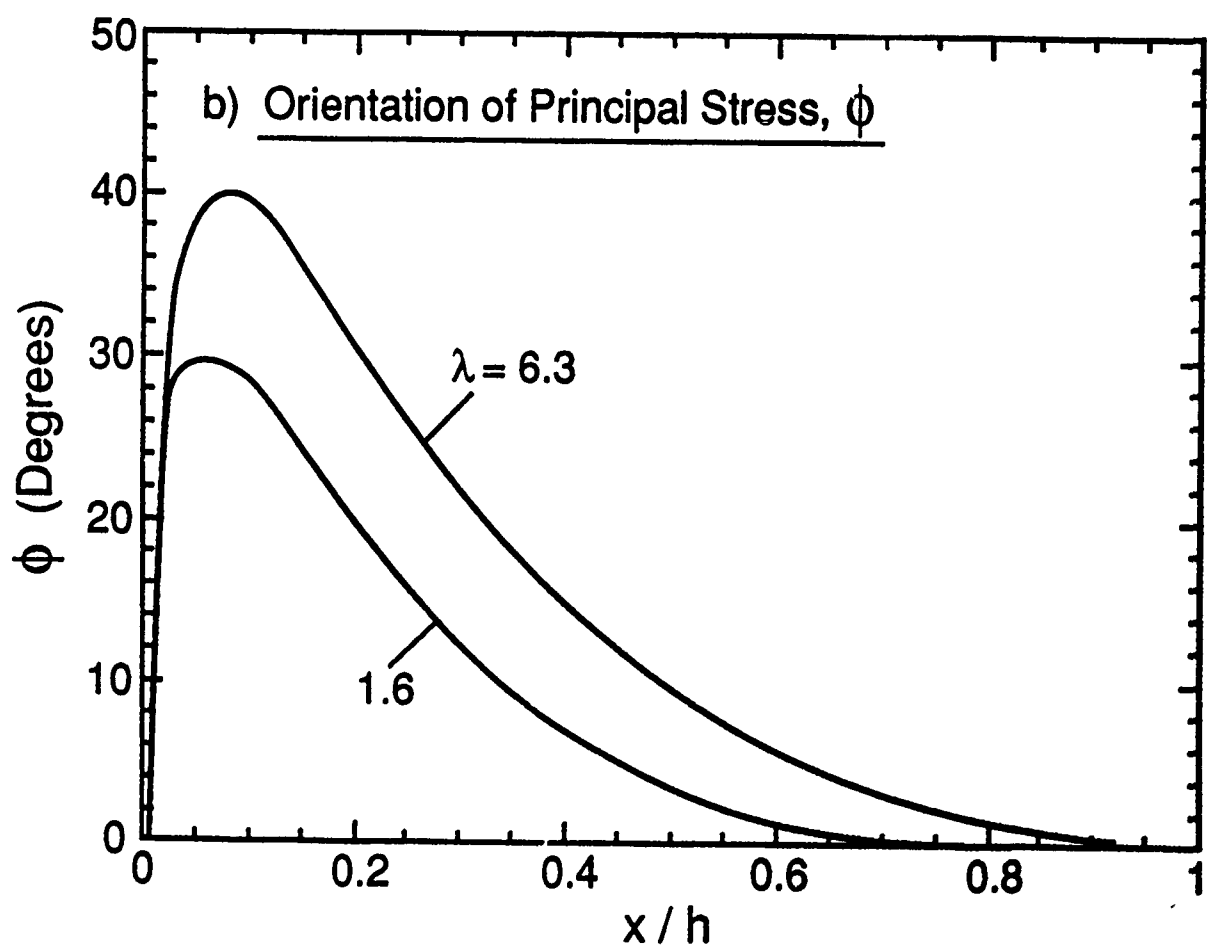
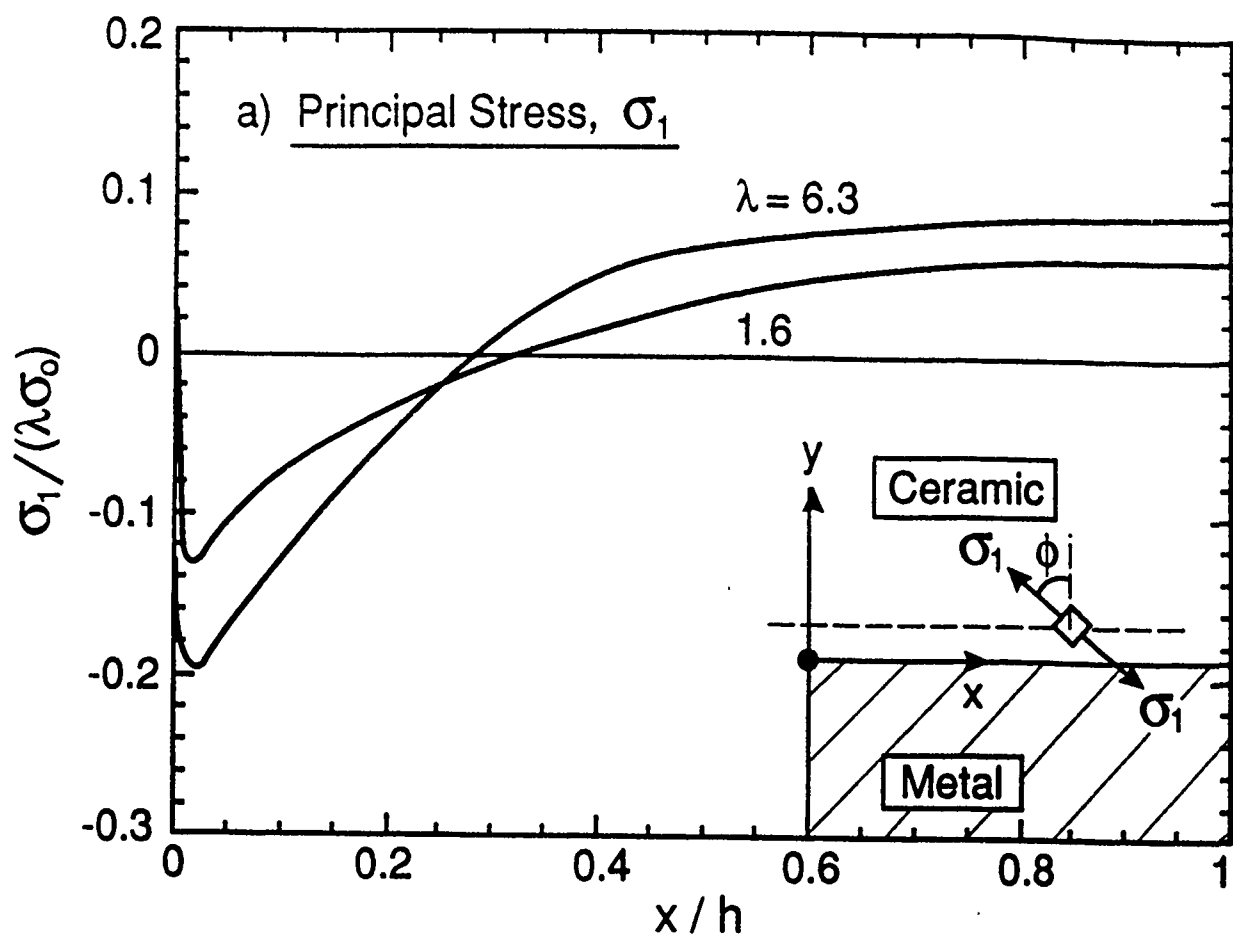


Fig. 6. a) The principal stress,  $\sigma_1$ , in the ceramic near the interface.

b) The orientation of the most positive principal stress,  $\sigma_1$ .

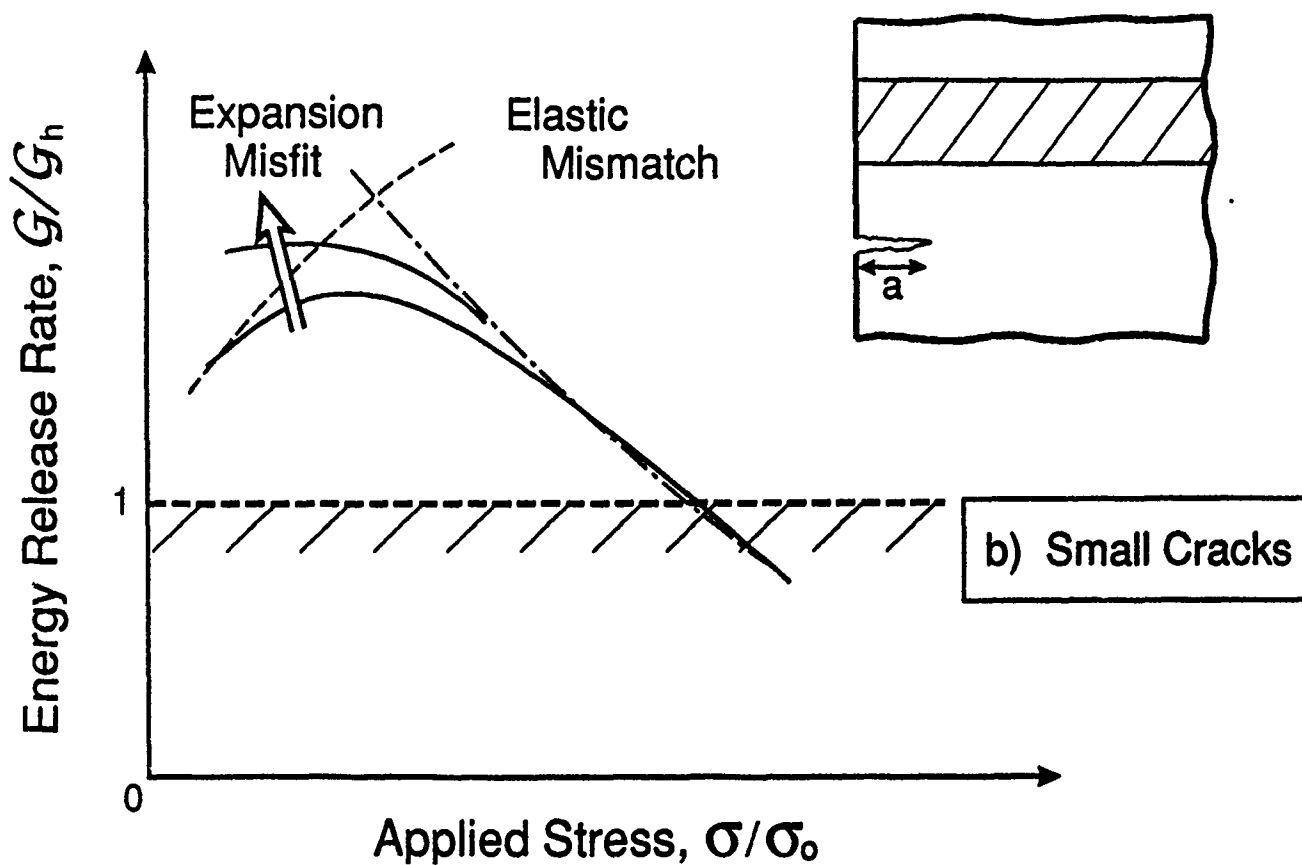
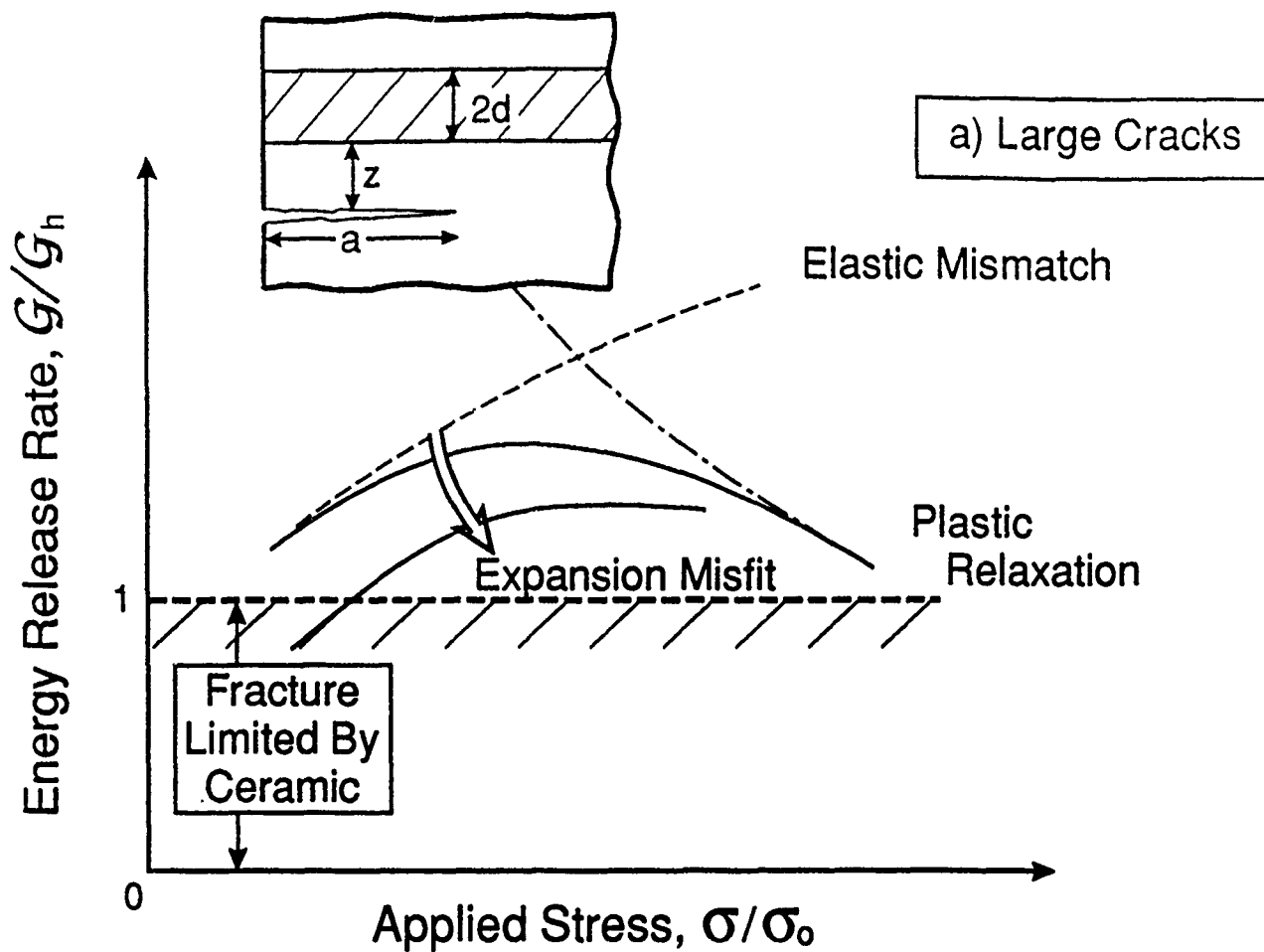


Fig. 7. A schematic indicating trends in the energy release rate with applied stress  
a) large cracks b) small cracks,  $a/h \lesssim 0.1$ .

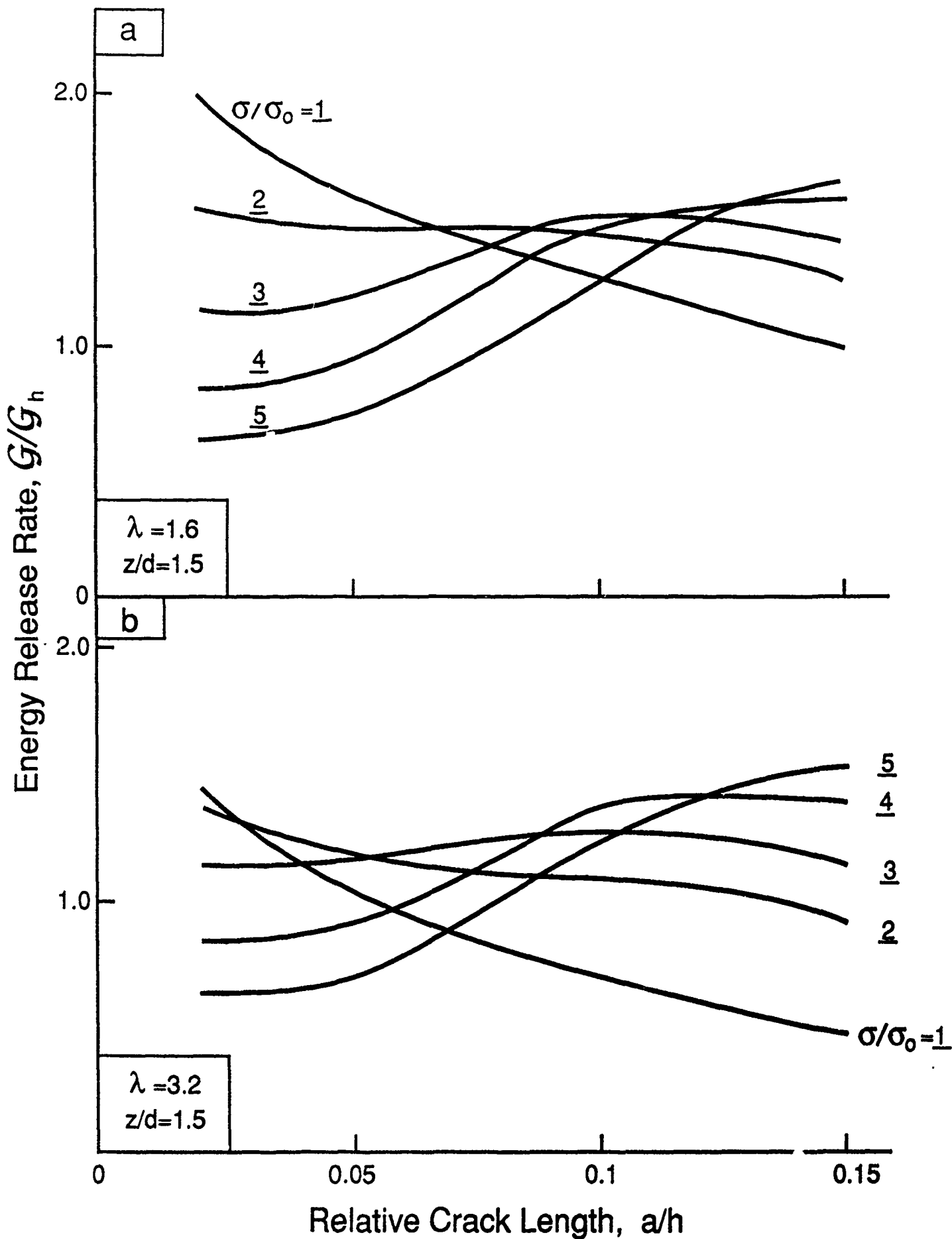


Fig. 8. Variation in the normalized energy release rate with crack length for various stresses a)  $\lambda = 1.6$ ,  $z/d = 1.5$  b)  $\lambda = 3.2$ ,  $z/d = 1.5$ .

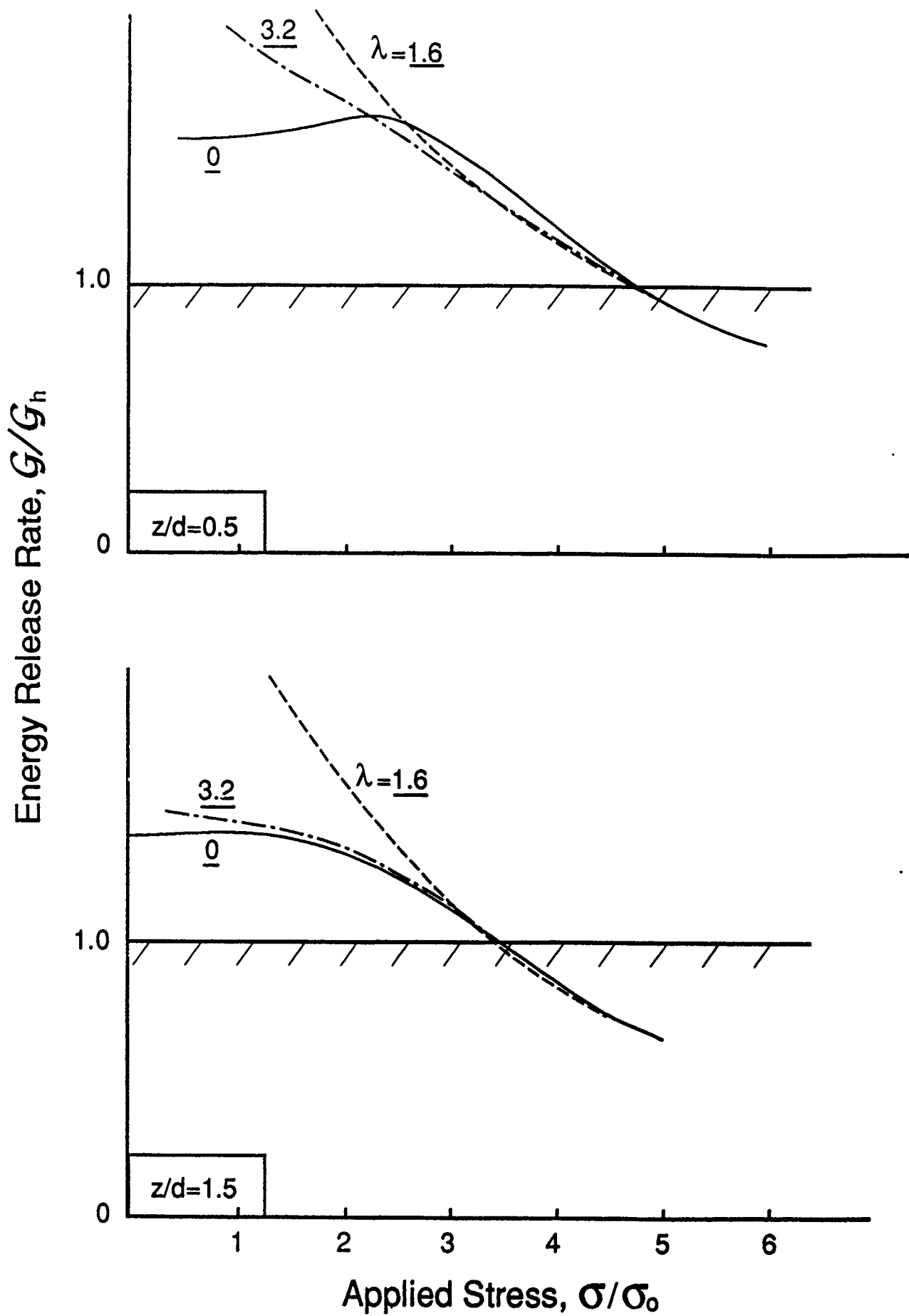


Fig. 9. Effects of stress and expansion misfit on the energy release rate for short cracks, ( $a/h = 0.02$ ) a)  $z/d = 0.5$  b)  $z/d = 1.5$ .



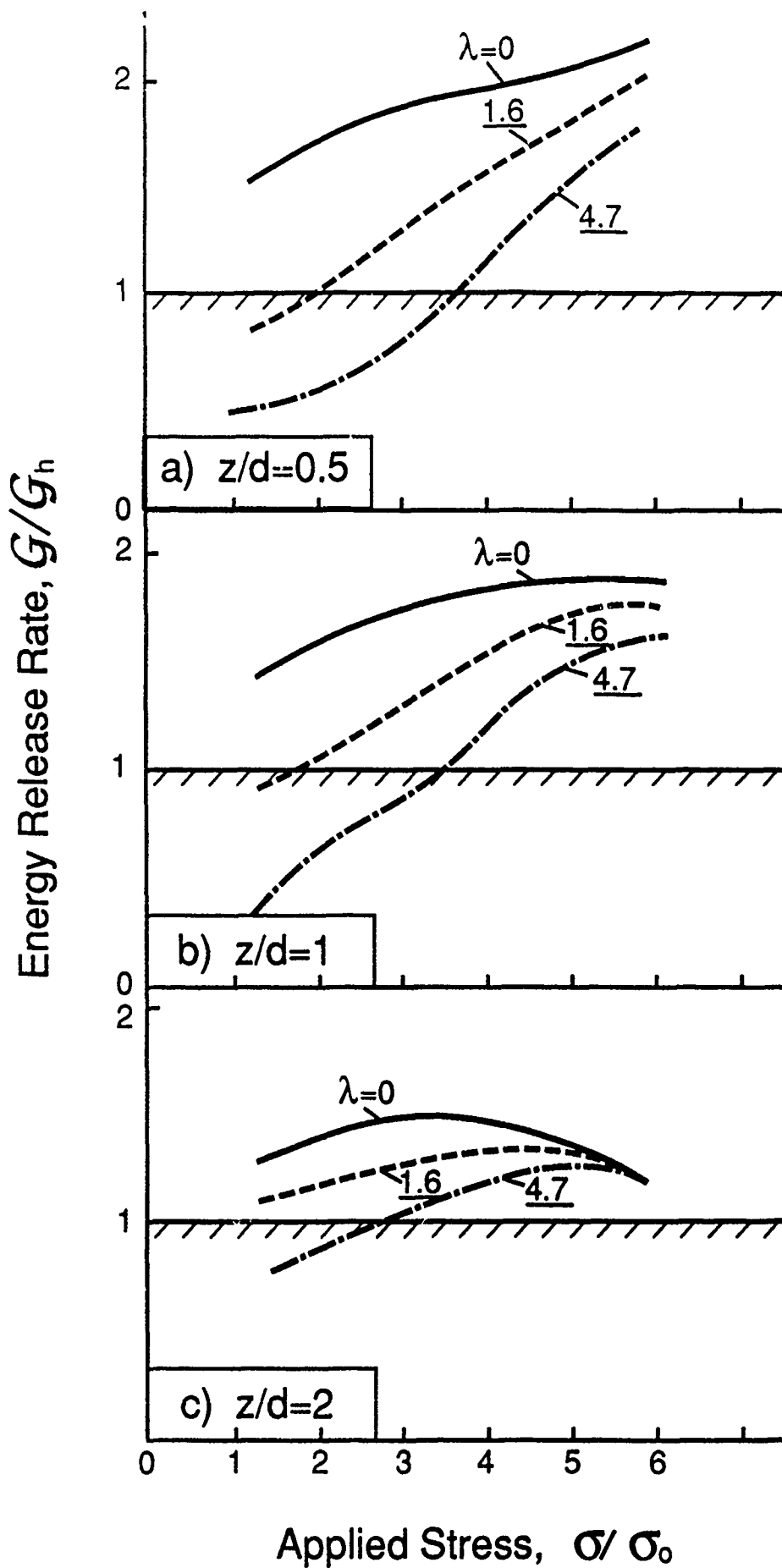


Fig. 10. Effect of stress and expansion misfit on the energy release rate for *long cracks* ( $a/h = 0.2$ ) a)  $z/d = 0.5$  b)  $z/d = 1.0$  c)  $z/d = 2.0$ .

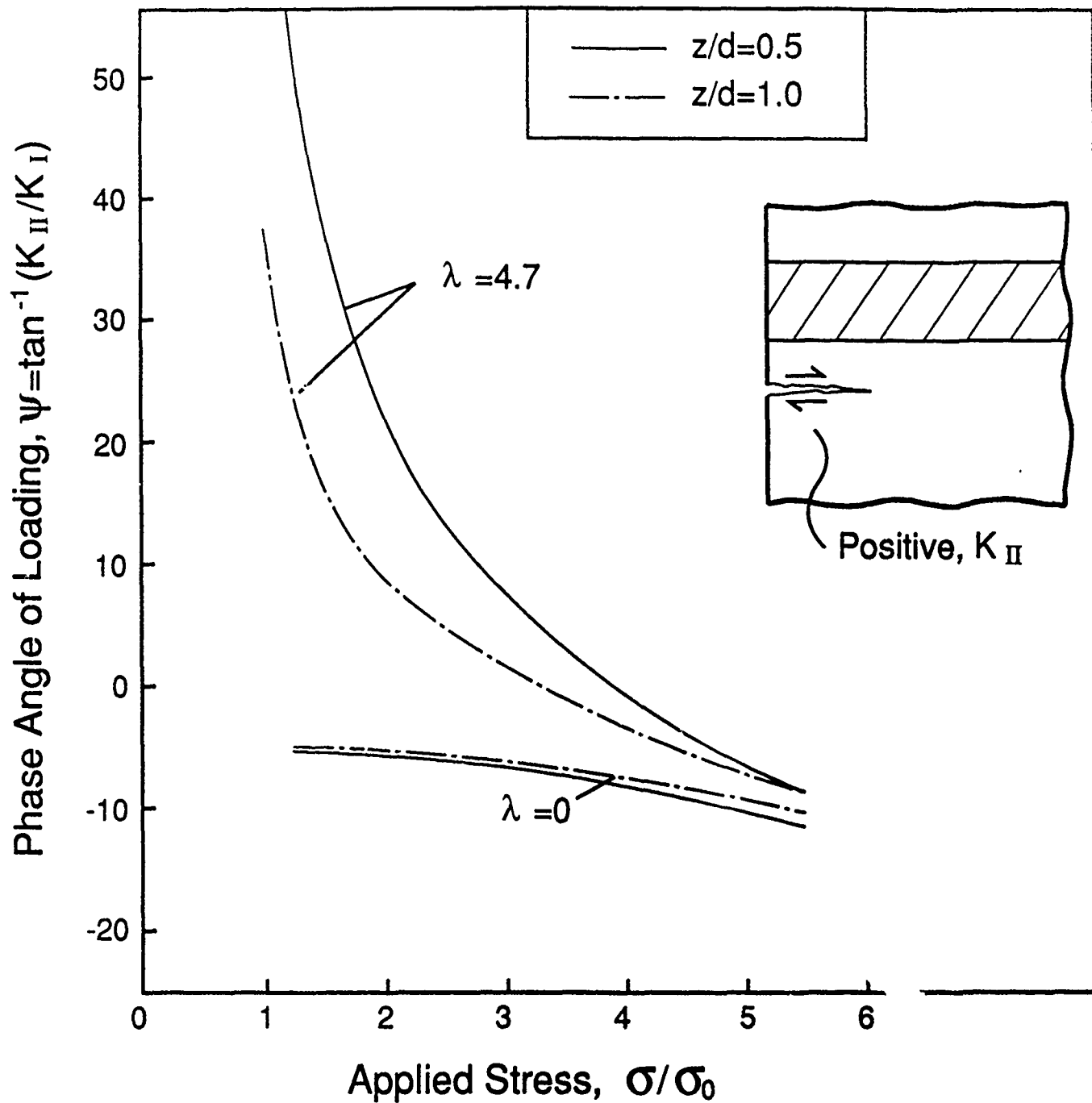


Fig. 11. Effects of stress and expansion misfit on the phase angle of loading for a long crack near the interface ( $a/h = 0.2$ ).

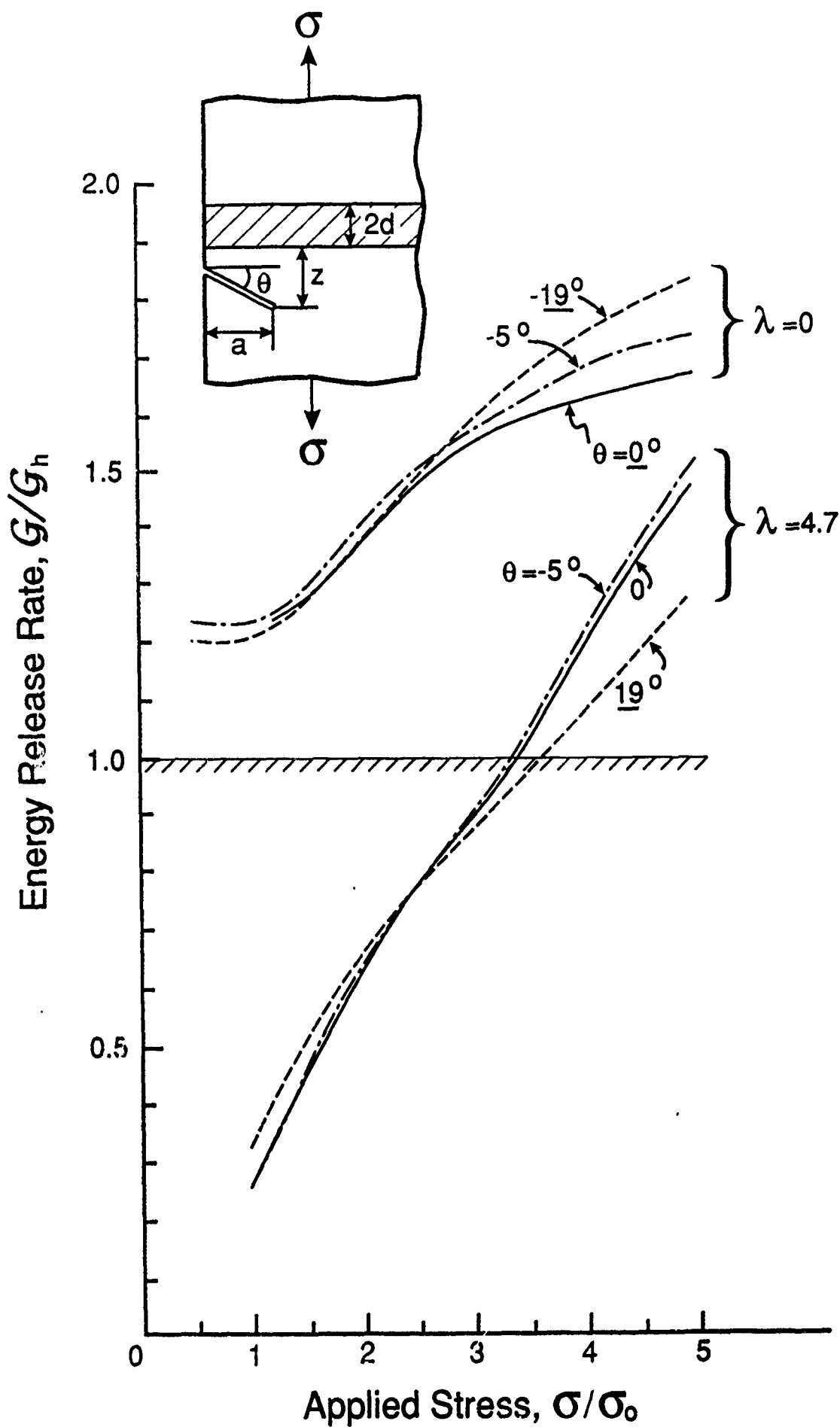
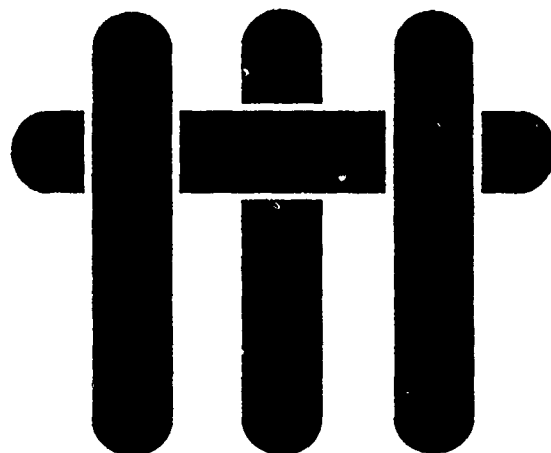


Fig. 12. Effects of crack orientation on the energy release rate.

# M A T E R I A L S



## THE FRACTURE RESISTANCE OF A MODEL METAL/CERAMIC INTERFACE

by

I. E. Reimanis and A. G. Evans

Materials Department  
College of Engineering  
University of California  
Santa Barbara, California 93106

## ABSTRACT

Crack propagation has been measured for the  $\text{Al}_2\text{O}_3/\text{Au}$  interface subject to conditions that exclude stress corrosion. Crack growth has been shown to occur with a rising resistance, governed by intact metal ligaments in the crack wake. The level of resistance also increases as the metal layer thickness increases. Crack extension occurs by a combination of plastic void growth and interface debonding. The fracture energies are much larger than the work of adhesion, but appreciably smaller than those expected for ductile interface fracture. The fracture energy is nevertheless dominated by plastic dissipation, which increases at larger metal layer thicknesses.

## 1. INTRODUCTION

The fracture of metal/ceramic interfaces may involve irreversible processes such as phonon dissipation, plasticity and phase transformations [1, 2, 4-7] and can occur by either brittle or ductile mechanisms [1, 7]. *Brittle mechanisms* involve atomic decohesion at the crack tip [6], whereas *ductile mechanisms* involve void nucleation and growth [7, 8] usually ahead of the tip. Brittle fracture can be environmentally assisted [5, 7], although the associated fracture energy still involves an appreciable contribution from plastic dissipation that occurs in the metal as the brittle crack extends along the interface [5, 7].

The intent of the present study is to investigate explicit effects of plasticity on the fracture of a metal/ceramic interface. A model system of gold bonded to sapphire is used. This system has the attributes that the properties of the constituents have been thoroughly characterized, and that a discrete interface can be produced by diffusion bonding without the formation of interphases and without dissolution of  $\text{Al}_2\text{O}_3$  in the Au [7]. Finally, the transparency of the sapphire allows *in situ* observation of crack propagation along the interface [7].

## 2. EXPERIMENTAL PROCEDURES

### 2.1 Diffusion Bonding

As described previously [7], interfaces between Au and  $\text{Al}_2\text{O}_3$  can be created by the diffusion bonding of high purity polycrystalline Au foil to single crystal  $\text{Al}_2\text{O}_3$  discs having basal plane (0001) orientation. The bonding was done in vacuum ( $\sim 10^{-6}$  torr) at  $1040^\circ\text{C}$  for 48 h and subjected to a normal stress of about 5 MPa. The diffusion bonded discs consisted of thin Au layers of 100, 25 or 10  $\mu\text{m}$  thickness between two thick  $\text{Al}_2\text{O}_3$  layers: one having 1 mm thickness and the other 3.5 mm thickness. The Au foil was polycrystalline after bonding, but highly textured such that the foil plane has a (001)

orientation [7]. Residual porosity remains at the interface<sup>7,9</sup> in the form of isolated, faceted pores in the Au, approximately 3–10  $\mu\text{m}$  wide and about 1  $\mu\text{m}$  deep, with a mean spacing of about 20–50  $\mu\text{m}$ . The thinnest foil exhibited tearing in some locations (Fig. 1).

## 2.2 Mechanical Testing

Most bimaterial interface fracture problems occur under mixed-mode loading conditions [1]. A flexural configuration (Fig. 2) which has a mode mixity angle,  $\psi \approx \pi/4$ , is thus particularly appropriate for the investigation of interface fracture [10]. Furthermore, the relative ease of introducing a stable precrack facilitates use of this specimen. Subsequent to diffusion bonding, beams were diamond machined with overall dimensions, 45  $\times$  3.5  $\times$  4.2 mm. In some cases, side faces were polished to facilitate optical observation during testing. A precrack was established in the following way. Knoop indentations, loaded to  $\sim 50$  N, were placed on the center of the tensile side of the beam. The sample was then loaded in 3-point bending until the crack from the indents grew unstably through the sapphire. Following precracking, three- and four-point bend tests were carried out *in situ* in an inverted optical microscope [7]. The load was measured using a high-resolution, button-type load cell consisting of semiconductor strain gages. Tests were performed in a dry  $\text{N}_2$  environment which was achieved by enclosing the apparatus and maintaining a positive pressure outflow of dry, high purity  $\text{N}_2$ . To fully suppress subcritical crack growth, high purity grade  $\text{N}_2$  (3 ppm  $\text{H}_2\text{O}$ ) was necessary. The chamber was flushed with  $\text{N}_2$  for at least 20 minutes prior to testing.

## 2.3 Characterization

After the crack had been propagated to a length  $\sim 5$  mm, fracture surfaces were prepared for microscopic investigation using the following procedure. Water was introduced into the crack front and the specimens loaded in 3-point bending, whereupon the  $H_2O$  debonded intact regions by stress corrosion. This process occurred at sufficiently low load levels that the fracture surface remained essentially undamaged. Thereafter, the specimens were embedded in epoxy to ensure that the mating fracture surfaces were not damaged during subsequent cutting. Following diamond sawing into the desired shape, the specimens were removed from the epoxy by soaking in acetone, and the top sapphire layer separated from the Au foil to allow characterization of the fracture surfaces. These surfaces were investigated in the SEM in conjunction with X-ray spectroscopy (EDS) to determine possible chemical differences

## 3. RESULTS

### 3.1 Measurements and Observations

Four-point flexure tests conducted in a dry  $N_2$  atmosphere revealed resistance behavior, manifest in loads that increased as the interface cracks extended. The resistance  $\Gamma_R$  determined from the loads has the characteristics indicated in Fig. 3. Both the initiation resistance  $\Gamma_0$  and the subsequent growth resistance appear to increase as the metal layer thickness increases. Explicit trends in  $\Gamma_0$  with metal layer thickness are presented in Fig. 4.

The crack growth mechanisms, which were ascertained from *in situ* observations, revealed some dependence on the metal layer thickness, although generic characteristics exist. In particular, alternate debonding usually occurred on *both interfaces*, as illustrated schematically in Fig. 5a. This behavior was elucidated by matching top and bottom



interfaces, wherein the region which remained intact on the top interface (Fig. 5b) debonded on the bottom interface (Fig. 5c). Consequently, ductile ligaments bridge the crack, even after crack extensions of 5 mm. Slip lines visible on the perimeter of the intact area (Fig. 6a), which delineate the plastically deformed ligaments, are continuous through the metal (Fig. 6a, b). The intact areas begin to debond  $\sim 3$  n.m behind the crack tip and continue to debond as the crack extends (Fig. 7). The debonding behind the crack tip occurred by continuous decohesion with no obvious interaction with interface porosity. For Au layers having intermediate and larger thickness, the crack front extended primarily on the upper interface, but for the thinnest layers the crack preferentially selected the lower interface.

Subsequent to crack extension of several millimeters in dry  $N_2$ , some samples were unloaded and reloaded in 3-point bending in air, thereby causing the intact ligaments between crack faces to debond by stress corrosion. When all of the intact ligaments had been debonded, the sample was again unloaded and reloaded in 4-point bending in dry  $N_2$ . The crack was found to resume growth at an energy release rate comparable to the initiation resistance  $\Gamma_0$ , and to further extend subject to a resistance curve having the same characteristics as the original curve (Fig. 8). *These experiments explicitly relate the rising fracture resistance to the presence of metal ligaments across the interface crack faces*, consistent with previous studies on the Cu/glass system [5].

The *initial growth* mechanisms were most readily *visualized* from experiments wherein the crack had been previously extended by stress corrosion, resulting in a ligament-free crack. The crack in the thicker Au layers was observed to extend by abrupt increments of order 200  $\mu\text{m}$  in width, occurring at distinct sites along the crack front (Fig. 9), with no evident interaction with the interface porosity. The contrast which developed along the fracture surface delineates the grain boundaries in the Au and indicates that the increments of crack growth typically encompass several grains. For Au layers of intermediate thickness, voids nucleated *ahead* of the crack front (Fig. 10).

The nucleation sites are pre-existing pores on the interface within  $\sim 30 \mu\text{m}$  of the crack front. Voids within about  $10 \mu\text{m}$  of the crack extend back and coalesce with the crack, whereas voids greater than about  $10 \mu\text{m}$  from the crack grow, but do not necessarily interact with the crack. The associated plastic deformation, which extends approximately 1 pore diameter, was  $\sim 0.1 \mu\text{m}$  deep, as measured using an electron damage technique [7]. Finally, in the thinnest Au layer, the crack extends continuously on the lower interface by direct growth from the crack front, with some isolated debonding in the form of void growth, on the upper interface, reminiscent of the crack growth process subject to stress corrosion [7].

*Subsequent to initial growth*, continued crack extension was accompanied by *periodic debonding* at the second interface. Interfacial pores were located at the centers of each debond, suggesting that pores are the preferred nucleation sites. The nature of void growth ahead of the crack and thus, the size of the intact ligaments, was noted to depend on the metal layer thickness: the intact ligaments being smallest for the thinnest layers. A characterization of the size and distribution of intact areas is summarized in Table I.

The annulus of plastic distortion at the perimeter of intact ligaments also depended on the metal layer thickness. Typically, the annuli had widths of  $\sim 50 \mu\text{m}$  and  $\sim 150 \mu\text{m}$  for the  $25 \mu\text{m}$  and  $100 \mu\text{m}$  Au layer thicknesses, respectively. Intact regions smaller than about  $20 \mu\text{m}$  in diameter exhibited no detectable deformation. An estimate of the plastic strain in the ligaments was obtained from measurements of the difference in height between the intact and the debonded regions, using the electron beam damage technique. This height difference was observed to depend on the metal layer thickness, but typically had maximum values in the range of  $1\text{--}2 \mu\text{m}$ , which corresponds with a plastic shear strain of  $\sim 5 \times 10^{-3}$ .

Finally, the uniaxial flow stress of the Au was estimated *in situ* by emplacing Vicker's indentations into the Au side of the fracture surfaces, using loads of  $0.01\text{N}$ . The

indent size was less than about one-third the Au layer thickness to ensure that the  $\text{Al}_2\text{O}_3$  substrate did not have an effect. By regarding that the hardness,  $H \approx 3 \sigma_0$  [11], the flow stress was estimated as  $\sigma_0 \approx 130 \text{ MPa}$  for all three layer thicknesses. This strength is larger than that for bulk annealed Au.

### 3.2 Interface Characterization

Following crack growth in dry  $\text{N}_2$ , surfaces separated by stress corrosion in water were observed in the SEM. X-ray analysis in the SEM revealed no evidence of Au on the sapphire and no evidence of Al on the Au, even in the regions where crack propagation occurred in dry  $\text{N}_2$  by a void growth mechanism. It is thus concluded that fracture proceeded along the interface plane.

An estimate of the work of adhesion,  $W_{\text{ad}}$ , was obtained from measurements of angle  $\theta$  between the pore wall and the Au fracture surface (Appendix), as measured on Au fracture surfaces created by subcritically growing the crack in the presence of water. About 30 such angles were measured giving  $\theta = 135^\circ \pm 8^\circ$ . The work of adhesion was calculated from  $\theta$  [12] by using a surface energy for Au, given by  $\gamma_m = 1.3 \text{ Jm}^{-2}$  [13, 14]. This gave,  $W_{\text{ad}} \approx 0.38 \pm 0.12 \text{ Jm}^{-2}$ .

## 4. MICROMECHANICS OF METAL/CERAMIC INTERFACES

### 4.1 Initial Crack Extension

Analysis of ductile fracture mechanisms associated with stationary cracks in a thin metal foil between two elastic plates [15] recognizes that the plastic constraint in a thin metal layer causes the stress to attain values substantially larger than that possible in a homogeneous elastic/plastic solid (Fig. 11). Furthermore, a stress maximum occurs at a distance ahead of the crack governed by the metal layer thickness. One *ductile*

*fracture* mechanism involves the unstable plastic *cavitation* which occurs when the mean stress at the interface,  $\sigma_m$ , reaches a critical value. This instability has been shown to occur when the ratio of the mean stress to the uniaxial yield stress,  $\sigma_0$ , is given by

$$\sigma_m/\sigma_0 \approx 5.5 \quad (1)$$

In mode I loading, the preceding analysis predicts a distance between the location of this maximum stress and the crack tip given by [15]

$$d \approx 2.2h \quad (2)$$

where  $h$  is the metal layer thickness. The corresponding critical energy release rate for initial mode I crack growth is [15]

$$\Gamma_0 = 0.2\sigma_0 h \quad (3)$$

A *second ductile mechanism* obtains when the pore spacing is sufficiently small that the pores near the crack tip nucleate voids which grow plastically and coalesce with the crack tip. The mode I fracture energy for this process is given by [16]

$$\Gamma_0 = 2.0\sigma_0\delta_t \quad (4)$$

where  $\delta_t$  is the critical crack tip opening displacement. Initial crack growth is presumed to occur when  $\delta_t$  is on the order of the pore spacing,  $\chi_0$  [17], such that

$$\Gamma_0 \approx 2.0\sigma_0\chi_0 \quad (5)$$

Consequently, the ratio of the flaw spacing  $\chi_0$  to the metal layer thickness  $h$  is an important quantity in controlling the *ductile fracture* mechanism that dominates initial crack growth. Specifically, for  $\chi_0/h < 0.1$  the energy for ductile fracture by void coalescence is below that for cavitation, and vice versa, as indicated on Fig. 12.

When interface fracture involves *debonding*, as well as plastic void growth, Eqns. (3) and (5) represent *upper bounds for the fracture energy*. Explicit relations between  $\Gamma_0$  and either the plastic flow strength or the work of adhesion when debonding occurs are unknown. Some possibilities suggested by the experiments, with the insight given by Eqns. (3) and (5), are discussed in Section 5.

## 4.2 The Fracture Resistance

The rising resistance behavior can be rationalized by examining the effect of crack surface tractions caused by the intact metal ligaments on the energy release rate. Analysis of this phenomenon for mixed-mode cracks indicates that such tractions reduce the mode I crack tip stress intensity but *increase* the mode II stress intensity [18]. Consequently, the fracture energy  $\Gamma_R$  varies sensitively with the mode mixity dependence of the underlying interface crack extension mechanism. Expressions for this mixity effect are needed before resistance curves can be calculated [18]. An expression for the mixity effect that appears to conform with typical experimental data is given by [19]

$$\Gamma_R/\Gamma_0 = [1 - (1 - \lambda)\sin^2\psi]^{-1} \quad (6)$$

where  $\psi$  is the mixity angle (zero for mode I and  $\pi/2$  for mode II) and  $\lambda$  is a parameter between 0 and 1. Specifically, the fracture energy of a material with  $\lambda \rightarrow 1$  has little

sensitivity to mixity angle, whereas  $\lambda \rightarrow 0$  refers to strong effects of mixity. Experimental results are mostly in the range  $\lambda \approx 0.1-0.3$  [19]. With this background, the calculations [18] reveal that the resistance  $\Gamma_R$  can be characterized by the non-dimensional parameter

$$\Sigma = ph / E_c \Gamma_o \quad (7)$$

where  $E_c$  is the Young's modulus for the ceramic and  $p$  is the traction exerted by the ligaments on the crack surfaces. For metal ligaments

$$p = \sigma_o f_p \quad (8)$$

where  $f_p$  is the area fraction of Au which contributes to the bridging given in Table I. Resistance curves predicted for a range of  $\Sigma$  and  $\lambda$  are plotted on Fig. 13.

## 5. THE CRACK GROWTH RESISTANCE

In the presence of  $H_2O$ , stress corrosion occurs at the interface with a low fracture energy [7], suggestive of *brittle bond rupture* at the interface. Such a brittle mechanism occurs despite the incidence of plastic flow and some crack blunting. In dry  $N_2$ , interface fracture by plastic void growth is the prevalent mechanism, but this is accompanied by interface debonding. In an attempt to correlate the fracture energy trends, it is first recalled that the initiation fracture resistance,  $\Gamma_o$ , is smaller than the level expected for ductile interface fracture (Fig. 12). Another notable feature is that the non-dimensional fracture energy,  $\Gamma_o / \sigma_o h$ , increases as the metal layer thickness decreases, indicative of a corresponding increase in the *relative* contribution of plasticity to the fracture energy. This effect is the origin of the non-linearity apparent in Fig. 4.

However, the *absolute* contribution of plasticity to  $\Gamma_o$  must decrease as the metal layer thickness decreases and approach zero as  $h \rightarrow 0$ . Furthermore, since fracture involves interface decohesion, it is reasonable to suppose that  $\Gamma_o \rightarrow W_{ad}$  as  $h \rightarrow 0$ . With this background, plus the insights provided by Section 4.1, it has been possible to identify a simple non-dimensional expression for  $\Gamma_o$ , which includes the role of  $W_{ad}$ , given by (Fig. 4),

$$\Gamma_o \approx W_{ad} [1 + \sigma_o h / W_{ad}]^{1/2} \quad (9)$$

While this expression has no fundamental basis, it appears to be useful for correlating experimental information and should provide guidance for the development of crack growth models.

The subsequent resistance,  $\Gamma_R$ , above  $\Gamma_o$ , may be rationalized using the ligament model presented in Section 4.2 in conjunction with the information in Table I, plus the uniaxial yield strength obtained from hardness measurements. Then, with  $\Gamma_o$  from Fig. 3, the experimental data can be transposed onto Fig. 13. It is apparent from this construct that the normalization suggested by the models brings the data onto a single curve, consistent with the curve calculated for a mixity parameter,  $\lambda \approx 0.2$ . Values of  $\lambda$  in this range are typical for interfaces [19]. It is thus concluded that the resistance behavior ( $\Gamma_R > \Gamma_o$ ) is explicable in terms of the bridging associated with intact metal ligaments. It is recalled that such bridging effects are specimen geometry dependent [18] and consequently,  $\Gamma_R$  should not be construed as an unique resistance characteristic of the interface.

## 6. CONCLUDING REMARKS

This study has demonstrated several characteristics of crack propagation along a metal/ceramic interface. The fracture resistance is sensitive to moisture through a stress corrosion mechanism. In the absence of stress corrosion, the interface cracks extend subject to a rising resistance curve, governed by intact metal ligaments in the crack wake. Additionally, the resistance increases as the metal layer thickness increases. These changes in resistance with crack extension are fully explicable in terms of crack shielding caused by the bridging ligaments.

Crack extension occurs by a combination of plastic void growth (that typically initiates at interface pores) accompanied by brittle interface debonding. The measured fracture energies are substantially greater than the work-of-adhesion, but less than the values expected for ductile interface fracture. It has not been possible to use existing models of the plastic dissipation to correlate the experimental fracture energy data. Instead, a semi-empirical function has been identified that seemingly correlates the present data. The development of the associated understanding is an important topic for further research.



## APPENDIX

The equilibrium angle  $\theta$  between the Au and  $\text{Al}_2\text{O}_3$  at an interface and the pore depth can be measured in the following way. First, an electron beam damage line is induced in the SEM across the void with the surface normal to the beam. Tilting by  $\Psi$  about an axis parallel to the deposition line, the depth of the void  $d$  is reflected in the displacement  $\Delta a$ , (Fig. A1):  $d = \Delta a / \sin \Psi$  [20]. The angle  $\theta$  is obtained by geometry in terms of the rotation angles  $\theta_R$  and  $\Omega$  (Fig. A1), such that

$$\tan \vartheta = \frac{d \cos \beta \tan \vartheta_r}{d \sin \Psi - \Delta h \tan \vartheta_r} \quad (\text{A1})$$

where

$$\Delta h = d \cos \Psi \sin \beta \quad (\text{A2})$$

For the ellipse in Fig. A1

$$y = d \sin \Psi \sin \beta, \quad (\text{A3})$$

$$\equiv \frac{d \cos \Psi}{\tan \Omega} \quad (\text{A4})$$

Consequently, equating (A3) and (A4),

$$\beta = \sin^{-1} \left[ \frac{1}{\tan \Psi \tan \Omega} \right] \quad (\text{A5})$$

Placing (A5) and (A2) into (A1) gives

$$\tan \vartheta = \frac{\cos \left\{ \sin^{-1} \left[ \frac{1}{\tan \Psi \tan \Omega} \right] \right\} \tan \vartheta_r}{\sin \Psi \tan \Omega - \frac{\cos^2 \Psi \tan \vartheta_r}{\sin \Psi \tan \Omega}} \quad (\text{A6})$$

Thus,  $\vartheta$  is obtained from knowledge of the SEM tilting angle,  $\Psi$ , and from measurements of  $\Omega$ , and  $\vartheta_r$  in Fig. A2.

TABLE I

Au Layer Thickness $h$ ( $\mu\text{m}$ )	Area Fraction of Debond on Lower Interface $f_p$	Width of Intact area ( $\mu\text{m}$ )
10	0.8–0.9	< 50
25	0.4–0.6	50–100
100	0.2–0.4	100–200

## 7. REFERENCES

- [1] A. G. Evans, M. Rühle, B. J. Dalgleish and P. G. Charalambides, *Mtls. Sci. and Engr.*, **A126**, 53–64 (1990).
- [2] R. M. Cannon, R. M. Fisher and A. G. Evans, *Materials Research Society Proceedings*, **54**, 799 (1986).
- [3] B. J. Dalgleish, M. C. Lu and A. G. Evans, *Acta Metall.*, **36**, 2029 (1988).
- [4] R. M. Cannon, V. Jayaram, B. J. Dalgleish and R. M. Fisher, "Ceramic Microstructures," *Mat. Sci. Res.*, Vol. **21**, Eds. Pask and A. G. Evans, p. 959 (1986).
- [5] T. S. Oh, J. Rodel, R. M. Cannon and R. O. Ritchie, *Acta Metall.*, **36**, 2083 (1988).
- [6] P. M. Anderson, J. S. Wang and J. R. Rice, "Thermodynamic and Mechanical Models of Interfacial Embrittlement," *34th Sagamore Army Materials Research Conference*, Lake George, NY, (August 1987).
- [7] I. E. Reimanis, B. J. Dalgleish, M. Brahy, M. Rühle and A. G. Evans, "The Effects of Plasticity in the Fracture Resistance of Metal Ceramic Interfaces," *Acta Metall. Mater.*, in press.
- [8] B. J. Dalgleish, K. P. Trumble and A. G. Evans, *Acta Metall.*, **37**, 1923 (1989).
- [9] B. Derby, E. R. Wallach, "Diffusion Bonding: development of theoretical models," *Metall Science*, **18**, p. 427, (Sept. 1984).
- [10] P. G. Charalambides, J. Lund, A. G. Evans and R. M. McMeeking, "A test specimen for determining fracture resistance of bimaterial interfaces," *Jnl. Appl. Mech.*, **56**, 77 (1989).
- [11] D. Tabor, *Hardness of Metals*, Clarendon Press, Oxford (1951).
- [12] E. D. Hondros, "Bonding of Metal/Ceramic Interfaces," *Inst. Phys. Conf., Ser.* No. 75: Conf. Science of Hard Materials, Chapter II (1986).
- [13] A. R. Miedema, "Surface Energies of Solid Metals," *Zeitschrift für Metallkund* (Stuttgart [etc.]), Vol. **69**, 287, (1978).
- [14] R. M. Pilliar and J. Nutting, "Solid-Solid Interfacial Energy Determinations in Metal-Ceramic Systems," *Phil. Mag.*, **16**, 181 (1967).
- [15] A. G. Varias, Z. Suo and C. F. Shih, to be published.
- [16] R. M. McMeeking, "Finite Deformation Analysis of Crack-Tip Opening in Elastic-Plastic Materials and Implications for Fracture," *J. Mech. Phys. Solids*, **25**, 357 (1977).

- [17] J. R. Rice and M. A. Johnson, *Inelastic Behavior of Solids* (Ed. M. F. Kenninen *et al.*) McGraw-Hill (1970) p. 641.
- [18] G. Bao, B. Fan and A. G. Evans, *Mech. Mtls.*, in press.
- [19] H. Jensen, J. W. Hutchinson and K. S. Kim, *Intl. Jnl. Solids Structures*, **26** (1990) 1099.
- [20] R. A. Hoover, *J. Phys. E. Scientific Instruments* **4**, 747 (1971).

## FIGURE CAPTIONS

- Fig. 1. Optical micrograph of 10  $\mu\text{m}$  thick Au foil diffusion bonded between plates of sapphire, showing tears in the Au (arrowed).
- Fig. 2. Flexure specimen geometry used for interface fracture energy measurements.
- Fig. 3. Interface fracture energy  $\Gamma_R$  as a function of crack length  $a$ , for 10, 25 and 100  $\mu\text{m}$  thick Au layers.
- Fig. 4. Initiation fracture energy as a function of actual and relative metal layer thickness.
- Fig. 5. Debonding along alternate interfaces. (a) Schematic illustration (b) the intact depression along the crack front on the top interface corresponds to debonded area on the bottom interface (c).
- Fig. 6. a) Intact ligament on top interface with slip lines visible at the perimeter b) Debonded area on bottom interface corresponding to (a), also showing slip lines.
- Fig. 7. a) Intact ligament region behind crack tip. b) The same region as in (a) for a larger crack length: Intact area is commencing to debond in (b).
- Fig. 8. Interface fracture energy as a function of crack length before and after removing intact ligaments by stress corrosion.
- Fig. 9. Crack initiation and growth for 100  $\mu\text{m}$  thickness at three different levels of energy release rate a) 63  $\text{Jm}^{-2}$ , b) 96  $\text{Jm}^{-2}$  and c) 131  $\text{Jm}^{-2}$ .
- Fig. 10. Crack initiation and growth for 25  $\mu\text{m}$  thickness at three different levels of energy release rate a) 53  $\text{Jm}^{-2}$ , b) 62  $\text{Jm}^{-2}$  and c) 77  $\text{Jm}^{-2}$ .
- Fig. 11. Plot of normalized mean stress as a function of distance from crack tip [15].
- Fig. 12. Plot of normalized mode I fracture energy for crack extension by ductile fracture as a function of the non-dimensional quantity  $h/\chi_0$ : the experimental data obtained from Fig. 3 are superposed.

Fig. 13. Resistance curves predicted for interface cracks with bridging tractions [18]. Experimental data points from Fig. 3 are also shown:  $I$  is the moment of inertia of the beam and  $\Sigma$  is given by Eqn. (7).

Fig. A1 a) Scanning electron micrograph of pore with damage line made apparent by tilting,  $\psi = 70^\circ$ .  
b) Higher magnification SEM of edge of pore in (a).

Fig. A2 a) Cone rotated by  $\psi$  around axis  $bd$ .  
b) Cone rotated by  $\psi$  around axis  $bd$  and by  $\beta$  around axis  $fg$ .  
c) Ellipse showing rotations  $\psi$  and  $\beta$  (see text).

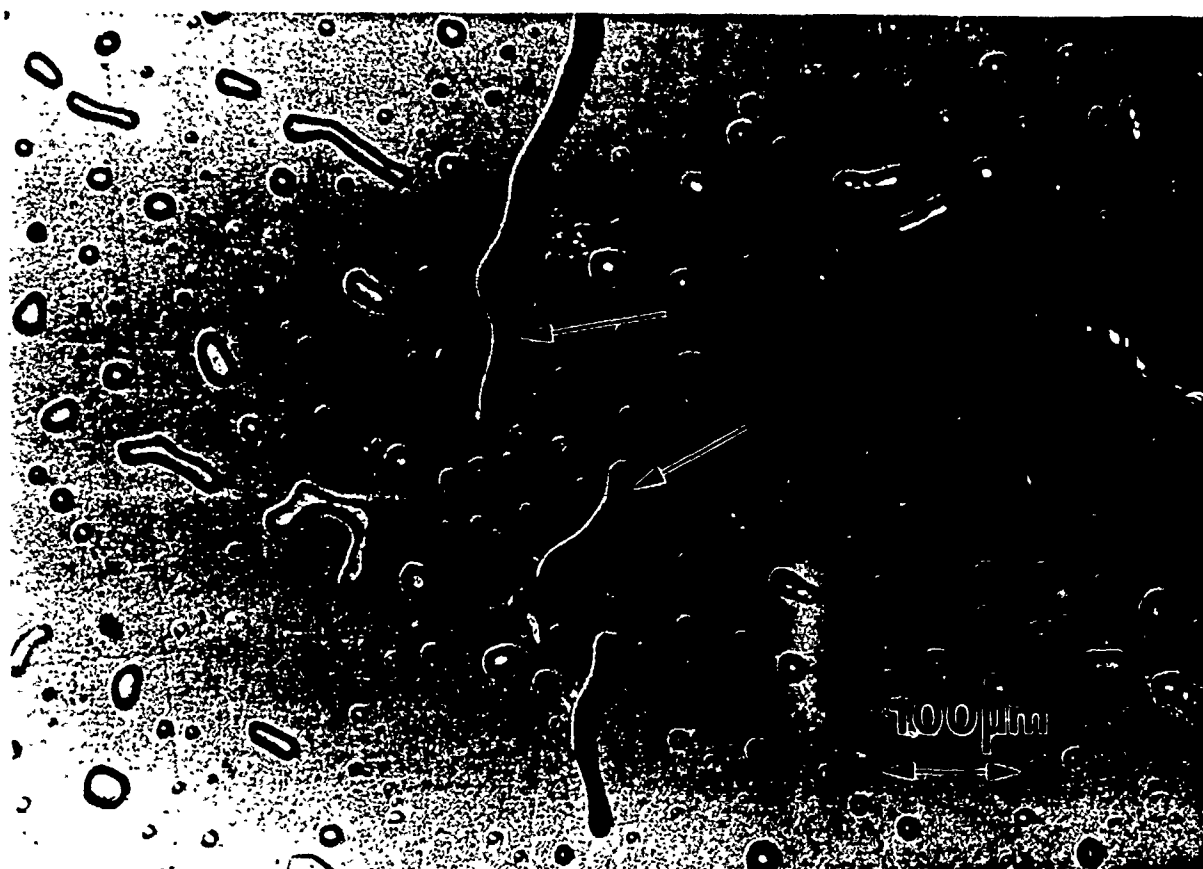


Fig. 1



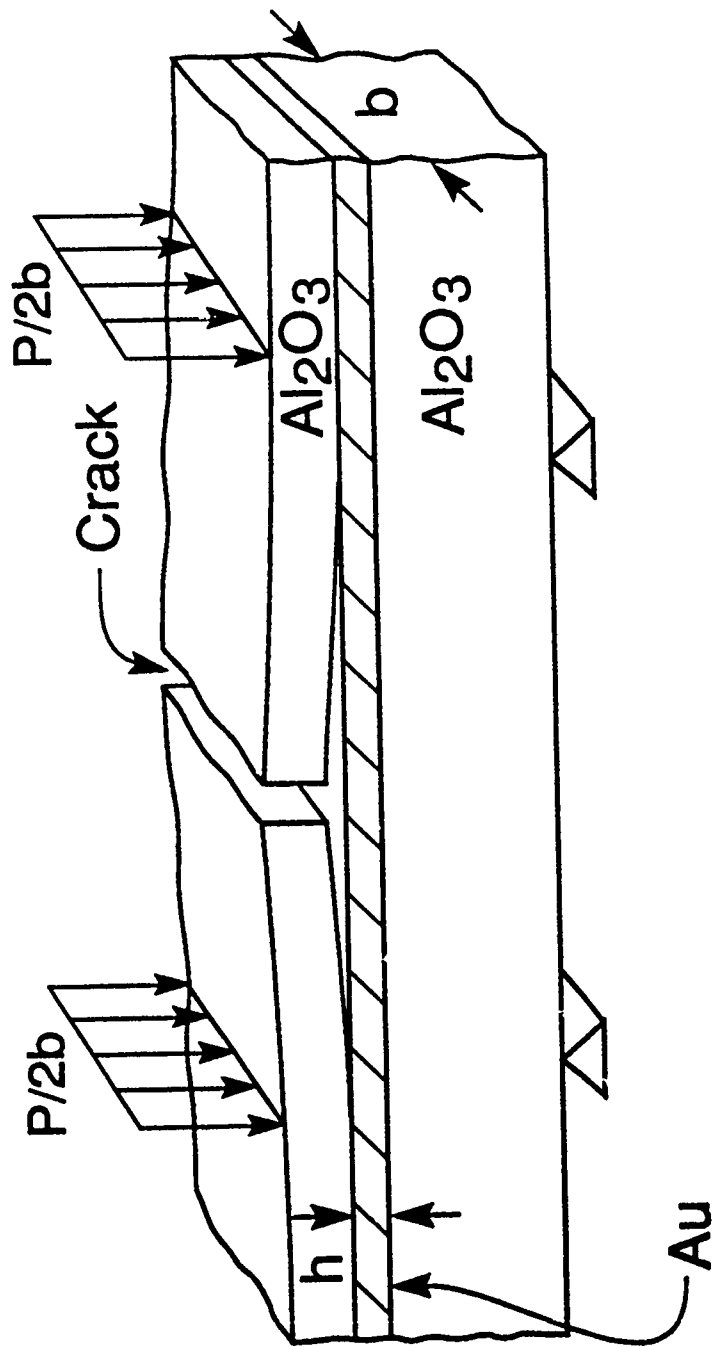


Fig. 2

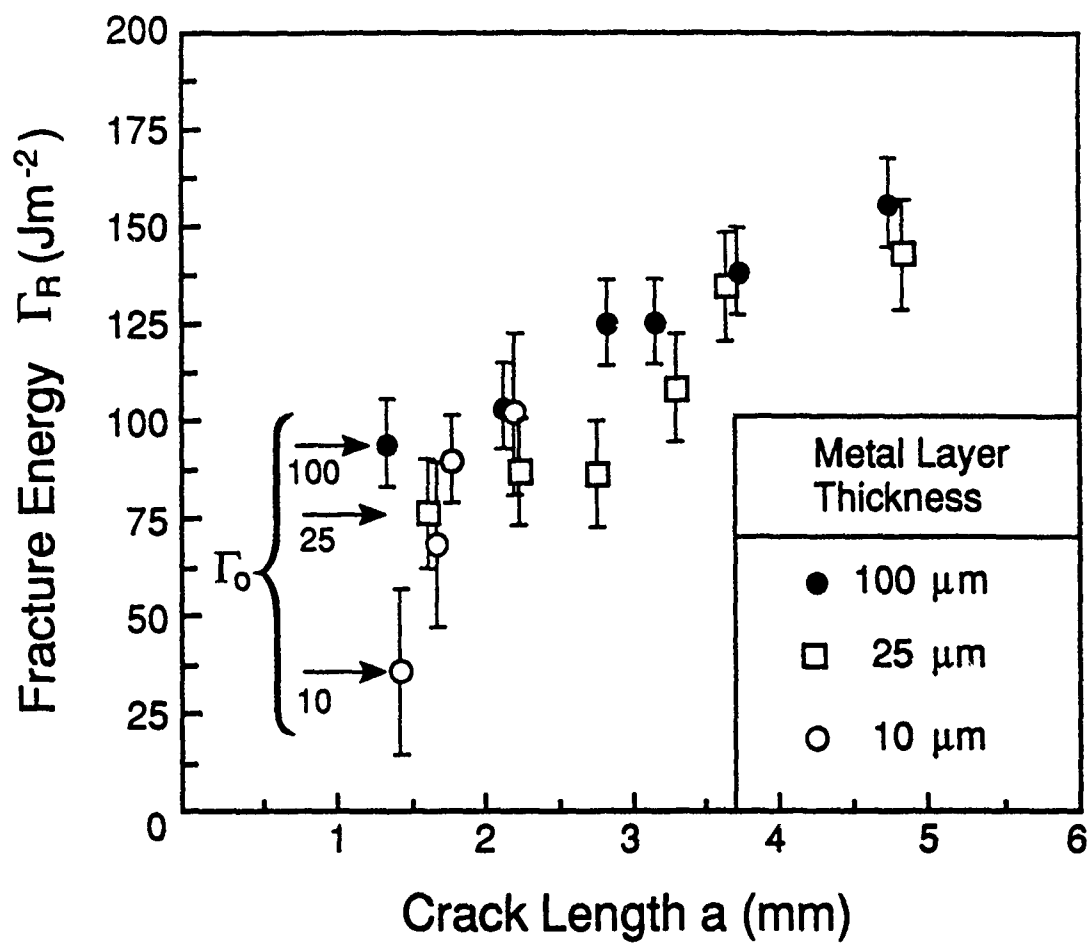


Fig. 3

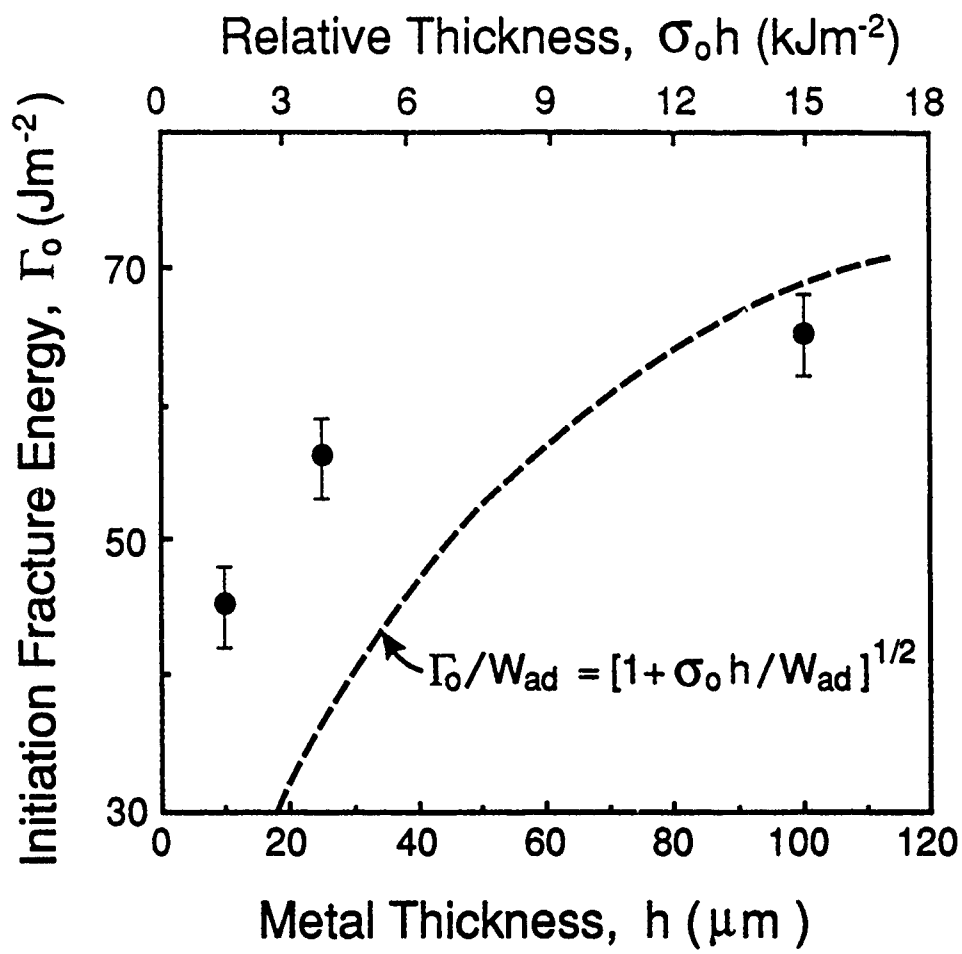


Fig. 4

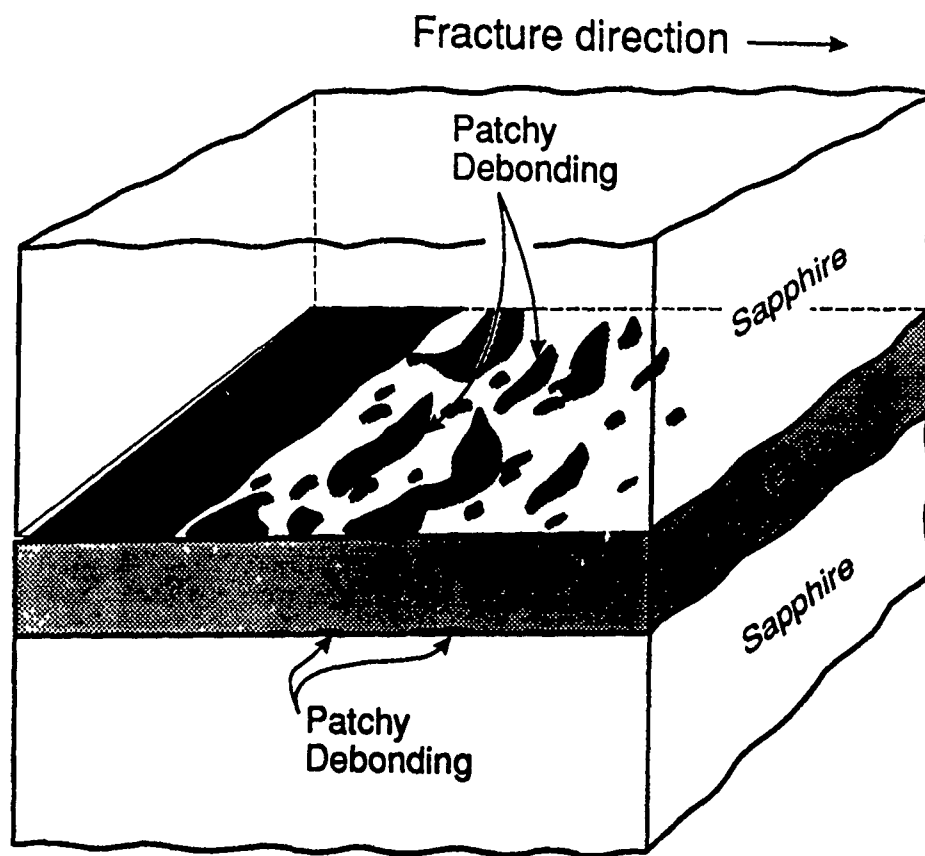
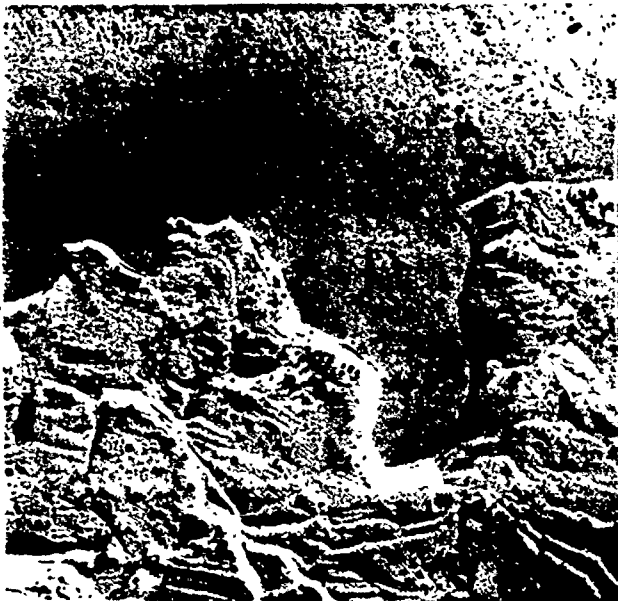
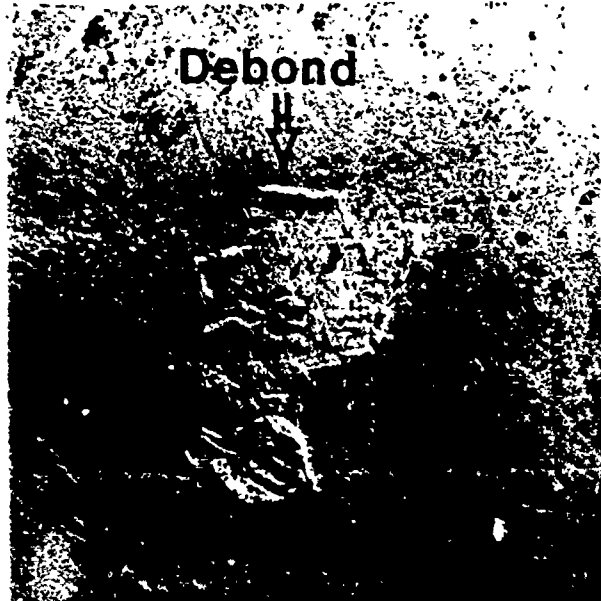


Fig. 5a

Crack  
front →



b) Upper Interface



c) Lower Interface

Fig. 5



Bonded Ligament



a)



Debonding  
Zone

b)

Fig. 7

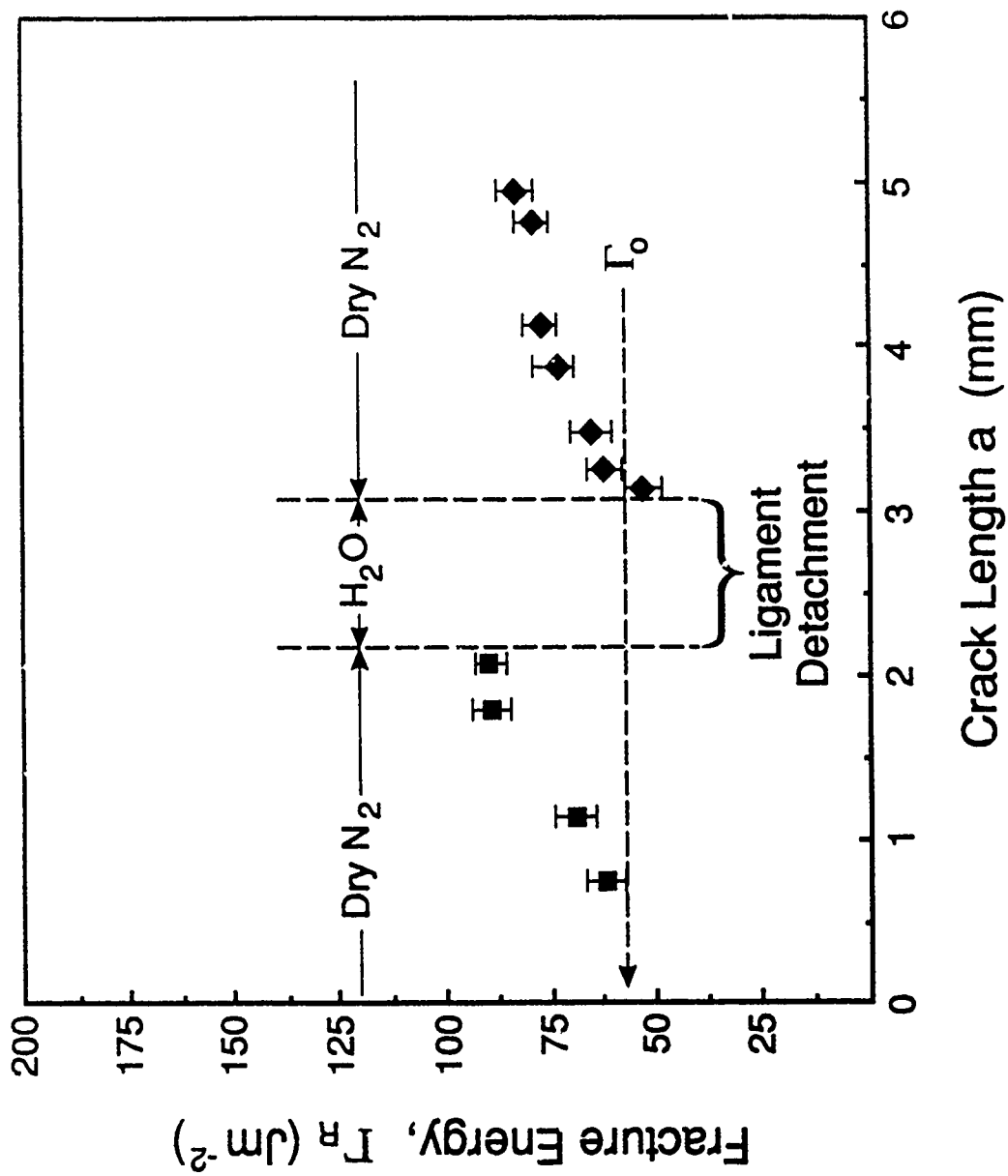


Fig. 8





a

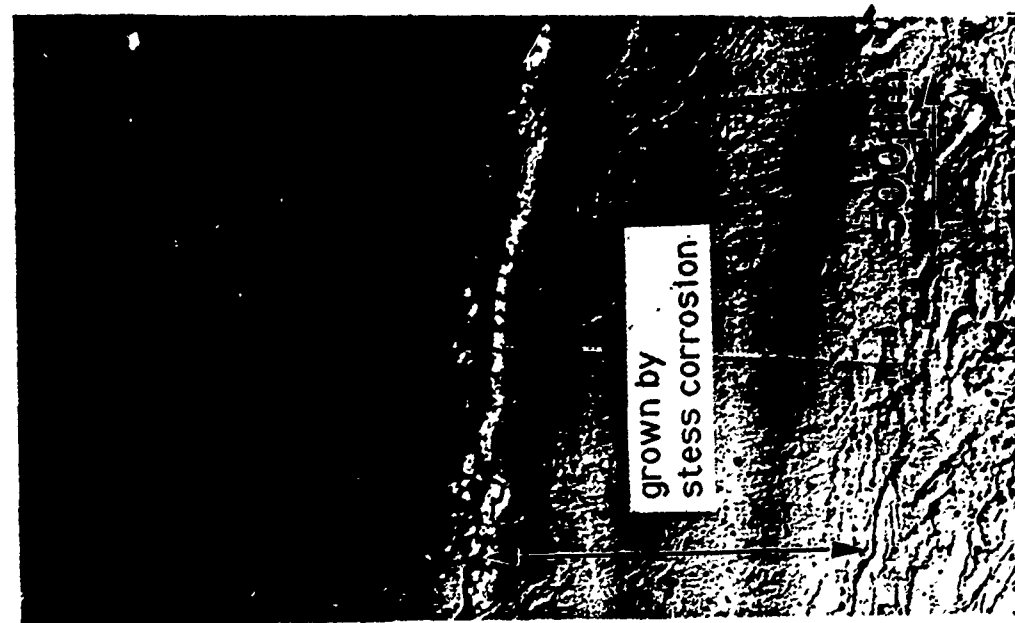
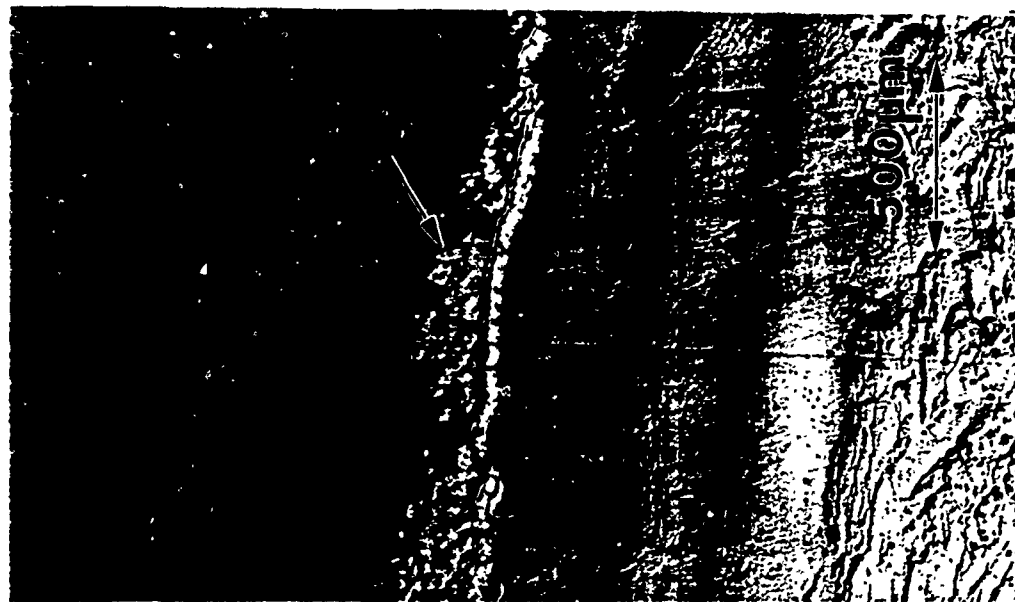
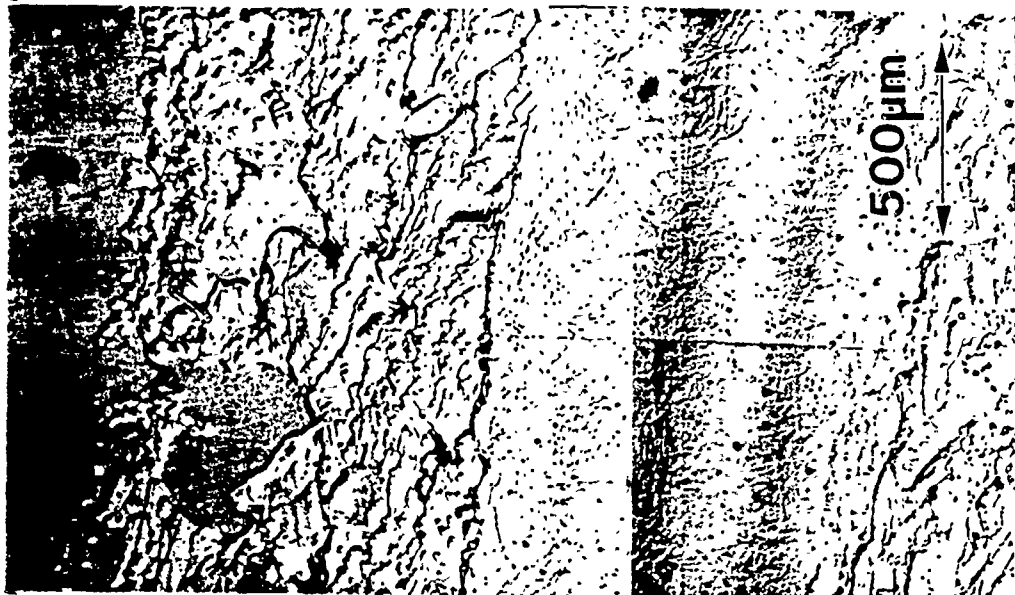


b



c

Fig. 9



a

b

c

Fig. 10

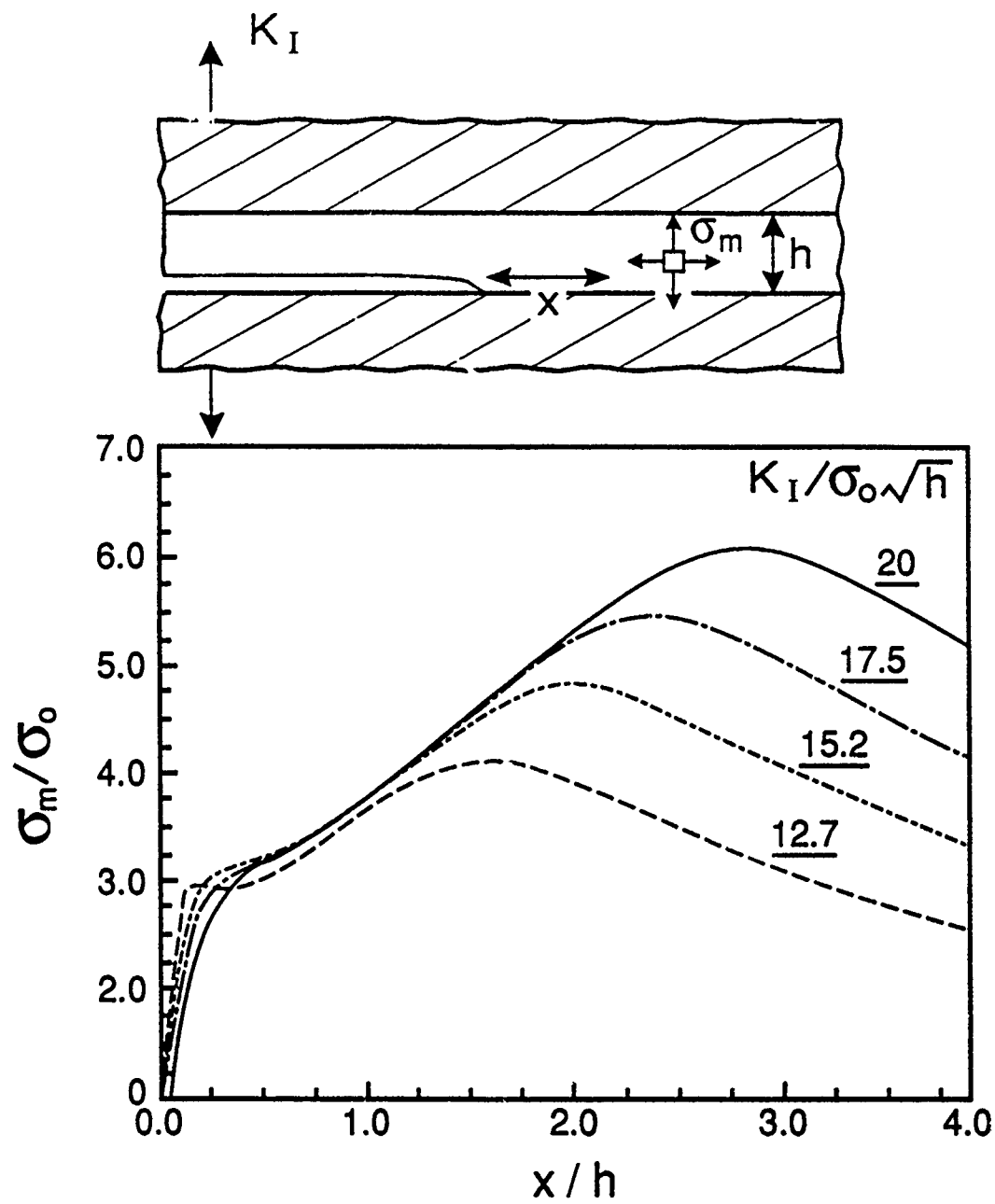


Fig. 11

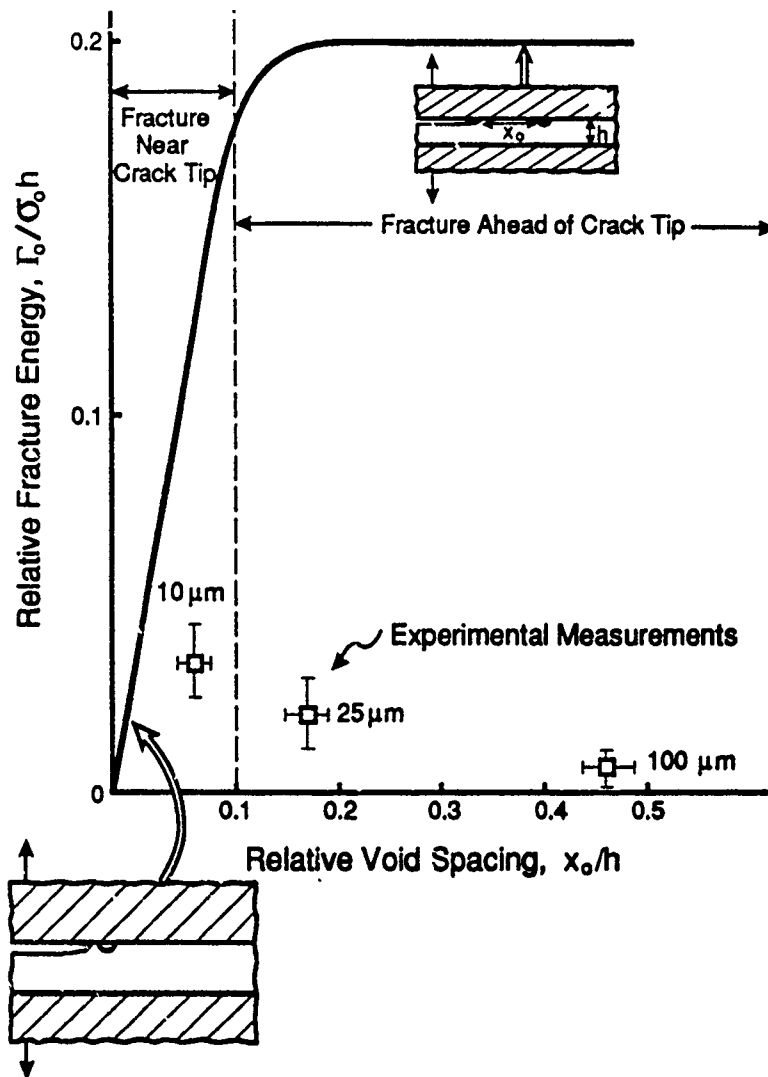


Fig. 12

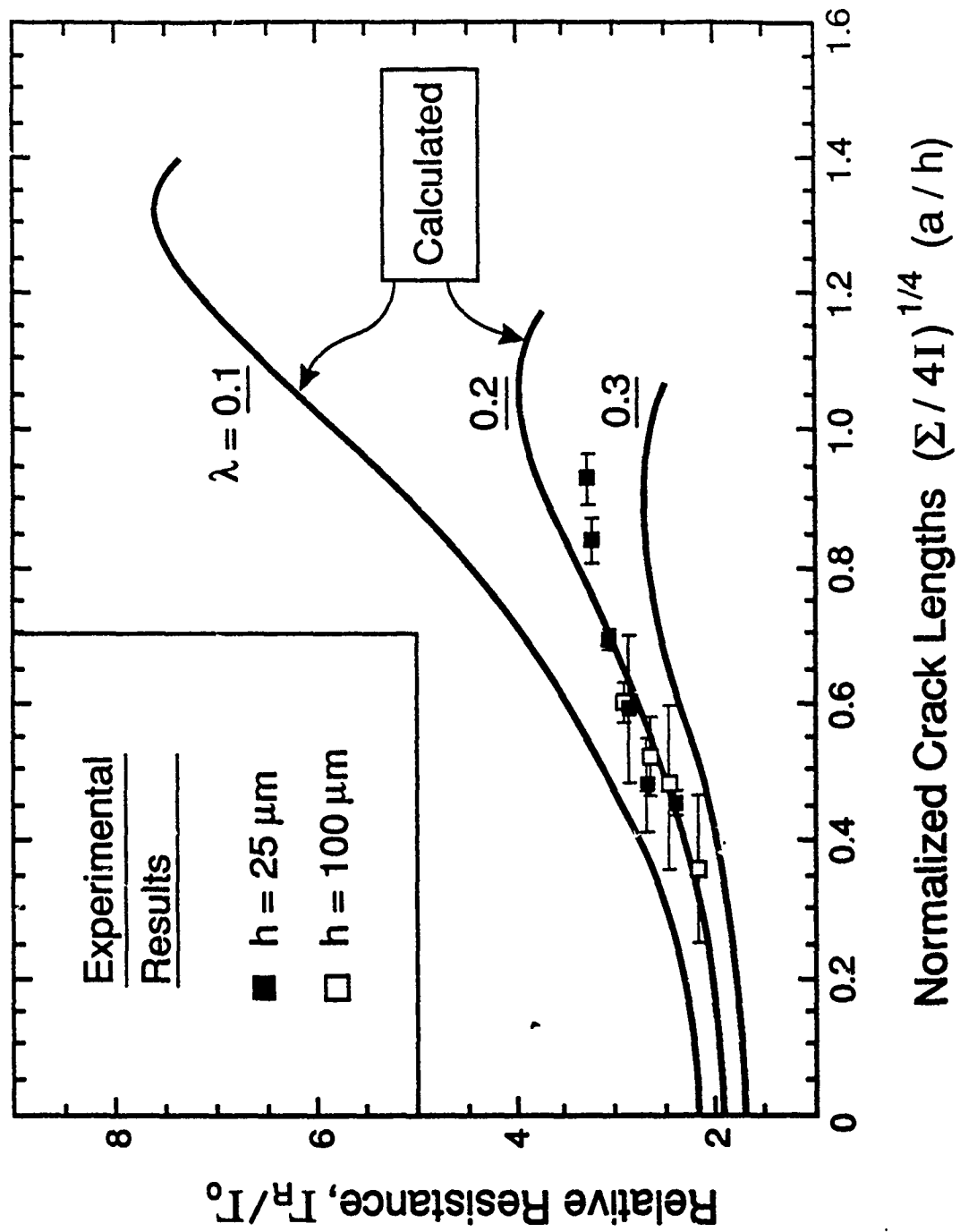


Fig. 13

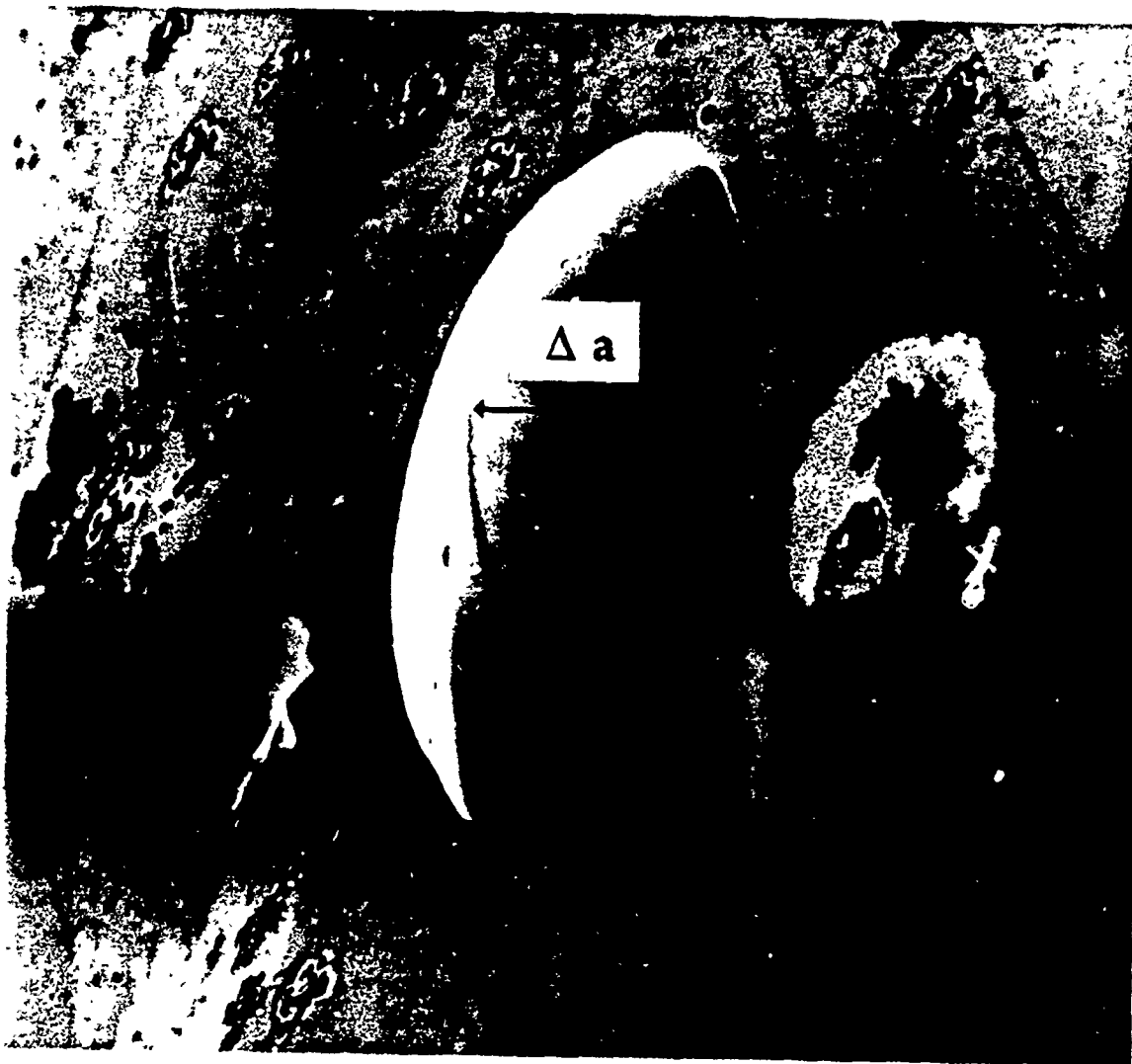


Fig. A1 a

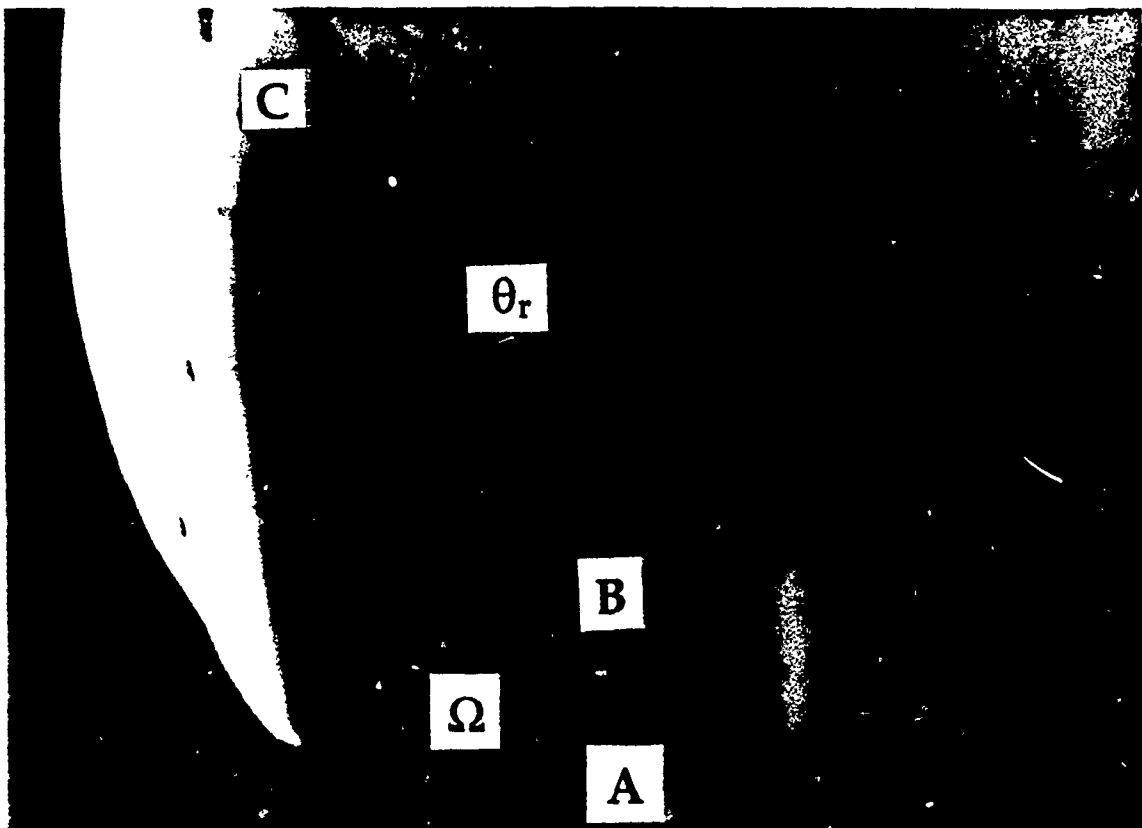
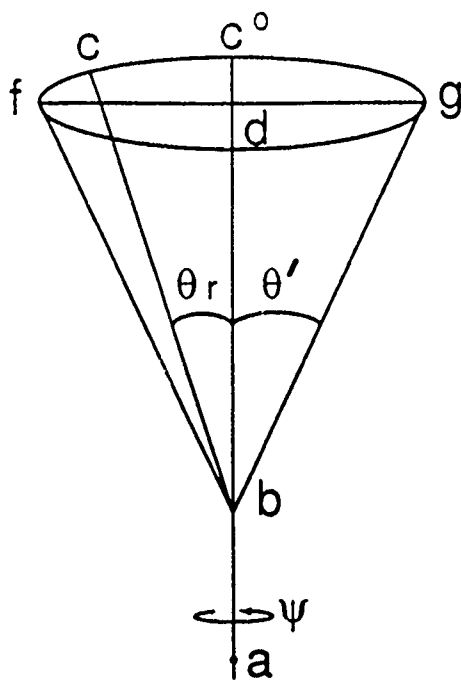
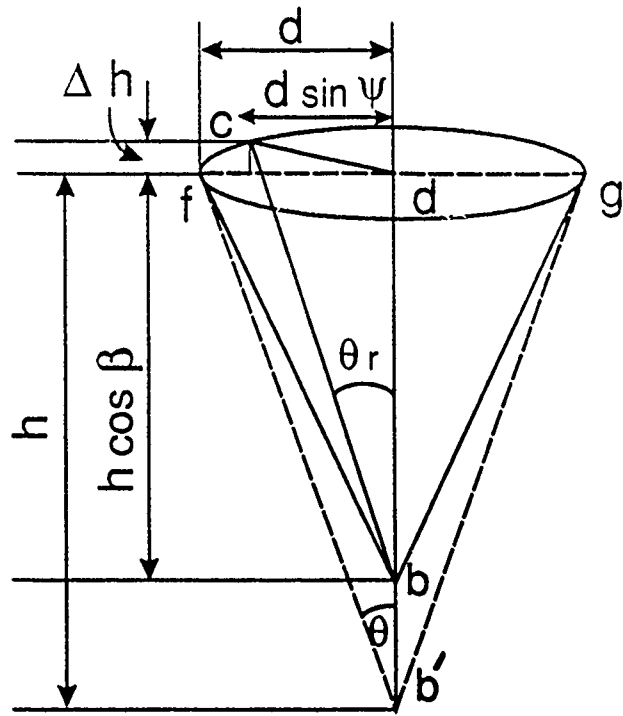


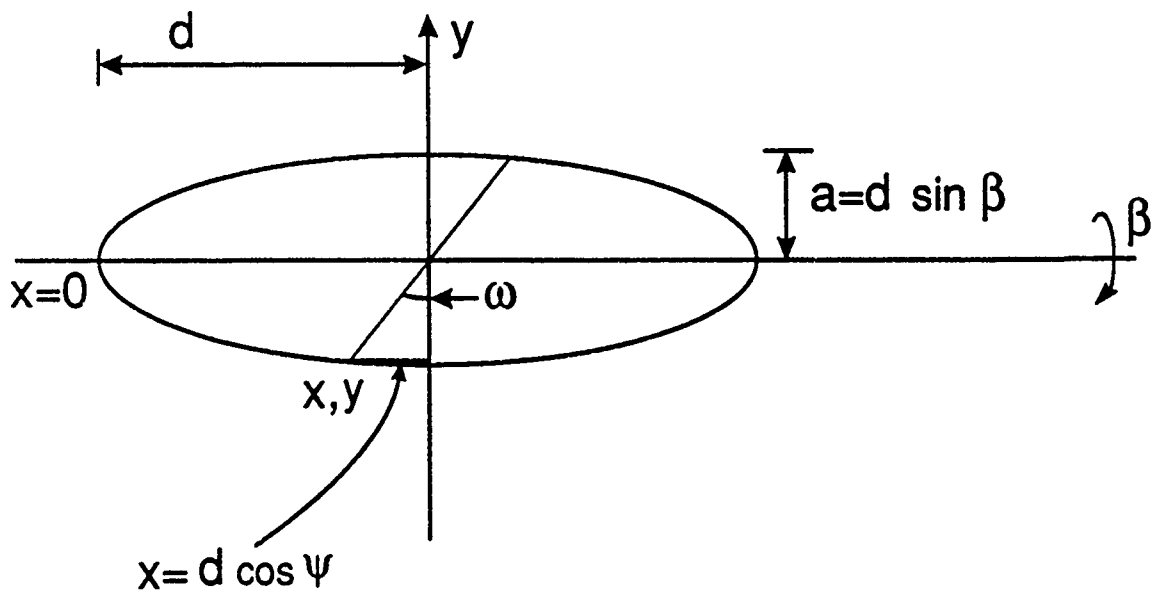
Fig. A1 b



a)



b)



c)

Fig. A2



# THE FRACTURE RESISTANCE OF METAL/CERAMIC/INTERMETALLIC INTERFACES

A. G. Evans, A. Bartlett, J. B. Davis, B. D. Flinn, M. Turner and I. E. Reimanis  
Materials Department, College of Engineering  
University of California, Santa Barbara, California 93106

## Introduction

A concerted effort on the mechanics of interface cracks (1-3), coupled with the development of test methods for measuring the interface fracture resistance (4, 5), has provided a framework for characterizing the mechanical properties of interfaces. There appear to be four governing issues (4, 6, 7). i) Interface fracture can be either brittle or ductile. ii) The fracture resistance is strongly influenced by the loading mixity, primarily through its influence on the crack path. iii) Crack growth by stress corrosion and by fatigue are commonly encountered. iv) The fracture resistance is substantially larger than the work of adhesion and is affected by plastic dissipation, as well as by interface non-planarity and by segregation. There are also appreciable geometric effects, such as the thickness of the metal present in laminates, adhesive bonds and fiber composites. In addition, residual stresses are typically involved and often provide an appreciable contribution to the energy release rate (8), as well as influencing the loading mixity (6).

There are major differences in interface fracture with the homologous temperature,  $T/T_m$ , used to produce the interface. Low homologous temperatures ( $T/T_m < 0.3$ ) processes such as evaporation result in interface mechanical properties dominated by impurities, especially organics present on the original surface prior to deposition (9). Consequently, thin bond layers, such as Cr and Ti, are often used to enhance the fracture resistance. The presence of these layers apparently results in the formation of carbides and hydrides that 'clean' the surface. The use of high homologous temperatures ( $T/T_m > 0.5$ ) generally results in 'strong' bonding for a wide range of metals, ceramics, intermetallics and glasses. Such diffusion bonds are emphasized in this article.

The fracture resistance of diffusion bonds can be influenced by the presence of reaction products. It is thus convenient to categorize interfaces in terms of their susceptibility to reaction product formation. An incomplete list of diffusion bonded interfaces that have been subject to *mechanical characterization* are summarized in Table I, together with the known incidence of reaction products. When reaction products form, cases have been found wherein cracks propagate within the product phase (10), and other cases wherein interface cracks extend between this phase and the parent material (11, 12), dependent on the system and the loading mixity.

A comprehensive review of the interface fracture processes associated with each system is not attempted here. Rather, the range of effects that can occur are illustrated from some of the systems presented in Table I. Consequently, the following sections are organized in accordance with present understanding of the dominant fracture mechanisms: ductile void growth, brittle debonding and decohesion, as well as combined void growth and debonding.

## Ductile Interface Fracture

Two systems are known to the authors in which fracture occurs by ductile void growth and coalescence in the metal near the interface. These are Al/Al<sub>2</sub>O<sub>3</sub> (13, 14) and Ti/Ti<sub>3</sub>Al/Al<sub>2</sub>O<sub>3</sub> (15). This mechanism involves void nucleation in the metal, typically at interface sites (Fig. 1a). For example, in Al/Al<sub>2</sub>O<sub>3</sub>, voids preferentially form at grain junctions in the Al<sub>2</sub>O<sub>3</sub> (14) (Fig. 1b). When this mechanism applies, there are several profound geometric effects on the mechanical fracture resistance: especially with regard to the metal layer thickness,  $h$ , and the loading mixity,  $\psi$ . The metal layer thickness enters through its influence on the stresses at the interface ahead of the crack (16) (Fig. 2). The trend is for these stresses to increase as  $h$  decreases, causing the fracture resistance  $\Gamma_R$  to diminish at small  $h$ . An extreme case is illustrated in Fig. 3 which demonstrates ductile void growth in a thin  $\alpha_2$ -Ti<sub>3</sub>Al layer formed between Ti(Ta)

and  $\text{Al}_2\text{O}_3$  (15). For this thin layer ( $h \approx 0.15 \mu\text{m}$ ), the fracture resistance  $\Gamma_R \approx 25 \text{ Jm}^{-2}$  is smaller than that for brittle interface fracture in many systems, as elaborated below. The spacing between void nucleation sites along the interface is also important and may dominate when this spacing is appreciably less than  $h$  (16).

The loading mixity is important because of the influence on the crack path (6). In particular, the loading that encourages the crack to deviate from the interface may induce cracking into the ceramic and prevents measurement of  $\Gamma_R$ . Measurements of  $\Gamma_R$  require careful consideration of test specimens having mixities that constrain the crack to remain at the interface, as exemplified by the flexure specimen depicted in Fig. 4 (17).

### Brittle Debonding and Decohesion

Brittle debonding of metal/ceramic interfaces formed by diffusion bonding has rarely been observed. The only example known to the authors is the  $\text{Al}_2\text{O}_3/\text{Mo}$  interface, which has a fracture energy,  $\Gamma_R \approx 3\text{--}4 \text{ Jm}^{-2}$  (Fig. 5) (18). There is also circumstantial evidence that  $\text{Al}_2\text{O}_3/\text{W}$  interfaces have a similarly low fracture resistance. However, even in these systems,  $\Gamma_R$  is appreciably larger than the thermodynamic work of adhesion,  $W_{ad}$ , indicating that dissipation mechanisms accompany interface fracture. The only other known example of brittle interface debonding occurs in the  $\text{Ti}(\text{Ta})/\text{Al}_2\text{O}_3$  system, when a  $\gamma$ -TiAl reaction product forms (12). In this case, fracture occurs at the interface between the parent  $\text{Al}_2\text{O}_3$  and the  $\gamma$ -TiAl reaction product (Fig. 6a), with a fracture energy,  $\Gamma_R \approx 17 \text{ Jm}^{-2}$ . This result contrasts with the behavior of diffusion bonded interfaces between  $\gamma$ -TiAl and  $\text{Al}_2\text{O}_3$  which are resistant to debonding (19) (Fig. 6b). Essentially all other interface fractures that involve debonding are accompanied by appreciably plastic dissipation in the metal, as elaborated below.

When brittle reaction products form and when thin brittle interlayers are used, brittle decohesion within the layer has been frequently observed. Examples include the  $\sigma$ -phase reaction product between  $\gamma$ -TiAl and Nb (10), as well as porous oxide interlayers between  $\text{Al}_2\text{O}_3$  and other materials (20). In such cases,  $\Gamma_R$  is dominated by the microstructure of the layer and the associated fracture resistance. The effects are exemplified by porous oxide interlayers, wherein  $\Gamma_R$  varies with the level of the porosity. The phenomenon is illustrated for  $\text{ZrO}_2$  interlayers in  $\text{Al}_2\text{O}_3$  (Fig. 7). For the porous interlayers (porosity  $\sim 30\%$ ) fracture occurs *within the layer*, with a fracture energy,  $\Gamma_R \approx 3\text{--}5 \text{ Jm}^{-2}$ . However, for the dense  $\text{ZrO}_2$  interlayer, fracture can be induced *at the interface* with a fracture energy,  $\Gamma_R \approx 15\text{--}20 \text{ Jm}^{-2}$ .

### Debonding with Plasticity

Many of the interfaces summarized in Table I involve debonding accompanied by plastic dissipation. These systems include  $\text{Al}_2\text{O}_3/\text{Au}$ ,  $\text{Al}_2\text{O}_3/\text{Pt}$  and  $\text{Al}_2\text{O}_3/\text{Nb}$ . Furthermore, the behavior is complicated by the incidence of stress corrosion (7), as well as by crack face bridging caused by metal ligaments (21, 22). The latter results in an interface fracture resistance that rises with crack extension (Fig. 8a). The rising resistance is well-described by plastic bridging models (23) (Fig. 8b). In the absence of stress corrosion caused by moisture, direct observations of interface crack extension (22) have revealed that the crack advances by the nucleation of debonds at the interface ahead of the crack (Fig. 9). These debonds grow by combined brittle debonding of the interface with plastic deformation and then coalesce to cause crack extension. This process occurs at a fracture resistance substantially lower than that expected for ductile fracture by plastic void growth. Models of this process have yet to be developed.

Moisture induced stress corrosion substantially reduces  $\Gamma_R$ , whereupon interface cracks grow with a characteristic growth rate that increases as  $\Gamma_R$  increases (7). This behavior is presumed to be analogous to that found in monolithic bodies. Furthermore, the nominal interface fracture resistance decreases as the metal layer thickness decreases (22) (Fig. 10), reflecting an important role of plastic dissipation in fracture, even through stress corrosion is occurring (7).

### Remarks

Some of the interface fracture phenomena evident in both metal/ceramic and metal/intermetallic interfaces have been briefly outlined. It is apparent that a rich spectrum of effects is involved, analogous to fracture in monolithic materials. While a start has been made, a systematic experimental effort is needed to characterize the range of fracture behaviors, along with the development of models that relate to each important fracture mechanism. Important issues that have not been addressed in this brief survey include effects of mode mixity on  $\Gamma_R$  and fatigue crack growth at interfaces.

TABLE I  
Interfaces That Have Been Subject to Mechanical Characterization

METAL	CERAMIC-INTERMETALLIC	KNOWN REACTION PRODUCTS
Al	Al <sub>2</sub> O <sub>3</sub>	None
Au	Al <sub>2</sub> O <sub>3</sub>	None
Nb	Al <sub>2</sub> O <sub>3</sub>	None
Mo	Al <sub>2</sub> O <sub>3</sub>	None
W	Al <sub>2</sub> O <sub>3</sub>	None
Ti	Al <sub>2</sub> O <sub>3</sub>	γ-TiAl α <sub>2</sub> -Ti <sub>3</sub> Al
Al	SiC	Al <sub>4</sub> C
Al(Si)	SiC	None
Al(Mg)	Al <sub>2</sub> O <sub>3</sub>	Spinel
Ti(Ta)	Al <sub>2</sub> O <sub>3</sub>	γ-TiAl α <sub>2</sub> -Ti <sub>3</sub> Al σ-phase
Pt	Al <sub>2</sub> O <sub>3</sub>	Pt <sub>3</sub> Al
Nb	γ-TiAl	T <sub>2</sub> , σ-phase
TiNb	γ-TiAl	α <sub>2</sub> -Ti <sub>3</sub> Al
Nb	MoSi <sub>2</sub>	(NbMo) <sub>5</sub> Si <sub>3</sub>
Cu	SiO <sub>2</sub>	None

### References

1. J. W. Hutchinson, *Metal/Ceramic Interfaces* (Ed., M. Rühle et al.) Pergamon (1990).
2. Z. Suo, this volume.
3. J. W. Hutchinson and Z. Suo, *Advances in Applied Mech.*, vol. 28 (1991).
4. A. G. Evans, B. J. Dalgleish, P. G. Charalambides and M. Rühle, *Mtls. Sci. and Engr.*, A R6 (1990) 53.
5. J. S. Wang and Z. Suo, *Acta Metall.*, 38 (1990) 1279.
6. A. G. Evans, M. Y. He and J. W. Hutchinson, *Acta Metall.*, 37 (1989) 3249.
7. I. E. Reimanis, B. J. Dalgleish, M. Brahy, M. Rühle and A. G. Evans, *Acta Metall. Mater.*, in press.
8. P. G. Charalambides, H. C. Cao, J. Lund and A. G. Evans, *Mech. of Mtls.*, 8 (1990) 269.
9. R. M. Cannon, R. Fisher and A. G. Evans, *MRS Proceedings* (1986) 799.
10. H. E. Dève, A. G. Evans, G. R. Odette, R. Mehrabian, M. L. Emiliani and R. J. Hecht, *Acta Metall. Mater.*, 38 [8] (1990).
11. A. Bartlett, M. Rühle and A. G. Evans, *Acta Metall. Mater.*, in press.
12. M. Y. He, A. Bartlett and J. W. Hutchinson, *J. Am. Ceram. Soc.*, in press.
13. B. J. Dalgleish, K. P. Trumble and A. G. Evans, *Acta Metall.*, 37 [7] (1989).
14. B. D. Flinn, F. W. Zok, F. F. Lange and A. G. Evans, *Proc. 1990 ASM/TSM Fall Meeting*, in press.
15. A. Bartlett and A. G. Evans, to be published.
16. A. G. Varias, Z. Suo and C. F. Shih, *Mechanics and Phys. of Solids*, in press.
17. P. G. Charalambides, J. Lund, R. M. McMeeking and A. G. Evans, *Jnl. Appl. Mech.*, 56 (1989) 77.
18. J. B. Davis, G. Bao, H. C. Cao and A. G. Evans, *Acta Metall. Mater.*, in press.
19. M. L. Emiliani, R. J. Hecht, H. E. Dève, J. B. Davis and A. G. Evans, to be published.
20. J. B. Davis, E. Bischoff and A. G. Evans, to be published in *Proceedings of the Symposium on Ceramic, Polymer and Metal Matrix Composites*, Am. Cer. Soc. (Nov. 1990).
21. T. S. Oh, R. M. Cannon and R. O. Ritchie, *J. Am. Ceram. Soc.*, 70 [12] C-352-C-355 (1987).
22. I. E. Reimanis and A. G. Evans, *Acta Metall. Mater.*, to be published.
23. G. Bao, B. Fan and A. G. Evans, *Mech. of Mtls.*, in press.

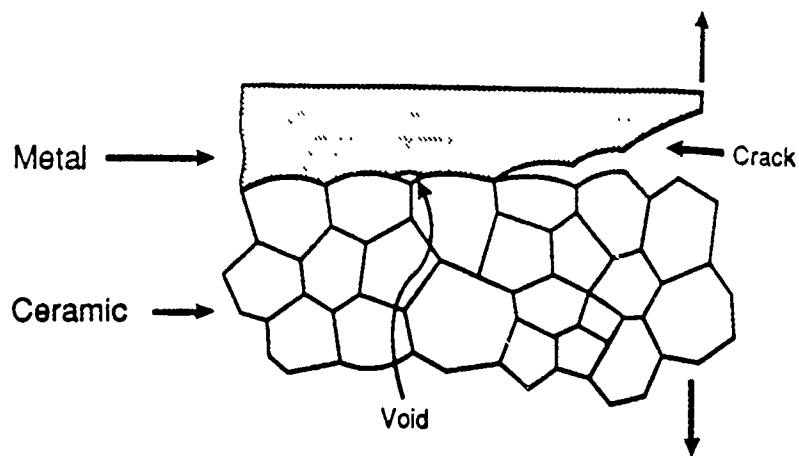


Fig. 1. a) A schematic of interface fracture by void growth.



- b) A fracture surface of an Al/Al<sub>2</sub>O<sub>3</sub> specimen indicating Al ridges formed by plastic void coalescence. Note that virtually all of the ridges surround three-grain junctions in the Al<sub>2</sub>O<sub>3</sub> which act as void nuclei.

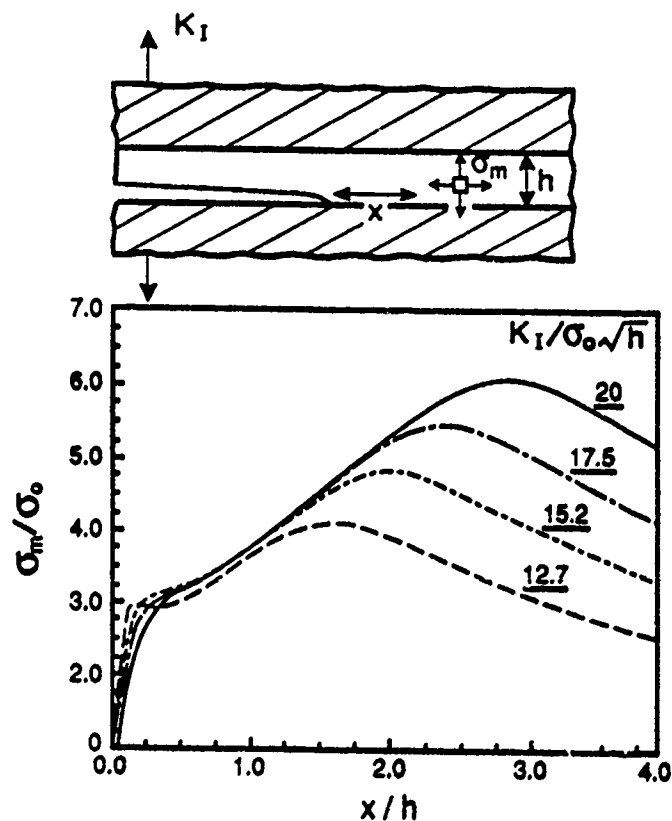


Fig. 2. Stresses at the interface ahead of a crack for a thin metal layer between two brittle solids.

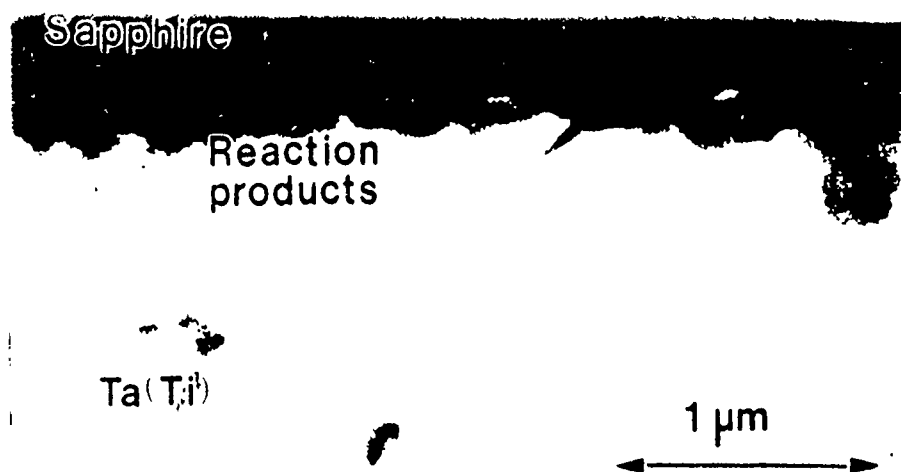


Fig. 3. Fracture by ductile void growth within a thin  $\alpha_2$ -Ti<sub>3</sub>Al reaction product layer found between Al<sub>2</sub>O<sub>3</sub> and Ti(Ta).

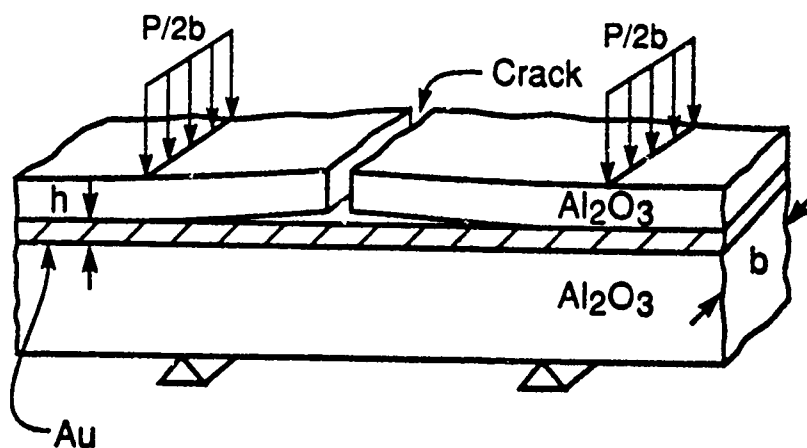


Fig. 4. A mixed mode flexure specimen for measuring the interface fracture resistance that constrain crack extension to occur along the interface.

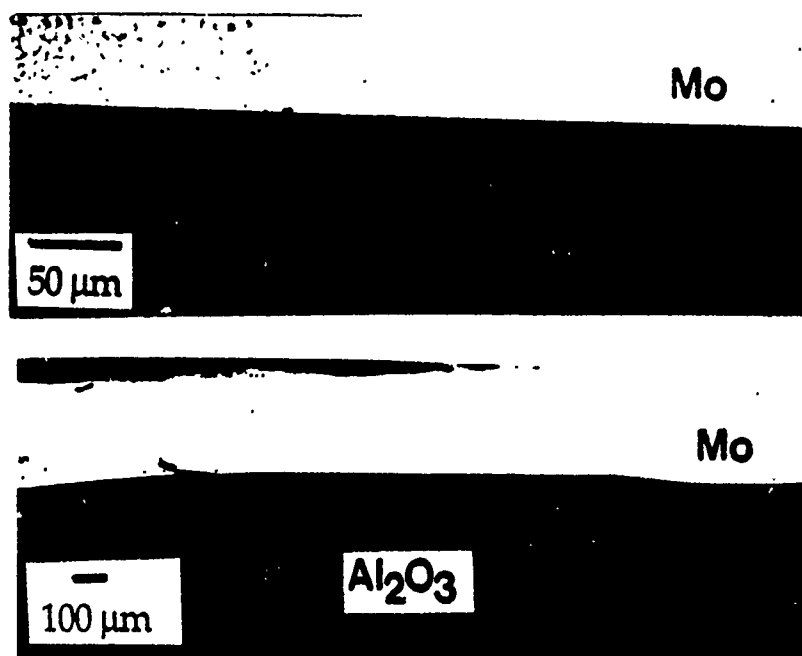


Fig. 5. An interface debond between Mo and Al<sub>2</sub>O<sub>3</sub>.

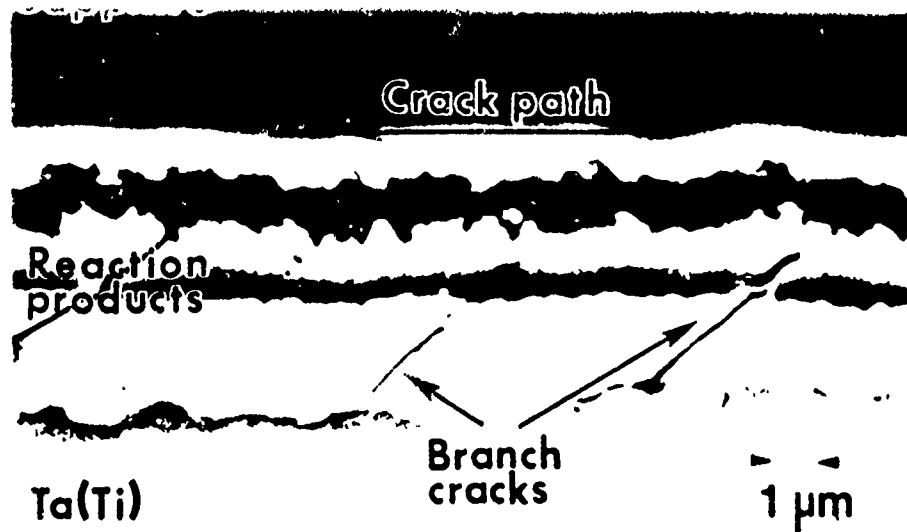
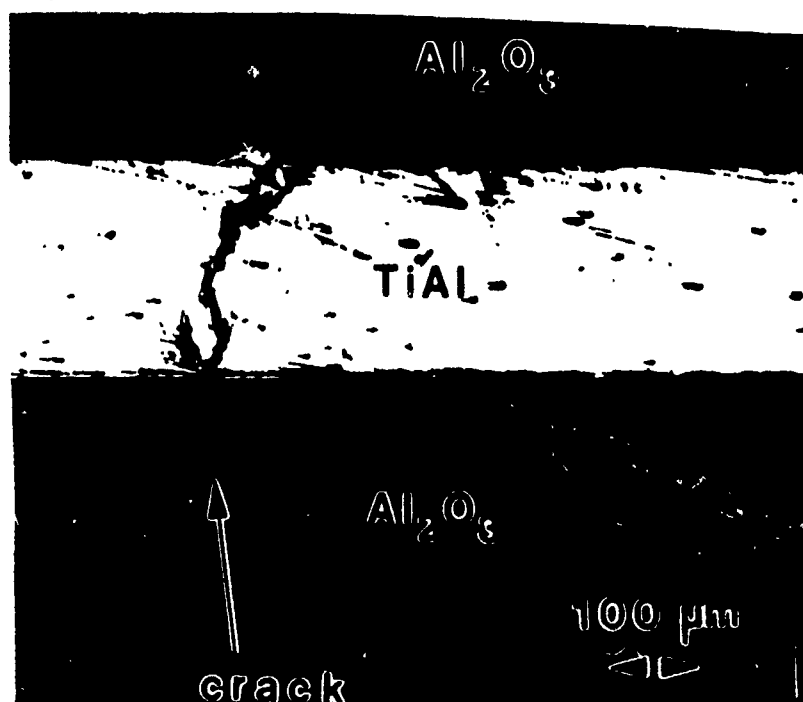


Fig. 6. a) Interface debonding between a  $\gamma$ -TiAl reaction product layer and  $\text{Al}_2\text{O}_3$ ; note the branch cracks in the reaction layer.



b) Crack extension across the interface, without debonding, in a diffusion brittle  $\gamma$ -TiAl/ $\text{Al}_2\text{O}_3$  specimen.

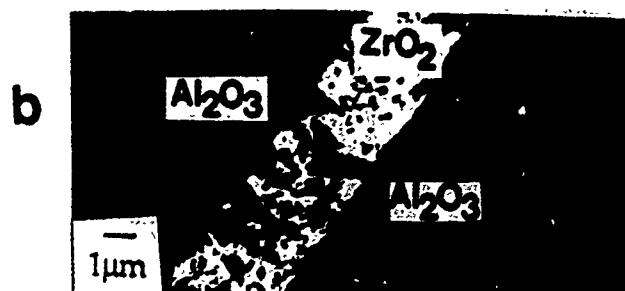
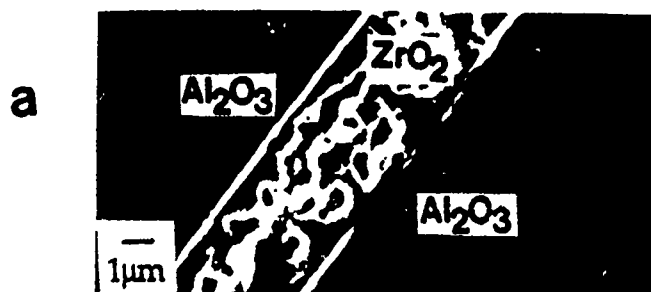


Fig. 7. SEM micrograph of  $\text{ZrO}_2$  interfaces on  $\text{Al}_2\text{O}_3$  (a) porous interlayer that fractures through the layer with  $\Gamma_R \approx 4 \text{ Jm}^{-2}$  (b) dense interlayers that fracture at the interface with  $\Gamma_R \approx 20 \text{ Jm}^{-2}$ .

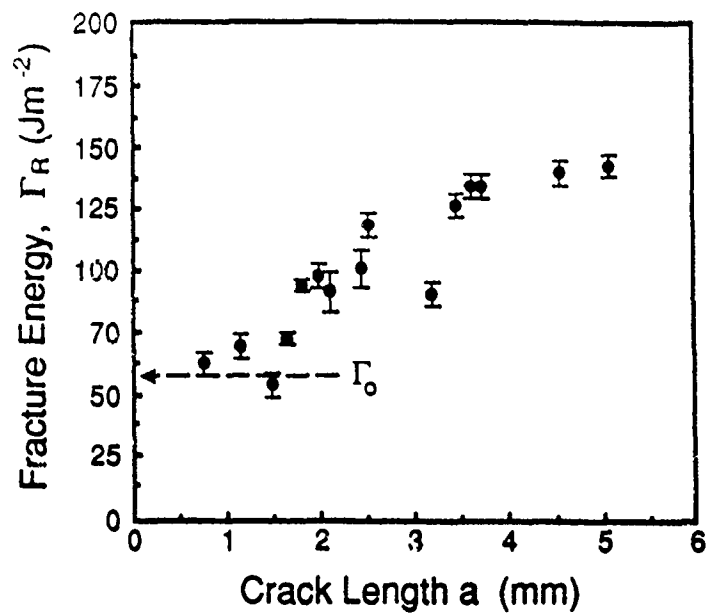


Fig. 8. a) A resistance curve for the Au/Al<sub>2</sub>O<sub>3</sub> interface measured in a dry atmosphere.

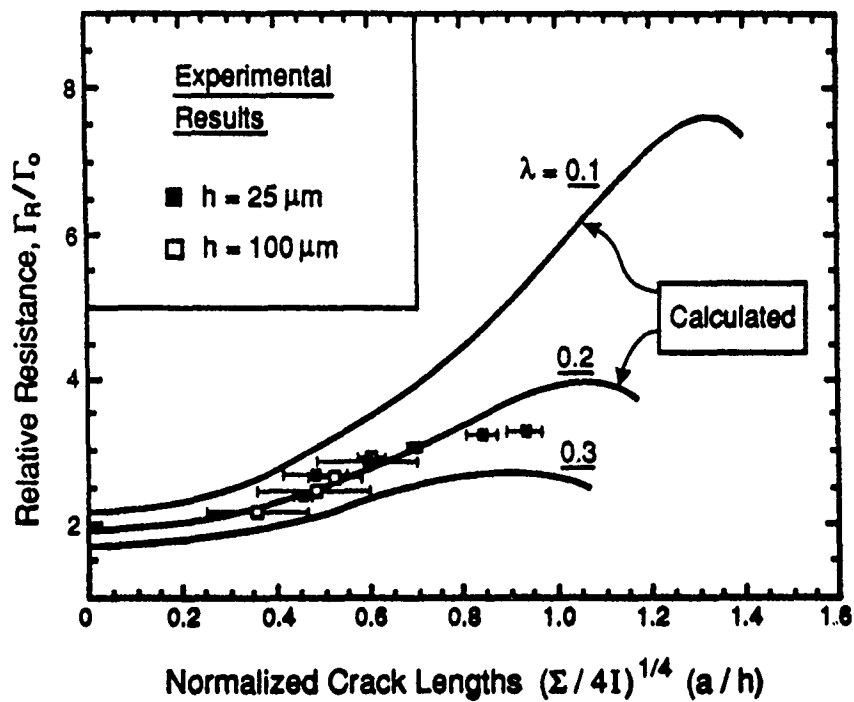


Fig. 8. b) A comparison of the measured resistance curve for Au/Al<sub>2</sub>O<sub>3</sub> with calculations based on a ligament model.

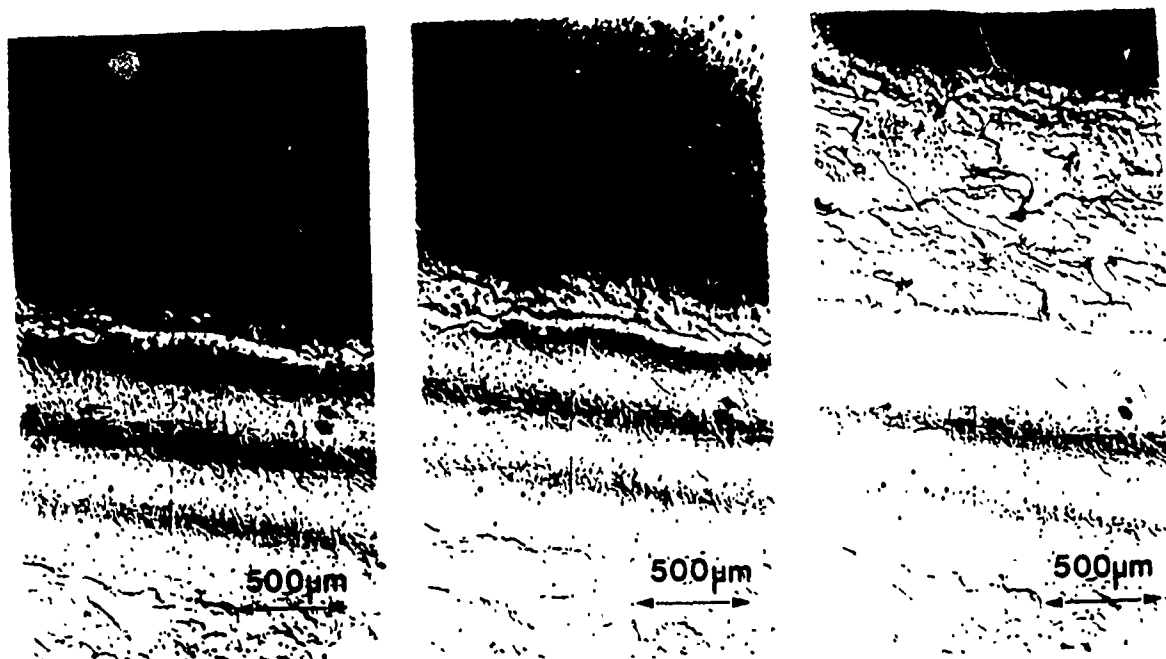


Fig. 9. A sequence showing the crack advance mechanism at the Au/Al<sub>2</sub>O<sub>3</sub> interface tested in a dry atmosphere.

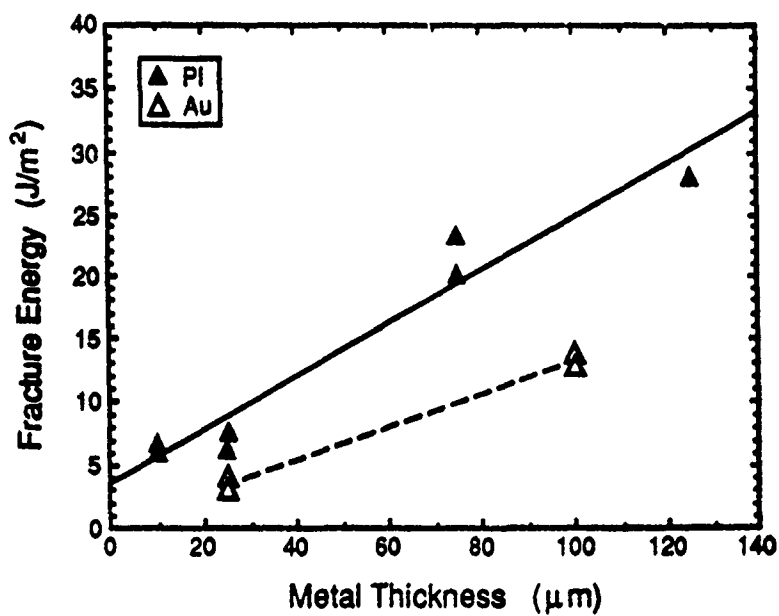


Fig. 10. Trends in the nominal fracture resistance with metal layer thickness for tests conducted in air.



## Powder Processing of Ceramic Matrix Composites

F. F. Lange, D. C. C. Lam, O. Sudre, B. D. Flinn, C. Folsom,  
B. V. Velamakanni, F. W. Zok, and A. G. Evans

Materials Department  
College of Engineering  
University of California at Santa Barbara  
Santa Barbara, CA 93106

### ABSTRACT

Powder processing of ceramic matrix composites is reviewed with emphasis on 1) forming powder compacts containing reinforcements, 2) effect of the reinforcement network on the shrinkage and strengthening of the powder matrix during a heat treatment, 3) a novel method for producing a metal reinforced ceramic composite and 4) a novel method for producing a laminar ceramic composite containing brittle fibers. Preliminary properties for the two new composite processing methods are given.

REINFORCEMENTS ARE INCORPORATED INTO CERAMICS to increase the fracture toughness of the ceramic matrix, impart R-Curve behavior (toughness increases as the crack grows) and to provide a material that fails at high strains. To realize these properties, the reinforcements must act as bridges behind an extending crack. The extending crack must bypass the reinforcement and the bridging reinforcements must dissipate work as they act as bridges. Analytical fracture models are relatively well developed to indicate how these behavior can be achieved, whereas processing methods are still under development.

Non-powder processing methods for making ceramic matrix composites via infiltration of the matrix into reinforcement preforms have been reviewed by Jamet et al.<sup>1</sup> and Naslain.<sup>2</sup> They include cyclic chemical vapor infiltration/deposition (CVI), cyclic sol-gel infiltration/heat treatment, and cyclic organometallic infiltration/pyrolysis. Molten metals are also infiltrated into partially sintered powder compacts.<sup>3</sup> In addition, several different ceramic matrices can be 'grown' into fiber

preforms via an environmental reaction method (e.g., the oxidation of certain aluminium alloys<sup>4</sup>) under development by the Lanxide Corporation. These methods can be synergistically used with powder methods.

Powder processing of composites involves three critical issues: 1) incorporating and consolidating powder-reinforcement systems, 2) making the powder matrix strong, and 3) controlling the matrix/reinforcement interface toughness and frictional characteristics. This review will focus on our current understanding of the first two issues, and then review the current progress concerning two new composite processing methods in which reinforcements are added after the ceramic matrix is made dense.

### PACKING COMPOSITE POWDERS

As reviewed elsewhere,<sup>5</sup> the problem of how ceramic fibers (and whiskers) can be incorporated into ceramic powders is at an advanced stage of understanding. It is understood that the particles in the powder matrix must have the highest packing density possible.<sup>6</sup> It is known that the highest packing density is achieved when:<sup>7</sup> a) repulsive forces exist between particles, a condition that requires colloidal powder processing and consolidation methods, b) a powder has an optimum particle size distribution that contains ~ 30 vol % of much smaller particles relative to ~ 70 vol % of larger particles, and c) mass segregation does not occur as the particles are packed to form the desired shape. It is also known that fibers and whiskers can lower the packing density of the matrix particles.<sup>8</sup> Fiber surfaces and positions where fibers touch one another lower the packing efficiency of matrix particles. Both of these effects depend on the particle size to fiber diameter ratio. Namely, smaller particles can pack more efficiently around the fiber surface and in the volume region

defined by touching fibers, much better than larger particles.<sup>3</sup> For these reasons, the particle size to fiber diameter ratio must be  $\leq 0.02$ . Powders with very small particles, relative to the fiber diameter, are needed to obtain a high particle packing density.

Since interparticle forces must be controlled to achieve high particle packing densities, slurry (particle-liquid systems) methods must be used to either consolidate mixtures of powders and whiskers, or pack powders within fiber preforms. These methods include either pressure filtration or centrifugation.<sup>9</sup> Provided that the slurry's viscosity is very high to prevent mass segregation, whiskers or chopped fibers can be mixed into the slurry to be consolidated by pressure filtration. Although attractive interparticle forces produce a slurry with sufficient viscosity to prevent mass segregation due to sedimentation, problems can be encountered due to differential strain recovery as reviewed below. In addition, flocced slurries do not produce high packing densities. All current evidence suggests that 'coagulated' slurries overcome the problem of mass segregation, pack to a high density, and will avoid the problems of strain recovery associated with flocced slurries.<sup>10</sup> Coagulated systems are produced by adding salt to a slurry containing charged particles. Hydrated counter ions surround the particles to neutralize the surface charge, diminish the particle's electrostatic repulsive potential, but produce a short range repulsive, hydration potential that prevent the attractive particles from touching one another. Particles in coagulated slurries attempt to sit in a weak, attractive potential well; the depth of the well is controlled by the amount of salt added to the system. The viscosity of coagulated slurries depends on the depth of the potential well, which is controlled by the salt content. Because coagulated particles attempt to repel one another when pushed together, they pack to their highest packing density by sliding over one another during rearrangement. This newly discovered<sup>10</sup> use of short range, repulsive hydration forces to increase slurry viscosity without hindering packing potential, appears significant for the consolidation of many composite slurry systems.

### CONSTRAINED DENSIFICATION

It is interesting to note that the composites produced by the French Aerospace Company, SEP, via the CVI process contain approximately 10 to 15 % porosity. Since these composites also contain ~ 40 vol % fibers (either Nicalon SiC or Carbon), the matrix phase is only 75 to 83 % dense. Despite their low matrix density, these composites, when coated to avoid internal oxidation, are a commercial success because they survive and perform critical engineering tasks not met by conventional materials. Although the success of the SEP material

teaches us that ceramic matrix composites need not be fully dense, most of the processing research concerning ceramic matrix composites is directed to make the matrix phase fully dense with the belief that denser composites will produce a higher strength and more reliable material.

It is widely recognized that the densification behavior of a crystalline powder can be dramatically influenced by an inert (non-densifying) second phase. The second phase can be either particles, whiskers or fibers. The phenomena associated with this effect appears to limit the pressureless processing of many composite systems and causes the composite processor to resort to deformation processing, viz. hot-pressing and HIPing to fully densify the matrix phase. Deformation processing certainly must be avoided if composites are to be engineered with reinforcements architecturally situated along principal stress trajectories.

In general, powder compacts are made strong by a heat treatment that promotes densification. Since the void phase is removed during densification, the powder compact shrinks. De Jonghe and coworkers<sup>11</sup> were the first to systematically characterize the fact that an inert inclusion phase will constrain densification. They demonstrate that a very small volume fraction (0.03) of inclusions would significantly limit the densification behavior of a composite powder compact. Their isothermal data for a ZnO powder, SiC inclusion composite system showed that the densification rate decreases with increasing volume fraction of SiC inclusions. Bordia and Raj<sup>12</sup> have reported similar data for TiO<sub>2</sub> powder containing Al<sub>2</sub>O<sub>3</sub> inclusions. Brook et al.,<sup>13</sup> reporting similar data for Al<sub>2</sub>O<sub>3</sub> powder containing dense, Al<sub>2</sub>O<sub>3</sub> inclusions. None of these observations are predicted by a model developed by Onoda and Messing<sup>14</sup> which suggested that inclusions would not affect densification until they were about to form a connective network at larger volume fractions.

Initial models<sup>15,16</sup> to explain the densification behavior of mixed powder-inclusion systems assumed the shrinking powder place the inert particles in a state of compression. The inclusions, in turn, would lower the sintering 'stress' of the powder by placing the matrix powder in a state of hydrostatic tensile stress. Although these initial models were mathematically appealing, Scherer<sup>17</sup> pointed out that the parameters needed to fit data were unreasonable with respect to the mechanics of the problem. He also indicated that the mean hydrostatic stress that might develop within the powder is much smaller than required by the models. In addition, neither model predicts the densification behavior at higher inclusion fractions (either closely spaced or touching), nor do they predict an end point density less than theoretical.

On the experimental side, Lange<sup>18</sup> showed that an isolated inclusion would not constrain the densification of the surrounding matrix as predicted by the initial models. Experiments<sup>19</sup> with alumina powders containing a moderate volume fraction of silicon carbide whiskers showed that the powder within the whisker network did shrink and densify onto the whisker network but the whisker network itself did not shrink. That is, the relatively rigid whisker network constrains composite shrinkage, but does not prevent the powder within the network from shrinking. Namely, as voids within portions of the densifying powder disappear, their volume is conserved by the opening displacement of other voids. From outside the composite, the powder appears to be completely constrained from densifying, but from within, some voids grow as others disappear. Thus, it had to be concluded that the mean hydrostatic tensile stress, produced within the powder matrix as it shrinks onto inclusions, plays little role in the densification behavior of composite systems.

It is now recognized that interaction between inclusions constrain composite densification. This interaction can be viewed in terms of an inclusion network. The inclusions in the network can be either touching or non-touching. At one extreme, all the inclusions touch one another, and the network itself cannot be densified as exemplified by the dense random packing of spherical inclusions or a strong network formed by touching whiskers or fibers. For this extreme case, it is easily seen that the relatively weak sintering 'stresses' produced by the powder cannot further consolidate the inclusion network, viz., the composite cannot change its volume as the powder attempts to densify. In the other extreme, none of the inclusions touch one another, but as it will be reviewed, the inclusions still form a strong interactive network that constrains composite densification.

Figure 1 illustrates a pair of spherical inclusions within a powder matrix.<sup>20</sup>

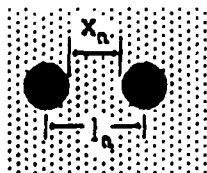


Figure 1 Two inclusions within a powder compact

Assuming that the powder everywhere exhibits the same linear shrinkage strain,  $\epsilon_m$ , the center to center shrinkage strain  $\epsilon_n$  for the inclusion pair is directly proportional to the linear shrinkage strain produced by the sintering matrix powder

between the inclusions and their separation distance to center-to-center distance ratio  $x_n/l_n$ .

$$\epsilon_n = \frac{x_n}{l_n} \epsilon_m \quad (1)$$

We can now describe the shrinkage of a composite powder containing a random distribution of non-touching, identical inclusions with an imaginary network formed by drawing lines between inclusion centers. The linear shrinkage of the network must mimic that of the composite, i.e.,  $\epsilon_{net} = \epsilon_{comp}$ . If it is assumed, for the moment, that the linear shrinkage between each inclusion pair is identical to that of the network,  $\epsilon_n = \epsilon_{net} = \epsilon_{comp}$ , rearrangement of Eq (1) shows that the matrix strain will depend on the inverse separation distance ( $x_n$ ) between inclusions:

$$\epsilon_m = \frac{l_n}{x_n} \epsilon_{comp} = \left( \frac{d}{x_n} + 1 \right) \epsilon_{comp} \quad (2)$$

where  $d$  is the inclusion diameter. With this assumption, Eq (2) shows that the linear shrinkage of the powder between the network pairs will depend on their separation distance. This equation suggests that the matrix powder between closely spaced inclusions will be denser and reach full density before the powder between widely spaced inclusions. That is, with the assumption that  $\epsilon_n = \epsilon_{comp}$ , it can be seen that the network of non-touching inclusions constrains the densification behavior of the powder matrix and produces a non-uniform density distribution during shrinkage.

The case where the inclusion pairs must mimic the composite ( $\epsilon_n = \epsilon_{comp}$ ) is when the inert inclusions are placed on lattice sites. In order to fit together with neighbors, each unit cell must retain its shape as the powder shrinks during densification as shown in Fig. 2. Since the relative amount of powder (i.e., ratio of distance between

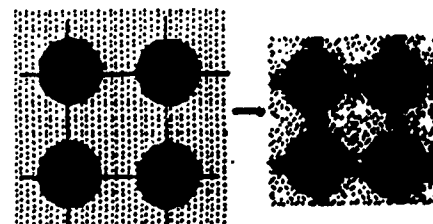


Figure 2 The development of a non-uniform distribution of matrix density due to a network on non-touching inclusions.

inclusions to distance between lattice sites) between cell edge sites is less than that between diagonal sites, identical network shrinkage Lange, et al.

strains will produce a different density for the powder between the different inclusions as concluded by Eq 2). That is, powder between site pairs forming cell edges will densify more relative to powder between diagonal site pairs. The condition that the unit cell must retain its shape requires that the shrinkage strain between any lattice site pair be identical to any other pair, viz.,  $\epsilon_n = \epsilon_{comp}$ . Thus the powder within the cell will have a lower density relative to the powder between edge site pairs. If the driving 'stress' of the lower density material within the cell is sufficient to compress and deform the denser material along connecting cell edges (i.e., pull the inclusions into the cell), then the matrix within the cell will fully densify without distorting the shape of the cell.

The assumption that  $\epsilon_n = \epsilon_{comp}$  states that the network formed by the inclusions shrinks without changing its shape, viz., the angles between network pairs do not change during composite densification. This is the condition required of the periodic network discussed above. In reality, some network distortion will occur. A random distribution of non-touching inclusions can be defined with different, irregular polyhedra joined together on faces. Inclusions are located at polyhedra vertices. Because each inclusion is shared by 4 different polyhedra, the shape change of any one polyhedron will require compatible shape changes by neighboring polyhedra. Since collectively, small groups of polyhedra must mimic the behavior of the composite, each polyhedron will impose some constrain on the deformability of its neighbors. The extreme case for this constrain is required by the periodic network<sup>20</sup> where  $\epsilon_n = \epsilon_{comp}$ .

As detailed elsewhere,<sup>21</sup> microstructure observations show that a network of denser material, surrounding lower density regions, does develop during constrained densification. This observation strongly suggests that  $\epsilon_n = \epsilon_{comp}$ . Two phenomena were observed as the composite was further heat treated to increase composite density. First, grain growth occurred within the dense network material due to grain boundary motion. Second, voids within the lower density regions grew larger by a desintering process (i.e., the separation of previously sintered grains) associated with grain coarsening. The larger voids are thermodynamically more stable to the low density microstructure from which they developed. These microstructure observations have led to a model of composite densification consistent with the constraining effect of the inclusion network: As the composite shrinks a network of denser material develops (expected to be associated with more closely spaced inclusions). The sintering 'stress' exerted by the lower density regions is small relative to the stress needed to deform the denser network. During this

shrinkage process, the denser network becomes more resistant to deformation through grain growth, and the lower density regions dissipate their shrinkage potential via desintering during coarsening.

Portions of this model do not apply to glass powders. Since glass powders do not develop grain boundaries during sintering they neither undergo microstructural instabilities (desintering) due to grain coarsening phenomena nor creep harden due to grain growth. In glass powder composites, the inclusion network will produce the same non-uniform density distribution discussed for crystalline powder matrices. But instead of dissipating their sintering stress via grain coarsening, the lower density regions in a glass matrix will continue to exert a sintering stress on the denser portions of the matrix and the inclusion network. If the sintering stress is sufficient to deform the inclusion network, denser regions within the matrix will deform via viscous flow to allow network deformation and composite densification. Thus, this model not only explains the effect of a network of inert inclusion on the densification of a crystalline powder, but also explains why the densification of glass powders is less affected by inclusions.

It can thus be concluded that both touching and non-touching inclusion networks will constrain the densification of a crystalline powder matrix. Either network will produce a non-uniform density distribution within a powder matrix that attempts to shrink via sintering. The understanding gained by the microstructural observation that confirm this simple model have led to new thinking, currently under study, to determine how to avoid the redistribution of the void phase due to constrained densification while optimizing the strength of the matrix phase produced by sintering.

## INNOVATIVE PROCESSING

By asking the silly question, "Can reinforcements be added to a fully dense ceramic matrix?", two new composite processing methods have been developed. Each completely avoids the problem of differential densification discussed above. One of these methods produces a metal reinforced ceramic composite while the other, produces a laminated ceramic composite. Their processing and preliminary properties will be outlined.

**METAL REINFORCED CERAMICS** - Jamet et al.<sup>22</sup> were the first to show that a powder could be packed within a fiber preform using a process similar to pressure filtration. In an adaptation used here, a fiber preform is placed on top of the filter and particles within the slurry flow through the

preform channels to build a consolidated layer within the preform during pressure filtration as schematically shown in Fig. 3. Before a consolidated layer builds up on the filter, a uniform pressure exists within the slurry and within the liquid filled (or slurry filled) preform. As the consolidated layer builds within the preform, the combined pressure exerted by the consolidated layer and the liquid is identical to the pressure within the slurry. That is, throughout all stages of pressure filtration, the preform is never subjected to non-hydrostatic loads which would produce disruptive effects (i.e., preform compaction and/or crushing). Thus, the preform is only subjected to a hydrostatic pressure. As discussed below, the strain stored within the preform, due to the hydrostatic pressure, can produce detrimental effects.

Our experience has shown that the success of this processing method depends on three conditions. First, it is obvious that if the consolidated layer is to form within the preform during filtration, particles must be small enough to flow through the preform channels. Filtration literature suggests that the particles should at least be 7-10 times smaller than the percolation channels to prevent the preform from acting as a filter. As discussed above, because of particle packing requirements, the ratio of the particle to reinforcement diameter needs to be  $\leq 0.02$ . When this requirement is converted to channel size, the particle diameter should be at least 10<sup>3</sup> times smaller than the average channel diameter. Second, the particles cannot be strongly attracted to themselves (should not floc) or attracted to the preform material as they flow through the channels. When attractive surface forces prevail, the channels are quickly blocked, the preform itself acts as the filter, and a consolidate layer builds up on top instead of within the preform. The third condition, discussed below, concerns the differential strain released from the network relative to the consolidated powder matrix.

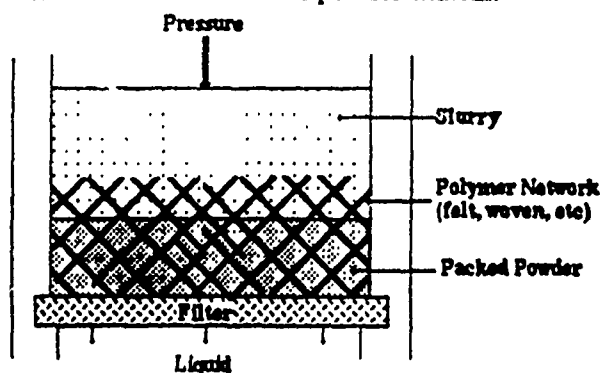


Figure 3 Packing of a powder into a pyrolyzable (carbon, polymer, etc) preform can be accomplished by pressure filtration. This is the first step in producing continuous pore channels that will be later filled with a molten metal after the ceramic powder matrix is densified.

The new method to produce metal reinforced ceramics involves four steps: 1) forming a powder compact containing a continuous network of either organic or carbon material by pressure filtration, 2) pyrolyzing the network to form channels within the powder compact that mimic the preform, 3) densifying the powder while retaining the channel network, and 4) intruding metal into the channel network by, e.g., squeeze casting. Pressure filtration is used to form the powder compact containing the pyrolyzable network either by pressure filtering mixed powder, chopped fiber slurries or by packing powder within pyrolyzable preforms as shown in Fig. 3. After the liquid is removed from the pressure filtered composite system and the preform is pyrolyzed, the furnace temperature is raised to densify the matrix powder. The decrease of the void volume associated with the channel network, remnant of the pyrolyzed preform, is proportional to the densification of the powder matrix, viz., the decreased channel diameter is proportional to the linear shrinkage strain of the powder matrix. Since the relative volume change of the void volume associated with the channel network is identical to the relative volume change of the powder matrix  $[(\Delta V/V)_{\text{network}} = (\Delta V/V)_{\text{matrix}}]$ , the volume fraction of the void volume associated with the channel network (and thus, the metal reinforcement) after densification is identical to the volume fraction of the preform material before densification. Metal reinforced ceramic composites with different reinforcement architectures, volume fractions and fiber diameters can be produced with this method.

Two different composite systems, one with a  $\text{Al}_2\text{O}_3$  matrix and the other with a transformation toughened  $\text{ZrO}_2$  (+3 mol %  $\text{Y}_2\text{O}_3$ ) matrix, have been fabricated using either polymer or carbon felts as the pyrolyzable preform material. The pore channels in both were intruded with a molten Al-Mg alloy. The effect of the metal reinforcement on crack growth resistance is currently under study in both systems.

Processing problems have been encountered in both systems. Microstructure examination has revealed that cracks exist within the ceramic matrix filled with metal during squeeze casting. In some composites, the cracks are infrequent and small, only extending a few fiber diameters, whereas in other composites, the cracks are numerous and large. Current evidence strongly suggests that these cracks are produced prior to the pyrolysis of the preform and are caused by either differential strain recovery after pressure filtration or powder matrix shrinkage when the liquid is removed by evaporation. Both of these problems will be discussed as related to the rheology of the pressure filtered body and interparticle forces.

To understand the problem of differential strain recovery, we must first understand the stress-strain behavior of consolidated powder bodies.

Consolidated powders exhibit non-linear elastic stress-strain behavior similar to that described by Hertz<sup>24</sup> for two spheres pressed together. The compressive stress ( $\sigma$ )-strain ( $\epsilon$ ) response of a powder can be expressed<sup>25</sup> as  $\sigma = A\epsilon^{3/2}$ , where  $A$  depends on the relative density of the powder compact (average number of contacts per particle) and the elastic properties of the particles. Relatively small stresses produce large strains and the compact becomes stiffer as the stress is increased. It is not the porosity that produces this behavior, but the large displacements between particle centers when a 'point' contact is elastically compressed into an area contact. Thus, after a powder has been consolidated and the pressure released, large elastic strains are recovered and the compact grows. The linear strain recovery of an  $\text{Al}_2\text{O}_3$  powder compact, produced by pressure filtration with an applied pressure of 80 MPa, is  $\approx 2$  to 3 %.<sup>26</sup>

Experiments have shown<sup>26</sup> that the strain recovery phenomena in powder compacts saturated with a liquid, i.e., those produced by pressure filtration or centrifugation, are time dependent. In addition, the rate of strain release depends on the rheology of the consolidated body, which in turn depends on the interparticle forces. Some bodies consolidated from dispersed slurries (repulsive interparticle forces) still flow despite their very high particle packing density, i.e., despite being pressed together during filtration, the particles are still repulsive when pressure is released. Their rheology can be described as plastic and they release their stored strain within a relatively short period. Bodies consolidated from flocced slurries (strongly attractive interparticle forces) appear elastic and they continue to release strain for many hours. In these bodies, as the particle network attempts to relax its stored compressional strain, the surrounding liquid is placed in tension. Liquid (or air) must flow from the surface to the interior to dissipate the tension within the liquid and thus, the compressional strain within the network. The time required to dissipate these stresses by fluid flow is governed by Darcy's Law. Dispersed bodies, on the other hand, appear to dissipate their stored strain by body flow. As addressed below, strain relaxation is of critical importance in the structural integrity of bodies containing either reinforcements or pyrolyzable networks.

The structural integrity of the dense ceramics (prior to metal intrusion) containing the channels remnant of the pyrolyzable preform was observed to depend on whether it was produced from a flocced or a dispersed slurry.<sup>23</sup> In repeated experiments, flocced slurries produced weak matrices whereas, dispersed slurries produced relatively strong matrices. Examination of

fracture surfaces of bodies produced from flocced slurries revealed large cracks produced during strain recovery. It was shown that the large cracks observed in the relatively elastic bodies produced from flocced slurries was caused by the differential recovery strain of the polymer preform relative to the consolidated powder when pressure was released after filtration. Since both the saturated powder matrix and the embedded preform material are both under compression, both will recover strain and grow larger as the pressure is released. By comparing the different stress-strain behavior of the powder matrix and the polymer preform, it was shown that the polymer preform would release more strain than the powder matrix. For the case of the relative elastic body formed from the flocced slurry, the differential strain recovery produced tensile stresses within the powder compact which were relieved by cracking. This problem did not arise when the body was consolidated from the dispersed slurry because the body was plastic and dissipated the stresses produced by differential strain recovery via body flow.

This initial work<sup>23</sup> concluded that cracking problems encountered by differential strain recovery could be avoided by using dispersed slurries because they produced plastic bodies. Current work shows that dispersed slurries can also produce relatively elastic bodies that are prone to cracking during differential strain recovery. We now recognize that repulsive particles in a slurry can be made attractive by the pressure exerted on the particle network during pressure filtration. Although a discussion of this effect is beyond the present review, our research is directed to understand and avoid this problem.

After a composite body is removed from the pressure filtration device, it is saturated with a liquid. This liquid must be removed prior to heat treatment. When the liquid is removed by evaporation, capillary forces exert a pressure on the particle network which can cause the particles to rearrange and increase their packing density, viz., shrinkage can occur during liquid removal via evaporation. Since composite bodies used to produce a metal reinforced system contain a pyrolyzable preform that may not shrink during liquid removal, stresses and disruptive phenomena can develop as the powder matrix shrinks during drying.

Current evidence suggests that the amount of shrinkage will depend on both the interparticle force and the pressure used to consolidate the powder. When a body is formed from flocced slurries, the particle packing density is strongly dependent on the consolidation pressure. If the consolidation pressure is less than the capillary pressure ( $\approx 0.5$  to 1 MPa) produced during drying, the body shrinks to the relative density produced by the capillary pressure.<sup>26</sup> This shrinkage can be

considerable. When the flocced slurry is consolidated at pressures much greater than the capillary pressure, the body exhibits very little shrinkage (linear strains  $< 0.5\%$  during drying because the smaller capillary pressure can not further rearrange the particle network.<sup>26</sup> When bodies are produced from dispersed slurries, their packing density is independent of the applied pressure, and can be much greater than that achieved with flocced slurries.<sup>26</sup> If the particles are still repelling one another in these bodies, they are not touching one another, and despite their much higher packing density, the body shrinks during drying as liquid is removed from between the non-touching particles. Namely, their shrinkage is related to the separation distance between the non-touching particles. The linear shrinkage strains for these dispersed bodies are typically  $\sim 1.5\%$ . Coagulated slurries (weakly attractive forces at long range, but strongly repulsive at short,  $< 2\text{nm}$ , range) produce the same particle packing densities as highly dispersed slurries. Recent work shows that their packing density is also pressure insensitive. Bodies produced from coagulated slurries also produce a non-touching particle network, but the particles are more closely spaced relative to highly repulsive particles. Preliminary observations suggest that they shrink less ( $< 1\%$ ) than bodies produced with dispersed slurries.

Regardless of the phenomena causing variable and currently, uncontrollable matrix cracking, composite materials have been produced to measure crack growth resistance behavior. Progress concerning the composite system formed with the  $\text{Al}_2\text{O}_3$  matrix, reinforced with the Al-Mg alloy has produced interesting observations. Initially, experiments concentrated on determining R-curve behavior where stable cracks were propagated through bar specimens placed in bending. Although these experiments showed that the metal reinforced composite did exhibit crack growth resistance behavior, it was determined that the data was not intrinsic to the material due to large scale bridging effects.<sup>27</sup> That is, the bridged crack length to specimen width ratio was too large to determine intrinsic crack growth resistance behavior without certain assumptions. As detailed elsewhere in this proceedings,<sup>28</sup> the plateau value of  $G_c$  was determined by a work-of-fracture measurement where stable cracks were propagated through a chevron-shaped web of material machined in bar specimens placed in bending. Three different materials have been examined in detail: 1) polycrystalline  $\text{Al}_2\text{O}_3$  without the Al-Mg reinforcements, 2) polycrystalline  $\text{Al}_2\text{O}_3$  containing 23 vol % Al-Mg reinforcement ( $\sim 17\text{ }\mu\text{m}$  diameter) produced with a polymer felt preform with smooth fiber surfaces, and 3) polycrystalline  $\text{Al}_2\text{O}_3$  containing 17 vol % Al-Mg reinforcement ( $\sim 10\text{ }\mu\text{m}$  diameter) produced with a carbon felt pre-

form with serrated fiber surfaces. The average value of  $G_c$  for the  $\text{Al}_2\text{O}_3$  without the reinforcements was  $40\text{ J/m}^2$ , whereas that for the  $\text{Al}_2\text{O}_3$  containing the 23 vol % of  $17\text{ }\mu\text{m}$  diameter metal reinforcements was  $400\text{ J/m}^2$ . As discussed elsewhere in this proceedings,<sup>28</sup> it currently appears that the debonding characteristics of the metal/ceramic interface, produced by metal cavitation associated with matrix grain junctions at this interface, is the feature that controls the deformability of the metal reinforcement, its bridging length prior to failure and thus, the fracture resistance of the composite system.

**LAMINAR COMPOSITES** - In the second new approach to fabricate ceramic composite by making the ceramic dense and then adding the reinforcements, dense ceramic sheets, produced by the conventional tape casting method use to manufacture ceramic substrates for the electronic industry, are sandwiched and bonded to fiber layers as schematically shown in Fig. 4.

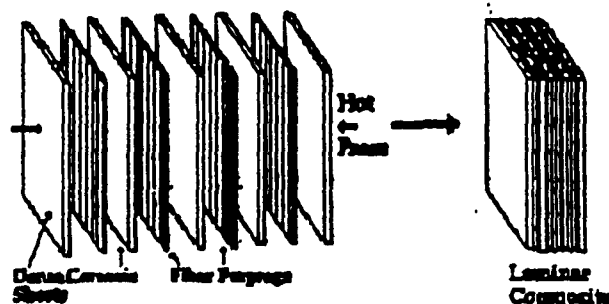


Figure 4 Processing method for producing laminar ceramic composites using dense ceramic sheets processed by tape casting and fiber layers pre-impregnated with an agent that both controls the interfacial bond between the fiber and bonding agent and bonds the prepreg to the ceramic.

As imagined, the ceramic can have any desired composition, e.g., it can be a composite itself. The fiber architecture can be unidirectional, cross-plyed, or woven. The bonding agent impregnates the fibers and bonds the fiber layer to the ceramic sheets; it must also produce an interface with the fibers to impart the desired interfacial fracture behavior. The bonding agent can be an epoxy, metal, glass or ceramic. The fiber layer is impregnated with the bonding agent (e.g., as a liquid or powder slurry) prior to composite processing.

To initiate an investigation of the mechanical behavior of this type of composite system, a low temperature composite has been fabricated with commercial ceramic sheets laminated with epoxy-carbon fiber prepreps. Processing of these composites is very simple and allows the production of a large quantity of



specimens with different ceramic materials and fiber architectures. The uncured epoxy preregs, received frozen from the manufacturer, are thawed, cut to the appropriate size, laminated with the ceramic sheets, vacuum bagged (to minimize entrapped air) and hot-pressed at 135 °C to cure the epoxy. Glass,  $\text{Al}_2\text{O}_3$ , and different transformation toughened  $\text{ZrO}_2$  sheets have been used to fabricate different composites to determine the effect of substrate properties (elastic modulus, fracture toughness, and strength) on the mechanical properties of the composite. Using these different ceramic sheets, different composites have been processed with unidirectional, 0-90 cross-ply (either within one layer or separated by a ceramic sheet), and woven (cloth) fiber architectures. The volume fraction of the fibers was varied by either using more than one fiber prepreg between each pair of ceramic sheets or using ceramic sheets of different thicknesses.

The ambitious investigation of the mechanical behavior of these composites includes: flexural testing, tensile testing, torsion testing, crack growth resistance determinations, and interfacial  $G_c$  determinations under mixed mode loading. Variables that include ceramic material properties (glass,  $\text{Al}_2\text{O}_3$ , tt- $\text{ZrO}_2$ ), fiber architecture, fiber volume fraction, fiber orientation, and temperature (to change the properties of the epoxy bonding agent) are under investigation. The program also includes the development and modification of testing procedures, e.g., the development of a tensile test to both prevent the longitudinal failure of unidirectional composite placed in transverse tension and minimize bending moments. Current results are limited to preliminary observations of the different  $\text{Al}_2\text{O}_3$ -epoxy/carbon fiber composites.

Although tensile testing procedures are still under development, preliminary tensile results strongly suggest that the stress-strain and failure behavior of unidirectional, laminar composite (7 vol % fibers) are similar to continuous matrix, continuous brittle fiber ceramic composites.<sup>29</sup> Namely, during initial loading the composite exhibits a linear stress-strain behavior. As the tensile load is increased, a crack extends through one of the ceramic sheets. Because tensile testing still includes large bending stresses, the stress level for this initial crack extension has not been correlated to the tensile strength of the ceramic itself. Four-point flexural testing suggest that it is within the range of the ceramic's strength; effects of residual thermal stresses developed during processing are unknown. Unlike uniaxial composites with a continuous ceramic matrix, the crack in one ceramic sheet is generally not coplanar with those that appear within other ceramic sheets at higher stresses. More cracks appear within each ceramic sheet with increasing load. The nature of the crack spacing and crack

density vs increasing load appears to be similar to that observed for uniaxial ceramic composites with a continuous matrix composite.<sup>29</sup> The stress-strain behavior of the laminar composite deviates from its initial linear behavior as cracks appear in the ceramic sheets. The stress-strain response of the laminar composite within the regime of increasing crack density has yet to be characterized, but the portions of the ceramic sheets between the cracks still support a portion of the applied load and contribute to the composite's stress-strain behavior until only fibers hold the composite together. Catastrophic failure occurs at the failure strain of the fibers ( $\approx 1.5\%$  for the current fibers).

Tensile and flexural tests of unidirectional laminar composites both show that brittle, low strain to failure behavior occurs when the tensile stress is applied perpendicular to the fiber direction, whereas, the high strain to failure behavior described above, occurs when the tensile stress is applied parallel to the fiber direction. In addition, for the composites tested to date (7 vol % fibers) the composite supports a significantly larger tensile stress when the tensile direction is parallel to the fiber direction.

The determination of the crack growth resistance behavior of these laminar ceramic composites initiated with unidirectional composites (7 vol % fibers) machined to a modified ASTM compact tension configuration. It quickly became apparent that regardless of the fiber to crack orientation, cracks only extended parallel to the fiber direction. This material was used to show that when the fibers are parallel to the extending crack, failure was catastrophic and the  $K_{Ic}$  was typical of  $\text{Al}_2\text{O}_3$ , viz.,  $K_{Ic} = 4.0 \text{ MPa}\sqrt{\text{m}}$ .<sup>1/2</sup> New specimens, with each fiber layer containing a 0-90 cross-ply, were prepared (14 vol % fibers) to allow testing with crack extending perpendicular to the fiber direction. Although this testing configuration is no longer used to explore crack growth resistance behavior for these composites due to large scale bridging effects,<sup>27</sup> (despite the relative large specimen size, approx:  $0.6 \times 4 \times 4 \text{ cm}$ , no apparent fiber failure occurred as the cracks within the ceramic sheets approached their maximum length), the observations made during this testing are instructive. First, the  $K_{Ic}$  of the initial crack extension from the machined notch was nearly identical to that for tests where cracks were extended parallel to the fibers in unidirectional composites. Second, after an initial pop-in, crack extension required an increasing applied stress intensity factor. Third, after initial crack pop-in and some extension, large secondary cracks were observed to extend either from the machined notch or from a position along the initial crack surface. And fourth, as shown in Fig. 5, cracks were inhibited from propagating completely through the ceramic sheets by the



apparent compressive stress in the unfractured ligament. As shown in Fig. 5, the cracks actually curve around to propagate in the opposite direction. New testing configurations are now being sought to determine the intrinsic crack growth resistance behavior of these materials without resorting to extremely large specimens.

In conclusion, the preliminary results presented here and more systematic studies currently underway, strongly suggest that ceramic composites, processed by laminating and bonding dense ceramic sheets with fiber layers, have the potential to support higher tensile stresses, catastrophically fail at significantly higher strains and possess useful crack growth resistance behavior relative to their matrix material. This conclusion not only supports our need to better understand the failure phenomena of the current laminar composite systems, but also to extend our processing to laminar composite systems with high temperature capability.

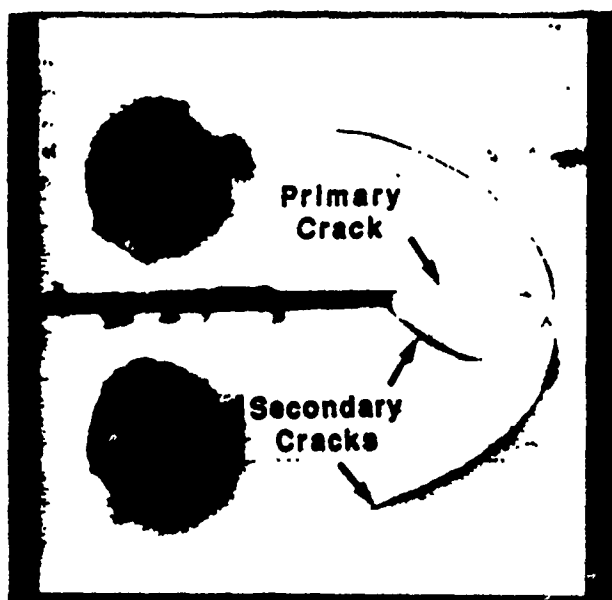


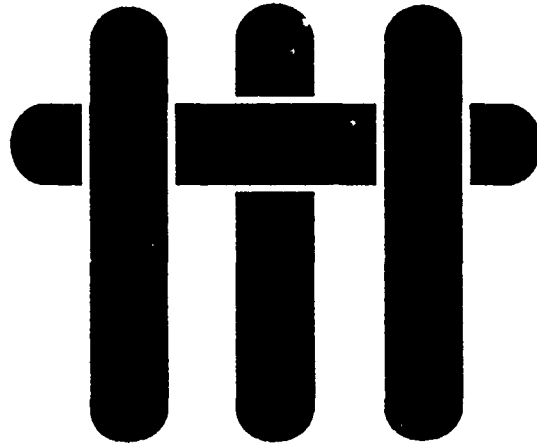
Figure 5 Modified compact tension specimen of laminar ceramic composite made from  $Al_2O_3$  ceramic sheets bonded to epoxy-carbon prepreps. Cracks produced during testing were highlighted with red dye penetrant.

**ACKNOWLEDGEMENTS** - This work was supported, in part, by a DARPA/ONR contract, No. N00014-86-K-0753, (Composite Processing) which is part of a larger multi-investigator, multi-institutional research program concerned with high temperature structural materials lead by A. G. Evans and R. Mehrabian. Research concerning the colloidal processing of powders is supported by an ONR contract, No. N00014-90-J-1441.

1. J.-F. Jamet, L. Anquez, M. Parlier, M.-H. Ritti, P. Peres, and L. Grateau, *L'Aéronautique et l'Astronautique*, No. 123/124, 128-42 (1987).

2. R. Naslain, *J. de Phys. Colloque C1*, sup. au no. 2, vol. 47, C1-703-715 (1986).
3. A. J. Pyzik, A. A. Aksay and M. Sarikaya, *Ceramics Microstructures '86*, Role of Interfaces, pp 45-54, Ed. by J. A. Pask and A. G. Evans, Plenum Press, N.Y. (1987).
4. M. S. Newkirk, A. W. Urquhart, H. R. Zwickler, and E. Breval, *J. Mater. Res.* 1 [1] 81-9 (1986).
5. F. F. Lange and D. C. C. Lam and O. Sudre, *Mat. Res. Soc. Symp. Proc* 155 [4] 309-18 (1989).
6. D. C. C. Lam and F. F. Lange to be published
7. B. V. Velamakanni, and F. F. Lange, submitted to *J. Am. Ceram. Soc.*
8. D. C. C. Lam, F.F. Lange and F. Zok to be published
9. F. F. Lange, *J. Am. Ceram. Soc.* 72 [1] 3-15 (1989).
10. B. V. Velamakanni, J. C. Chang, F. F. Lange and D. S. Pearson, *Langmuir Letters*, in press.
11. L. C. De Jonghe, M. N. Rahaman and C. H. Hsueh, *Acta Metall.* 34 [7] 1467-71 (1986).
12. R. K. Bordia and R. Raj, *J. Am. Ceram. Soc.* 71 [4] 302-10 (1988).
13. R. J. Brook, W. H. Tuan, and L. A. Xue, *Ceram. Trans.*, V 1, *Ceramic Powder Science*, Ed. by G. L. Messing, E. R. Fuller, and H. Hausner, 811-21, Am. Ceram. Soc. (1988).
14. G. Y. Onoda and G. L. Messing, *Processing of Crystalline Ceramics*, *Materials Science Research Vol 11*, ed by H. Palmour III, R. F. Davis and T. M. Hare, pp 99-112, Plenum Press, 1978.
15. C.-H. Hsueh, A. G. Evans, and R. M. McMeeking, *J. Am Ceram. Soc.* 69 [4] C64-6 (1986).
16. R. Raj and R. K. Bordia, *Acta Met.* 32 [7] 1003-20 (1984).
17. G. W. Scherer, *J. Am. Ceram. Soc.*, 70 [10] 719-25 (1987).
18. F. F. Lange, *Acta Met.* 37 [2] 697-704 (1989).
19. J. R. Porter and F. F. Lange, unpublished work.
20. F. F. Lange, *J. Mater. Res.* 2 [1] 59-65, 1987.
21. O. Sudre, D. C. C. Lam and F. F. Lange, *Mat. Res. Soc. Symp. Proc* 155 [4] (1989).
22. J. Jamet, D. Daraeange and J. Loubeau, French Patent No. 2,526,785, Nov. 18, 1983.
23. F. F. Lange, B. V. Velamakanni and A. G. Evans, "Method for Processing Metal-Reinforced Ceramic Composites," *J. Am. Ceram. Soc.* 73 [2] 388-93 (1990).
24. S. Timoshenko and J. N. Goodier, *Theory of Elasticity*, McGraw-Hill Book Co. (1951).
25. K. Walton, *J. Mech. Phys. Solids*, 35 [2] 213-226 (1987).
26. F. F. Lange and K. T. Miller, *Bul. Am. Ceram. Soc.* 66 [10], 1498-1504 (1987).
27. F. W. Zok and C. L. Hom, *Acta Met.*, in press.
28. B. D. Flinn, F. W. Zok, F. F. Lange and A. G. Evans, this proceedings.
29. D. B. Marshall and A. G. Evans, *J. Am. Ceram. Soc.* 68 [5] 225-31 (1985).

# M A T E R I A L S



## **EFFECTS OF PLASTICITY ON THE CRACK PROPAGATION RESISTANCE OF A METAL/CERAMIC INTERFACE**

by

I. E. Reimanis, B. J. Dalgleish, M. Brahy, M. Rühle and A. G. Evans

Materials Department  
College of Engineering  
University of California  
Santa Barbara, California 93106

## ABSTRACT

Fracture experiments have been conducted on a gold/sapphire interface. The interface is found to fail by interface separation in a nominally "brittle" manner with a critical strain energy release rate,  $G_c \approx 50 \text{ Jm}^{-2}$ , substantially larger than the work of adhesion,  $W_{ad} \approx 0.5 \text{ Jm}^{-2}$ . Evidence of plastic deformation on the gold fracture surface, such as blunting steps and slip steps, suggest that plastic dissipation is the primary contribution to the measured  $G_c$ . Calculations suggest that the majority effect occurs in the plastic zone through the crack wake. The interface is also found to be susceptible to slow crack growth.

## 1. INTRODUCTION

Metal/ceramic interfaces exhibit a wide range of fracture energies, dependent on bonding, interface morphology, plasticity in the metal and on the presence of interphases.<sup>1,2,3</sup> Detailed understanding of the fracture energy requires a systematic experimental study in conjunction with calculations of crack tip fields, using continuum<sup>4,5</sup> as well as dislocation level calculations. One aspect of this problem is addressed in this article; notably an experimental study of the effect of plasticity. To investigate this issue, the sapphire/gold system has several attributes. In particular, test specimens can be produced by diffusion bonding without the formation of interphases. Furthermore, bonding occurs without dissolution of  $\text{Al}_2\text{O}_3$  in the Au and consequently, the flow stress of the Au is well-behaved. Finally, the transparency of the sapphire allows *in-situ* observation of crack propagation along the interface, as needed to elucidate the dominant fracture mechanism.

The fracture energy of bimaterial interfaces can be measured with good precision by using a mixed mode four-point bending specimen<sup>6</sup>. This specimen has the dual advantage that precracking can be conducted with good control and that, when the interface crack is between the inner loading points, the energy release rate is essentially crack length independent<sup>6</sup>. In addition, the crack orientation in this specimen facilitates the *in-situ* observations of crack growth.

## 2. DIFFUSION BONDING

Diffusion bonded plates are produced by carefully polishing basal plane oriented sapphire discs having two-inch diameter. Polishing is conducted mechanically using diamond media. Gold foil, cold rolled to thicknesses in the range 10 to 250  $\mu\text{m}$ , is inserted between the sapphire plates and the system subjected

to a normal stress of about 5 MPa, within a resistance furnace. The temperature is raised to 1040°C either in air or in vacuum and maintained at that temperature for 1 to 48 h. The system is then slowly cooled to room temperature. Inspection of the interfaces in the optical microscope reveals the progression of the bonding process (Fig. 1a) from large planar voids to small, isolated, faceted voids in the Au. Such behavior is typical of void elimination processes at interfaces involving diffusion. Furthermore, the process was essentially the same for bonding conducted in air and in vacuum. After 48 h, some small isolated voids remain, corresponding to an area fraction of interface of ~ 10 percent. The same voids can also be identified on fracture surfaces (Fig. 1b). The pores are typically about 1  $\mu$ m deep and 3–10  $\mu$ m wide.

### 3. EXPERIMENTAL PROCEDURES

Beams with overall dimensions 40 x 3 x 3 mm are cut from the diffusion bonded plates and polished to facilitate optical observation during testing. Experience has indicated that testing is expedited by having a sapphire layer on the tensile side with thickness of ~ 0.5 mm while the sapphire on the compression side has a thickness of ~ 2.5 mm. Subsequent to cutting and polishing, a Knoop indentation, loaded to ~ 100N, is emplaced in the thinner sapphire layer, with axis normal to the beam axis, as needed to initiate a surface crack. Thereafter, the specimens are precracked by loading in three-point bending, using an outer span of 33 mm. During this process, the surface crack extends through the sapphire layer to the sapphire/gold interface and also extends symmetrically along the interface on both sides of the precrack to a length of ~ 0.5 mm (Fig. 2).

Subsequent to precracking, the specimen is loaded in a four-point bending fixture (inner and outer spans of 33 mm and 19 mm, respectively) located in an optical microscope (Fig. 3), as needed to permit *in situ* observation of cracking. Surfaces of the specimens and of the loading rods were carefully polished to negate effects of friction. Loading is continued as crack propagation proceeds and load, crack length data are generated. In some cases, intermittent unloading is conducted in conjunction with optical observation of the interface.

Following mechanical testing, the fracture surfaces are investigated in the scanning electron microscope (SEM), with the objective of both characterizing morphological features of the fracture process and investigating possible chemical differences using energy dispersive X-ray procedures (EDS). In addition, channeling patterns are obtained and used to characterize crystallographic orientations. Finally, transmission electron microscopy (TEM) of cross sections is used to provide further information about the chemical and atomistic characteristics of the interface.

#### 4. MEASUREMENTS AND OBSERVATIONS

Preliminary observations of crack growth reveal that subcritical crack extension occurs. However, crack extension is intermittent and erratic, as illustrated by the crack front sequences depicted in Fig. 4a. Nevertheless, the crack extends at an essentially uniform mean velocity when a constant load is applied and furthermore, the mean velocity increases when the load is increased. The subcritical growth behavior is seemingly characterized by a relationship between the crack velocity  $\dot{a}$  and the energy release rate  $G$ . The corresponding value of the phase angle of loading<sup>6</sup>  $\psi$  is  $52^\circ$ . The range in velocity at fixed  $G$  reflects the intermittent nature of

crack growth which, in turn, may depend on the spatial non-uniformity of the "bonding."

The magnitude of the critical energy release rate  $G_c$  can be estimated from the precracking experiments. During precracking, the load is increased until the Knoop indentation crack in the sapphire is induced to extend unstably across the specimen. This event coincides with a load drop (Fig. 5), to a load  $P_a$ , at which the crack bifurcates along the interface, arrests and then slowly extends (Fig. 2). Interface crack extension during this sequence occurs quite rapidly and consequently, the magnitude of  $G$  deduced from  $P_a$  is regarded as an approximate measure of  $G_c$ . Estimates of  $G_c$  can be obtained from solutions generated by Charalambides et al.<sup>6</sup> extrapolated into the short crack range. This procedure indicates that  $G_c$  is about  $50 \text{ Jm}^{-2}$ .

Upon constant-load crack growth a:  $G < G_c$ , the fracture surface is found to be relatively featureless at optical resolutions (Fig. 6). However, a change in load generates a step in the gold along the crack front (Fig. 6). The steps are indicative of crack blunting, as elaborated below. Slip steps that emanate from the crack front are also evident in some cases. During unloading, crack closure occurs over dimensions of order  $100 \mu\text{m}$  (Fig. 7). However, the original crack front is still visible as a small trough, again indicative of a blunt crack.

## 5. CHARACTERIZATION

### 5.1. SCANNING ELECTRON MICROSCOPY

The fracture surfaces have been examined by scanning electron microscopy. Within the resolution limits of EDAX, there is no evidence of Au on the sapphire fracture surface and no evidence of Al on the Au. Channeling patterns obtained on

the Au surface (Fig. 8a) reveal that the Au has recrystallized during diffusion bonding into a highly textured foil with a {100} interface plane. The grain size is approximately 100–200  $\mu\text{m}$  (Fig. 8b). Furthermore, patterns obtained on both sides of slip steps reveal small lattice rotations of up to  $5^\circ$ . The oriented nature of the Au allows determination of the facet and slip step directions from the channelling patterns. In all cases, the facets and slip steps are along  $\langle 110 \rangle$ , consistent with slip in the Au occurring on {111}.

Observations of the sapphire surface reveal that it is featureless and essentially the same as the original surface prepared prior to bonding. It is thus concluded that there have been minimal morphological changes in the sapphire during bonding and mechanical testing, consistent both with the low diffusivities in the sapphire at the bonding temperature and with its high resistance to slip at room temperature.

The topography of the Au fracture surface has been examined using two techniques. In one case, a profilometer was scanned over the surface, to create a narrow plastic trough of uniform width. The profilometer readings gave one measure of the topography (Fig. 9). Secondly, lines of electron beam damage have been created while the fracture surface was oriented normal to the incident beam. This was achieved by imposing a high voltage, in line profile mode, while the beam scanned the specimen in one direction.<sup>7</sup> The specimens were then tilted by 60 to  $80^\circ$  to allow the shapes of the features to be deduced from the line profiles<sup>7</sup> (Fig. 10).

These techniques indicated that the crack front *blunting* steps were typically  $< 0.1 \mu\text{m}$  in height and that all such steps had the same sign (Fig. 9). Investigation of the residual voids (Fig. 10) was of primary interest for estimation of the work of adhesion  $W_{\text{ad}}$  from the void surface inclination at the interface. These measurements gave,  $W_{\text{ad}} \approx 0.5 \text{ Jm}^{-2}$ , consistent with previous estimates.<sup>5</sup>



## 5.2 TRANSMISSION ELECTRON MICROSCOPY

Thin foils normal to the interface have been made by mechanical dimpling followed by ion beam milling. Preliminary TEM analysis indicates the following characteristics. An atomic resolution image (Fig. 11a) shows that the Au/sapphire interface is incoherent and that there is no intervening phase. Analytical TEM indicates that there is no Al in the Au and no Au in the  $\text{Al}_2\text{O}_3$  at the detectability limits of the EDS system (about 1at%). Furthermore, no other elements were noted in the EDS spectrum. In some places, the interface is non-planar (Fig. 11b), reflecting roughness associated with the original sapphire surface before bonding.

## 6. THE FRACTURE ENERGY

The seeming absence of gold on the sapphire fracture surface and of sapphire on the gold, coupled with the relatively low values of  $G_c$  compared with the fracture energy expected for a soft ductile metal ( $G_c > 10^4 \text{ Jm}^{-2}$ ), suggests that the crack progresses by brittle bond rupture at the interface. In support of this contention, it is noted that ductile interface fracture occurs by hole growth in the metal, leaving metal ligaments attached to the ceramic side of the fracture surface<sup>8</sup> (Fig. 12). The proposed "brittle" mode of failure at the  $\text{Al}_2\text{O}_3/\text{Au}$  interface occurs despite the incidence of plastic flow in the Au and of crack blunting.

The plastic dissipation associated with a crack growing along an interface can be addressed by invoking comparison with the behavior of cracks in isotropic elastic/plastic solids. For such materials, the energy release rate at the tip of a growing crack is strictly zero, such that the measured energy release rate equates entirely with the plastic dissipation.<sup>9</sup> Consequently, within the framework of continuum analysis, it has not been possible to relate the dissipation within the

plastic zone to the dissipation within the fracture process zone. Yet, for the present problem, it is important to develop a basic expression that allows the plastic dissipation to be related to such variables as the metal layer thickness, the work of adhesion, etc. A preliminary attempt, described in the Appendix, considers the admissible dissipation outside the blunting width,  $\delta$ , and yields a dissipation,

$$W_p^* \approx G_o(h/\delta) \quad (1)$$

where  $h$  is the metal layer thickness and  $G_o$  is the dissipation within the fracture process zone. If  $G_o$  is regarded as being  $W_{ad}$ , then for the present case ( $h = 25 \mu\text{m}$ ,  $\delta \approx 0.1 \mu\text{m}$ ),  $W_p \approx 100 \text{ Jm}^{-2}$ . This level of dissipation is of the same order as the measured value ( $G_c \approx 50 \text{ Jm}^{-2}$ ). Qualitatively, therefore, the measured fracture energy is consistent with a dominant contribution from plastic dissipation.

The presence of slow crack growth indicates that rupture is chemically assisted and occurs in accordance with stress corrosion concepts.<sup>10</sup> These concepts typically invoke a brittle fracture process zone at the crack tip and a maximum stress-based fracture criterion in this zone.<sup>10</sup> However, for a thin metal layer between two elastic plates, the maximum normal stress of the interface exists at an appreciable distance ahead of the crack, governed by the layer thickness.<sup>11</sup> An interface decohesion criterion based strictly on the normal stress would thus predict a fracture mechanism that operates ahead of the crack front: at variance with present observations. Consequently, this topic also requires additional investigation.

## 7. CONCLUDING REMARKS

The relatively large fracture energy measured for the gold/sapphire interface reflects an influence of plasticity. Yet, the fracture process itself is brittle and seemingly occurs by "brittle" bond rupture. For such a process, it is qualitatively appreciated that the fracture energy should be a multiple of the work of adhesion,  $W_{ad}$ , and the metal layer thickness,  $h$ . Consequently, variations in fracture energy with metal layer thicknesses should provide further insight into the appropriate relations. However, ultimately, it will be necessary to couple the continuum level analysis of fracture to the atomistic bond rupture criterion through the use of discrete dislocation configurations.

The incidence of stress corrosion has been noted in other metal/ceramic interfaces<sup>12</sup> and could be analyzed phenomenologically using conventional expressions between crack velocity  $\dot{a}$  and energy release rate  $G$ .<sup>10</sup> However, appreciable additional research is needed to understand the underlying mechanism.

## APPENDIX

### PRELIMINARY ANALYSIS OF PLASTIC DISSIPATION IN STEADY-STATE\*

The basic features associated with plastic dissipation can be explored by considering the behavior of strips,  $dy$ , within the metal layer (Fig. A1). The dissipation within each layer,  $dW_p$ , is

$$dW_p \approx \tau_o \gamma_p dy \quad (A1)$$

where  $\tau_o$  is the shear yield strength and  $\gamma_p$  is the maximum plastic strain experienced within that element. In steady-state, the strain associated with the growing crack has an analytic form of the type<sup>9</sup>

$$\gamma_p \approx \gamma_o \ln(\alpha h/y) \quad (A2)$$

where  $\gamma_o$  is the yield strain and  $\alpha$  is an unknown coefficient. Integration of Eqn. (A1) over the metal layer gives;

$$\begin{aligned} W_p &= \int_0^h \tau_o \gamma_o \ln(\alpha h/y) dy \\ &= \tau_o \gamma_o h [1 + \ln \alpha] \end{aligned} \quad (A3)$$

The magnitude of  $\alpha$  can now be extracted by appreciating that, for the growing crack within a plastically deforming medium, the energy release rate at the crack tip is zero<sup>9</sup> and consequently the energy release rate and  $W_p$  are identical,

---

\* The treatment used in this Appendix was suggested and developed by J. W. Hutchinson.

$$G_c = W_p \quad (A4)$$

Consequently, from Eqns. (3) and (4)

$$\ln \alpha = G_c / \tau_o \gamma_o h - 1 \quad (A5)$$

In an attempt to separate the plastic dissipation in the plastic zone,  $W_p$ , and the dissipation in the fracture process zone,  $G_o$ , the dissipation is reevaluated with a cut-off dimension  $\delta$ ,

$$W_p^* \equiv W_p - G_o = \int_{\delta}^h \tau_o \gamma_o \ln(\alpha h/y) dy \quad (A6)$$

Integration of Eqn. (A6) with  $\alpha$  given by Eqn. (A5) gives

$$W_p^* = G_o \left( \frac{h}{\delta} - 1 \right) - h \tau_o \gamma_o \ln(h/\delta) \quad (A7)$$

Then, for small  $\delta/h$  and for the typical case,

$$G_o \tau_o \gamma_o \delta \gg \ln(h/\delta),$$

Eqn. (A7) reduces to

$$W_p^* \approx G_o (h/\delta)$$

This result is used in the text to provide an initial estimate of the plastic dissipation.

## REFERENCES

- [1] A. G. Evans, B. J. Dalgleish, P. G. Charalambides and M. Rühle, *Met. Trans*, in press.
- [2] R. M. Cannon, R. M. Fisher and A. G. Evans, *MRS Proceedings*, Vol. 54 (1986) p. 799.
- [3] B. J. Dalgleish, M. C. Lu and A. G. Evans, *Acta metall*, **36** No. 8 (1988) 2029.
- [4] C. F. Shih and R. J. Asaro, *Jnl. Appl. Mech.*, **55** (1988) 312.
- [5] C. F. Shih, R. J. Asaro and N. P. O'Dowd, *Metal/Ceramic Interfaces* (Eds., M. Rühle and A. G. Evans), Pergamon, in press.
- [6] P. G. Charalambides, J. Lund, R. M. McMeeking and A. G. Evans, *Jnl. Appl. Mech.*, **111** (1989) 77.
- [7] R. A. Hoover, *Journal of Physics E: Scientific Instruments*, 1971 Volume 4, p. 747.
- [8] B. J. Dalgleish, K. P. Trumble and A. G. Evans, *Acta metall.*, **37** (1989) 1923.
- [9] J. W. Hutchinson, *Non-Linear Fracture Mechanics*, Technical University of Denmark Monograph, 1979.
- [10] S. M. Wiederhorn, *Fracture Mechanics of Ceramics*, (Ed. R. C. Bradt et al.) Plenum, NY, Vol. 4 (1977) p. 549.
- [11] Z. Suo and J. W. Hutchinson, to be published.
- [12] T. S. Oh, J. Rödel, R. M. Cannon and R. O. Ritchie, *Acta metall.*, **36** (1988) 2083.

## FIGURE CAPTIONS

- Fig. 1. (a) The evolution of interface voids observed during diffusion bonding at 1040°C  
(b) Scanning electron micrograph of residual interface voids observed on the gold surface after fracture: slip steps formed during fracture are also visible
- Fig. 2. a) A precracked specimen viewed through the sapphire layer revealing the symmetrical cracks at the interface (specimen unloaded)  
b) Also visible at higher magnification is the faceted nature of the apparent (closure) crack front and the residual opening around voids ahead of the crack
- Fig. 3. A schematic of the test fixture used for *in situ* measurements of crack growth of the interface
- Fig. 4. Sequences of crack front profiles that illustrate the intermittent nature of crack extension at two different  $G$  levels
- Fig. 5. Load, deflection characteristics associated with precracking during three-point bending. The crack arrest load,  $P_a$ , is used to estimate  $G_c$ .
- Fig. 6. Optical view through the sapphire of blunting steps formed upon load changes and of the featureless surface formed upon uniform, slow crack growth
- Fig. 7. a) A crack front following slow crack growth at  $G \approx 20 \text{ Jm}^{-2}$ . A slip step (arrowed) is also visible (specimen loaded).  
b) After unloading, closure occurs over  $\sim 100 \mu\text{m}$ , but the original crack front is also still visible
- Fig. 8. a) Channeling patterns obtained on a gold surface revealing the (001) orientation  
b) A view of the sub-grains in the gold obtained in the SEM

- Fig. 9. Profilometer measurements on the Au fracture surface
- a) An optical view of a plastic trough passing over a blunting step
  - b) A profilometer amplitude trace over blunting steps
- Fig. 10. a) An electron damage line across an interface void, tilted to determine the void profile
- b) Schematic of the approach used to estimate the work of adhesion,  $W_{ad}$
- Fig. 11. a) An atomic resolution image of the interface
- b) A conventional TEM view revealing interface non-planarity
- Fig. 12. A fracture surface of a ductile interface fracture between  $Al_2O_3$  and Al
- Fig. A1. Trends in the non-dimensional plastic dissipation density with distance from the crack plane,  $y$



# Pore Removal in Diffusion Bonding

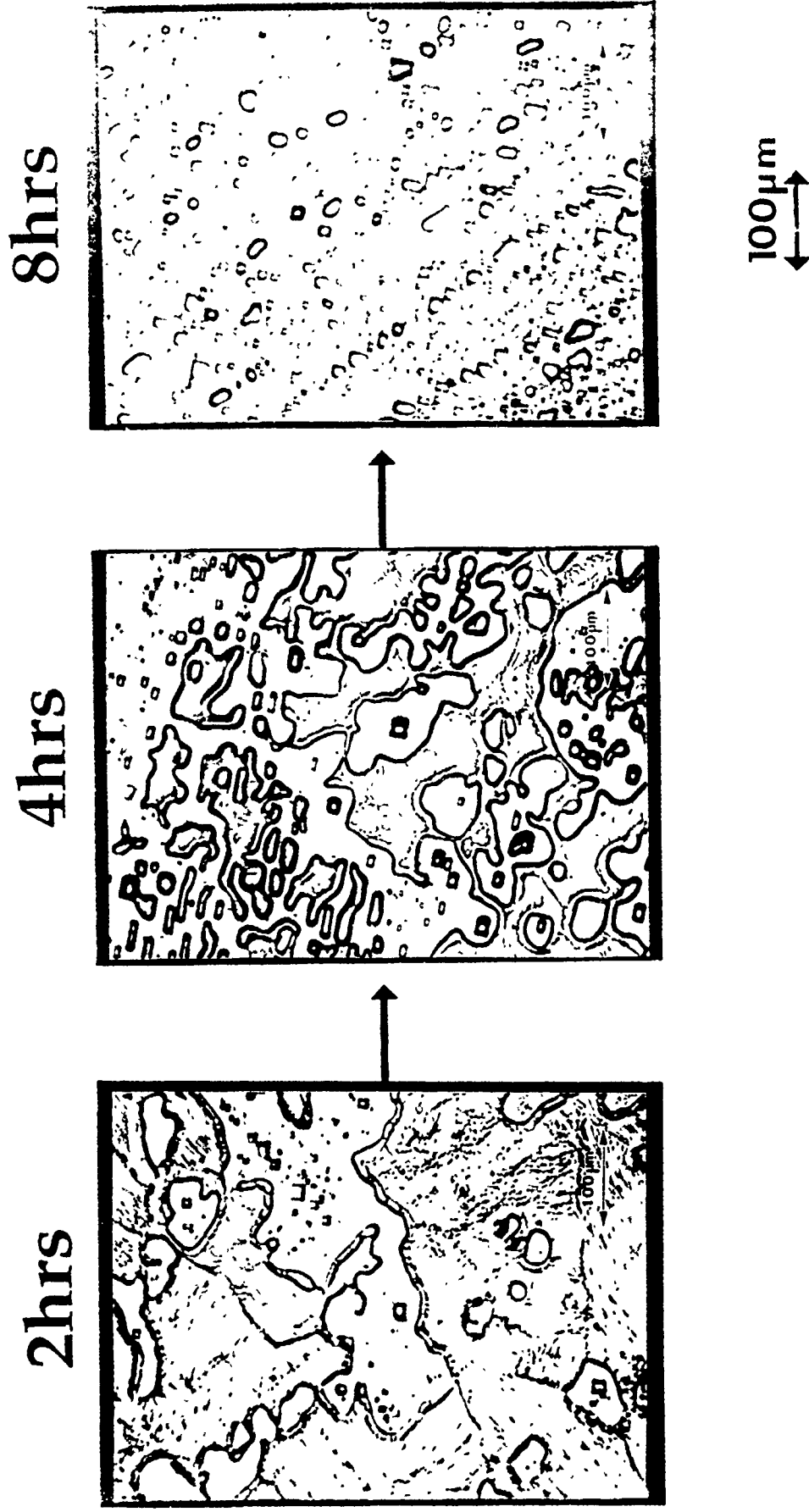


Fig. 1a

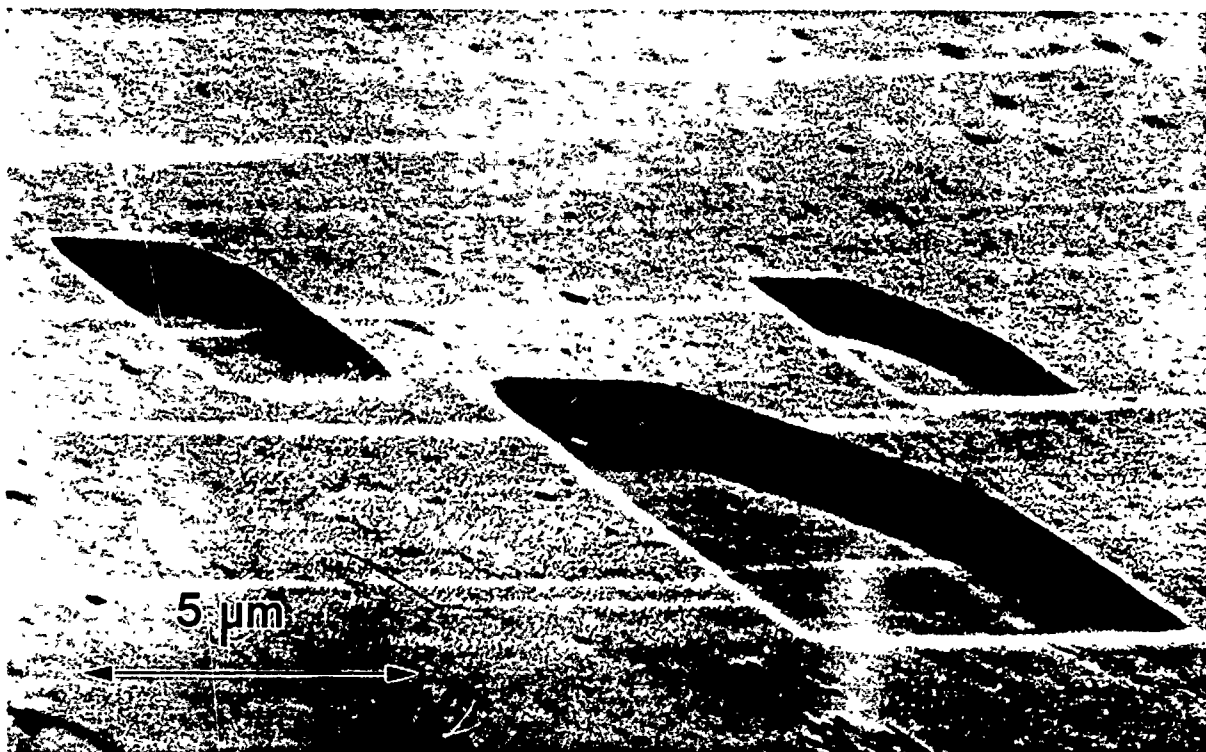
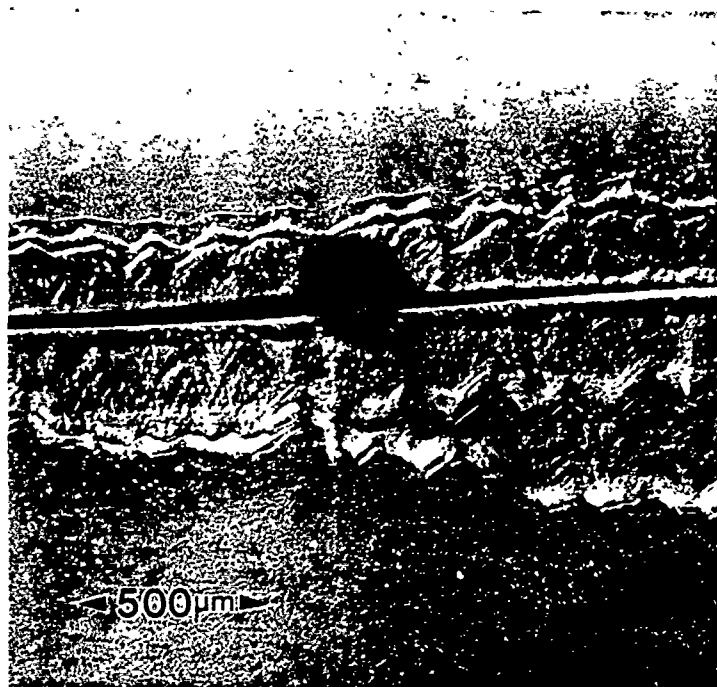


Fig. 1b



2a



2b

Fig. 2

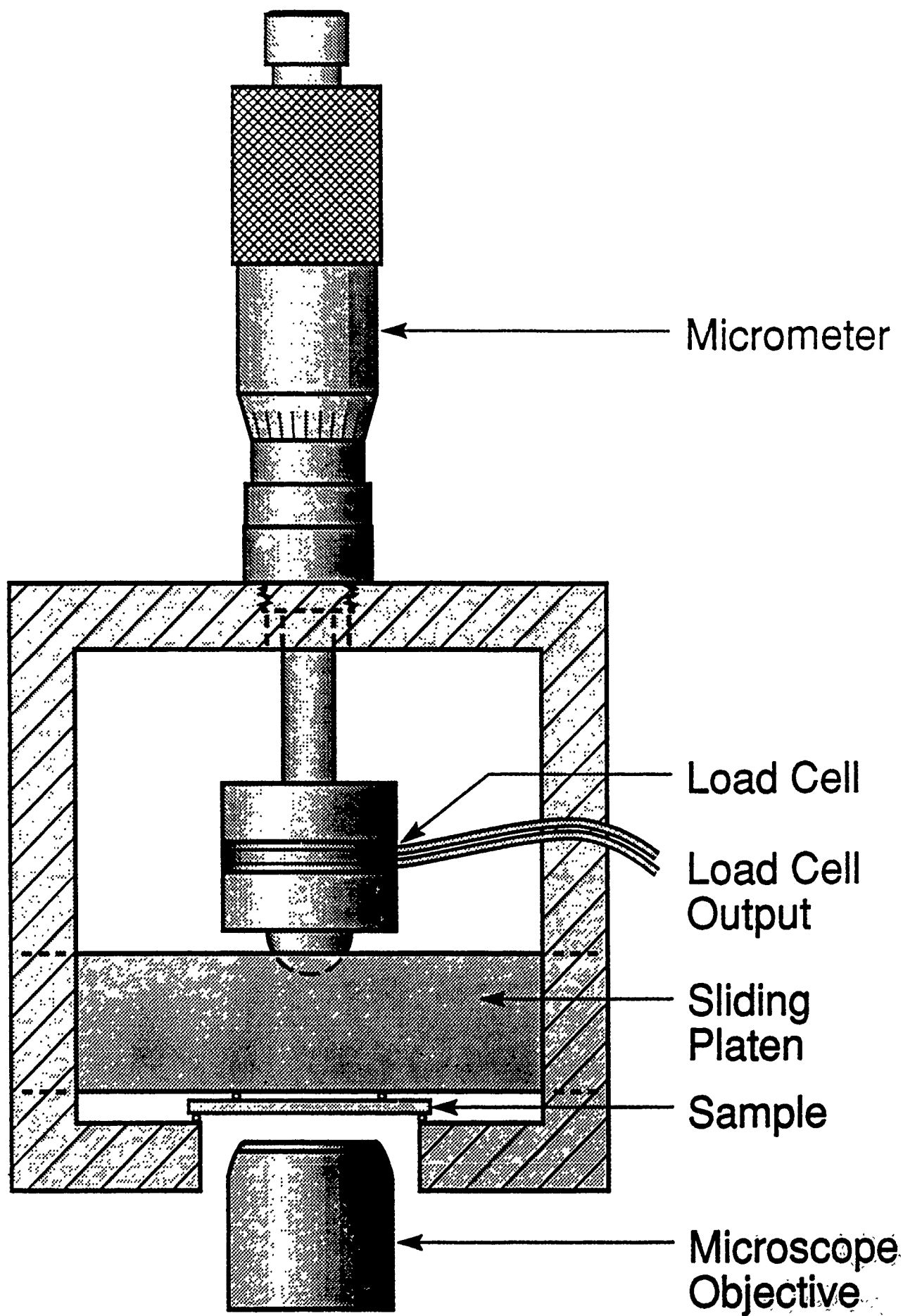


Fig. 3

# CRACK FRONT PROFILES

20 Second contour intervals

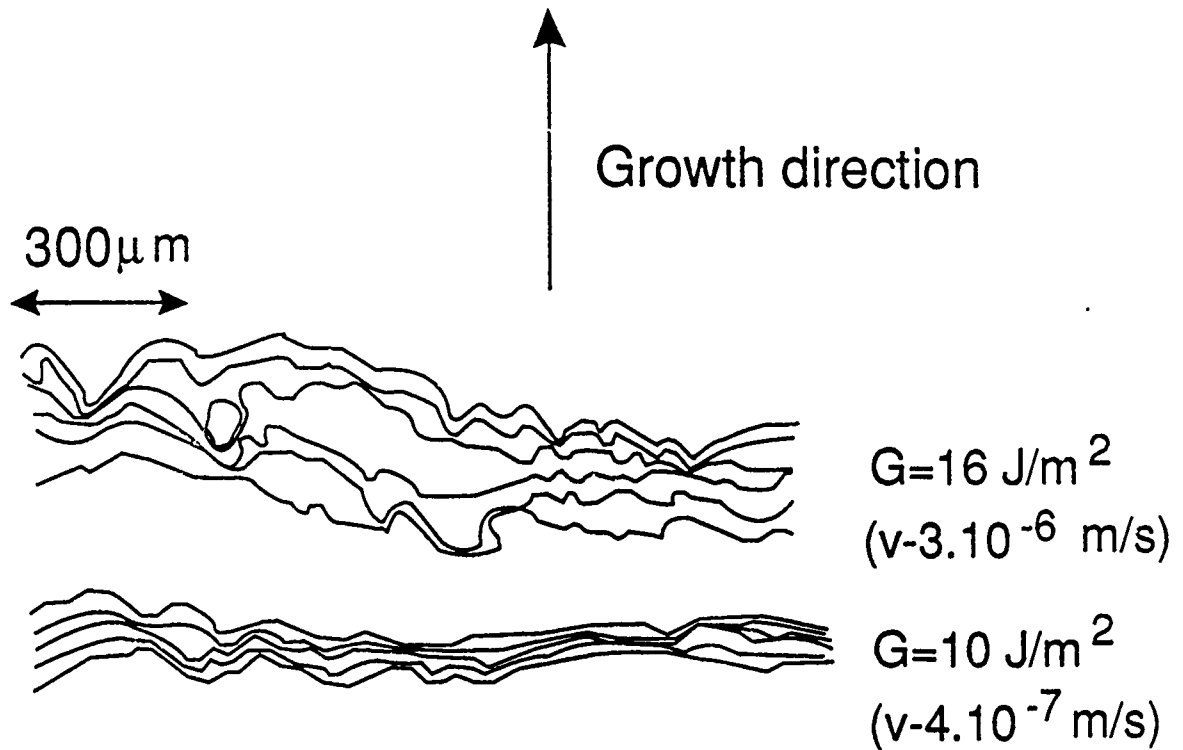


Fig. 4

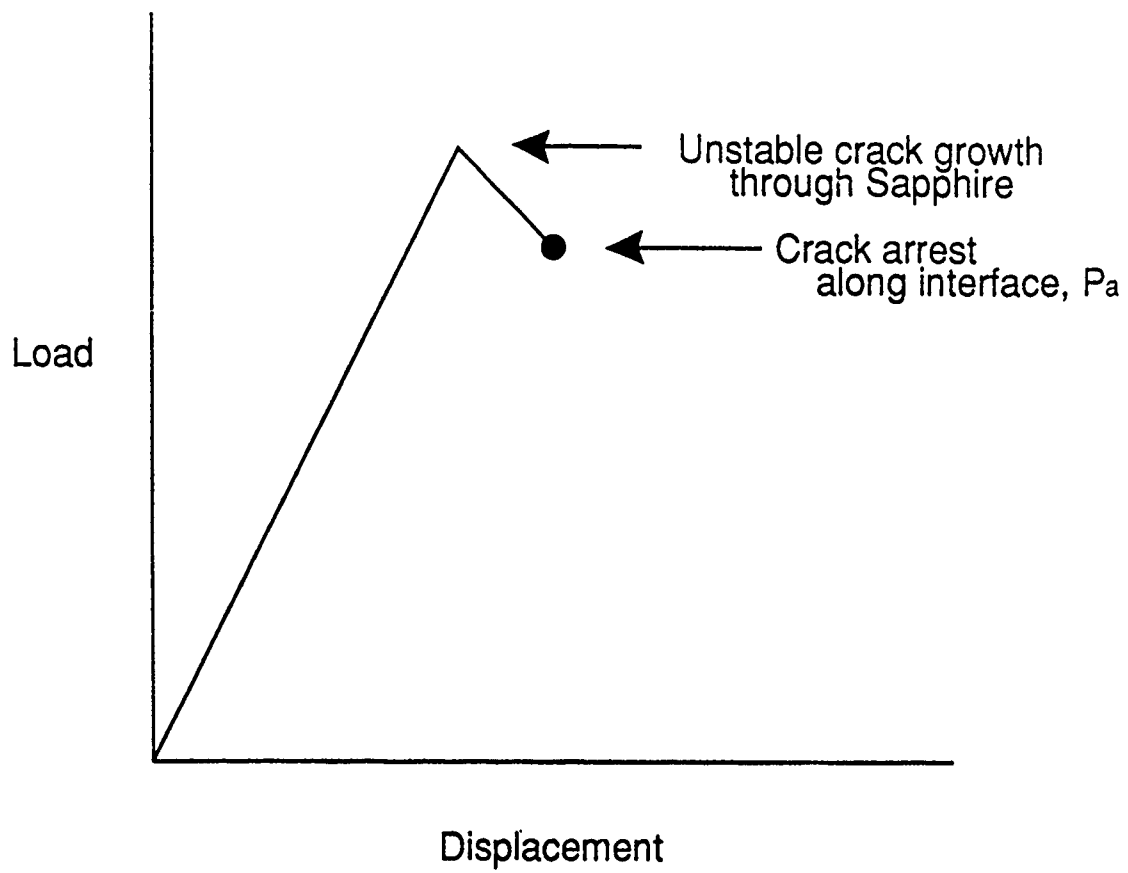


Fig. 5

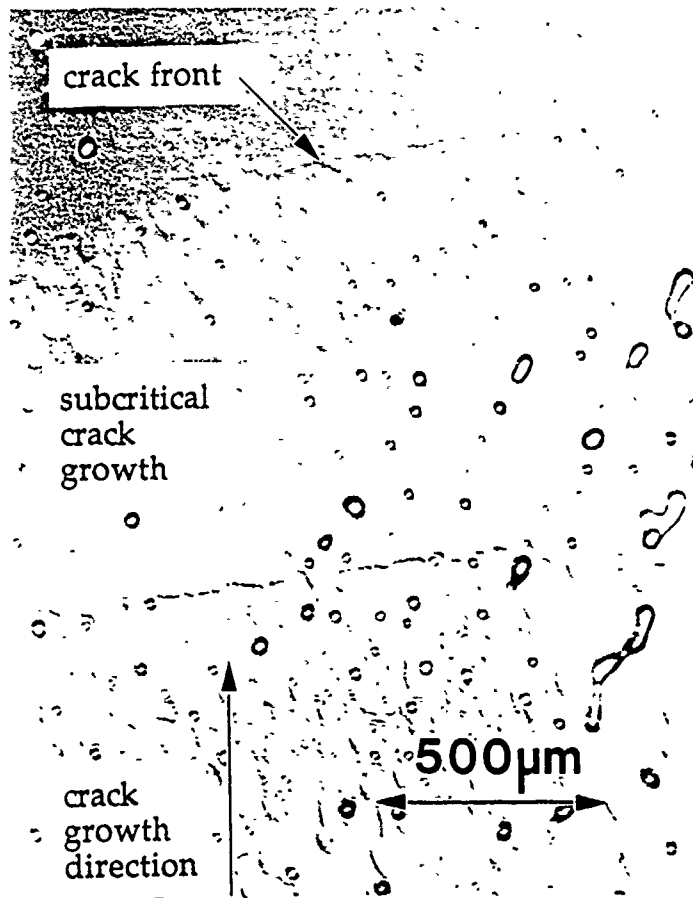
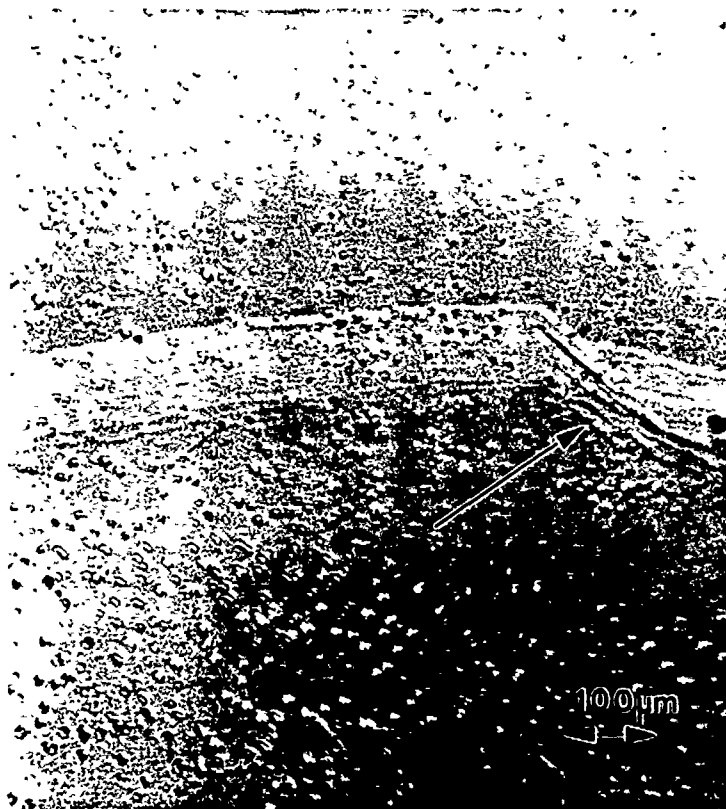


Fig. 6

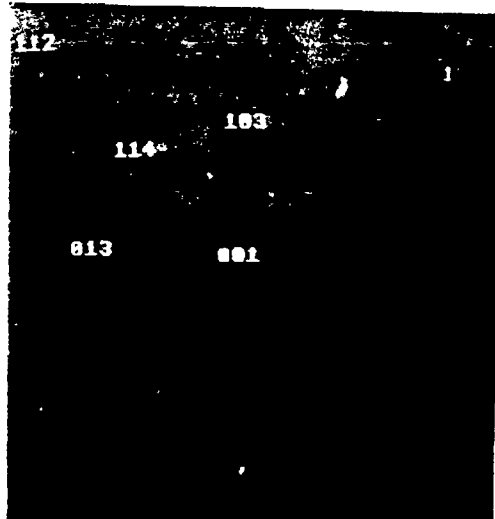


7a

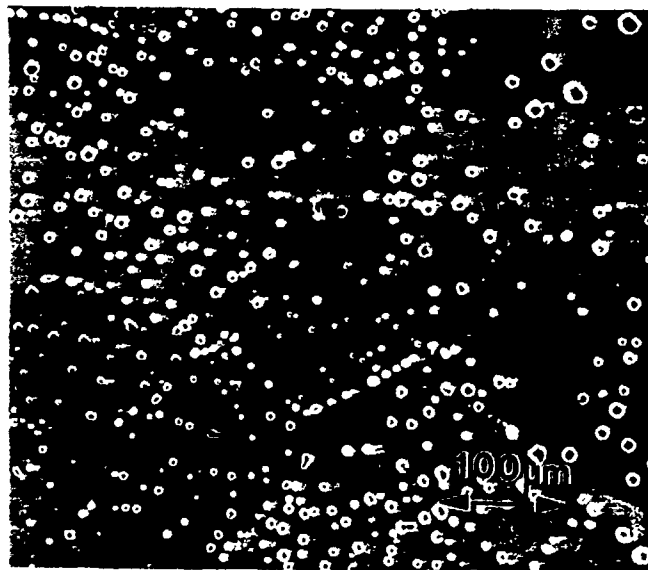


7b





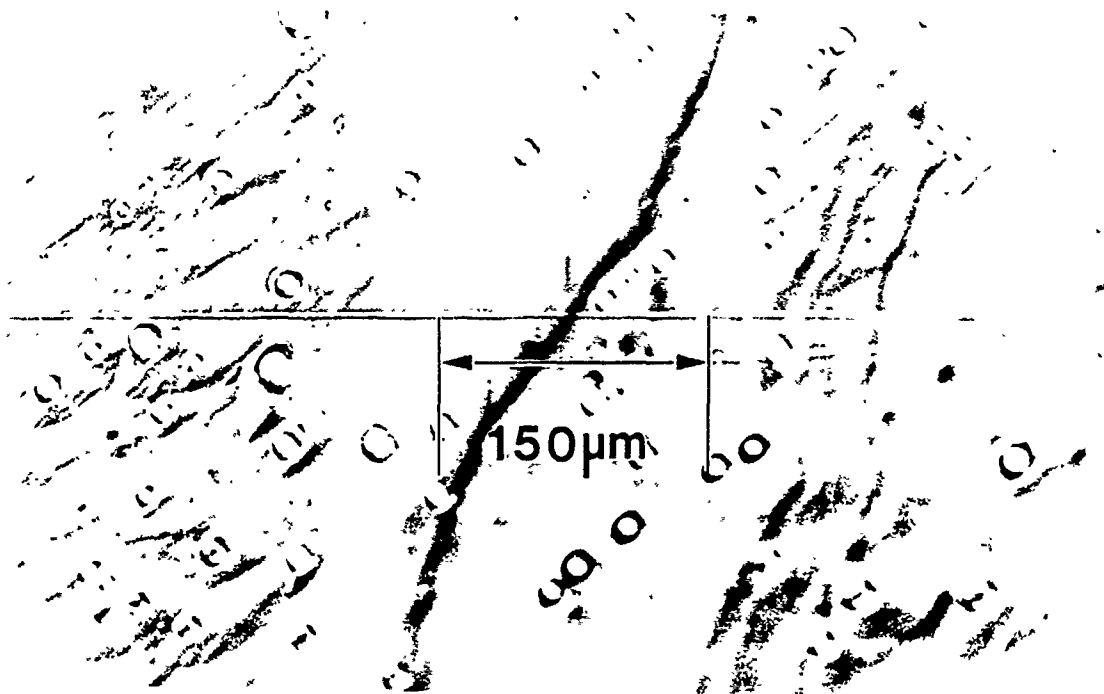
8a



8b

Fig. 8

← Direction of crack propagation



9a

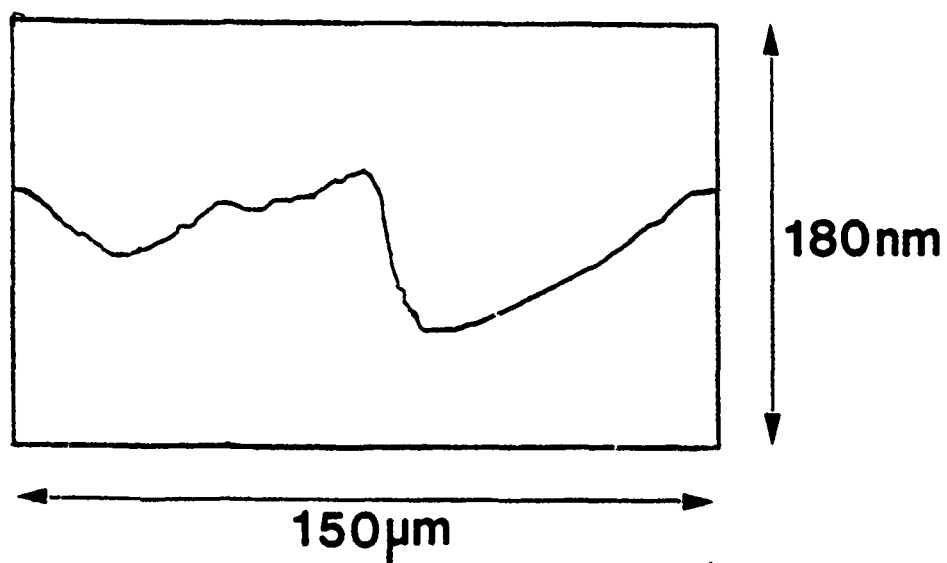
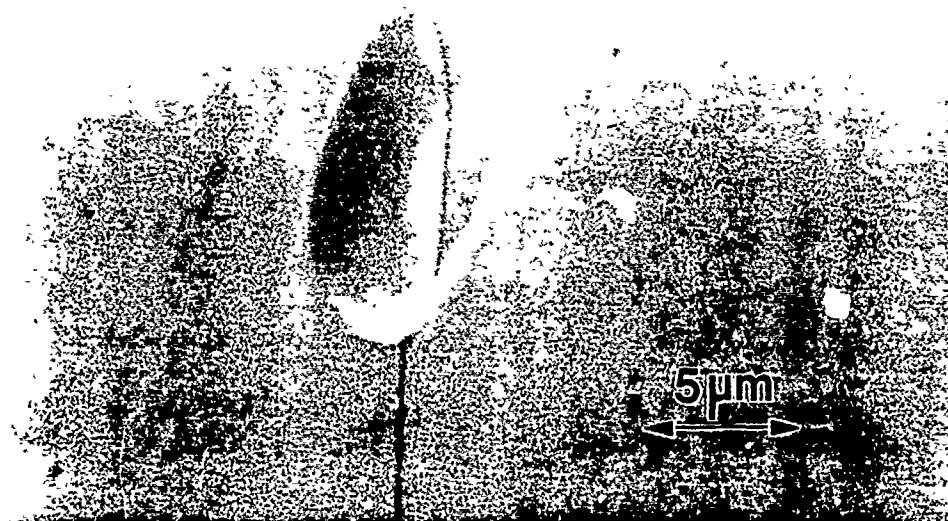


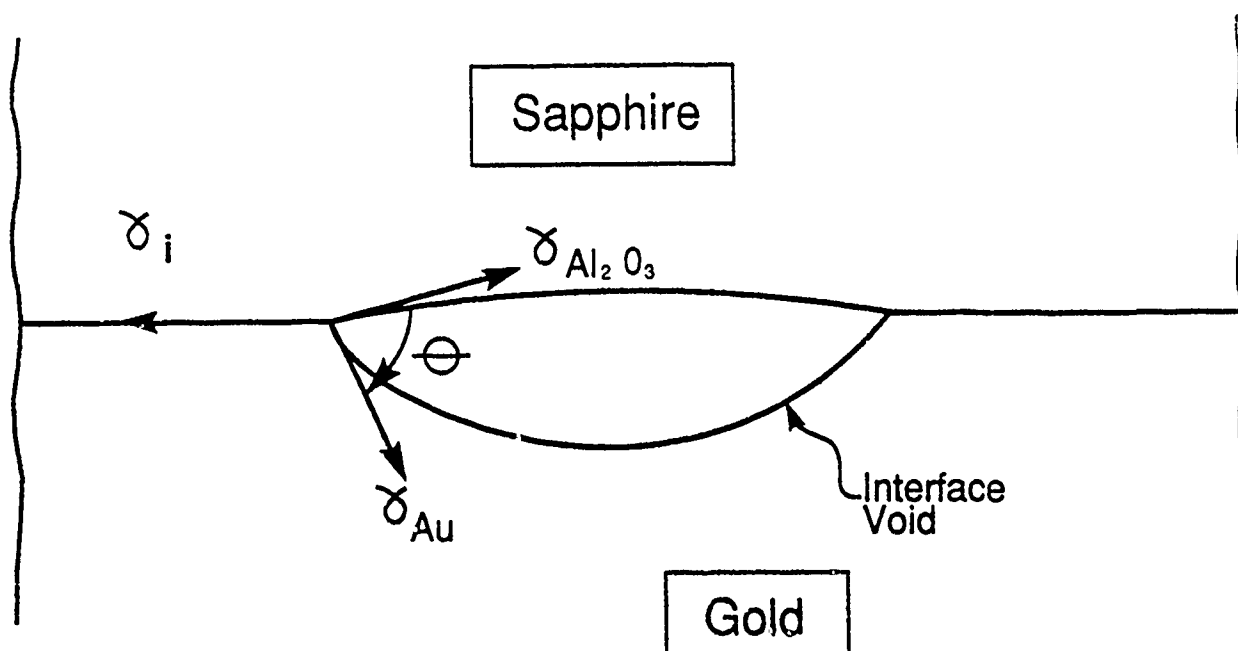
Fig. 9

9b



10a

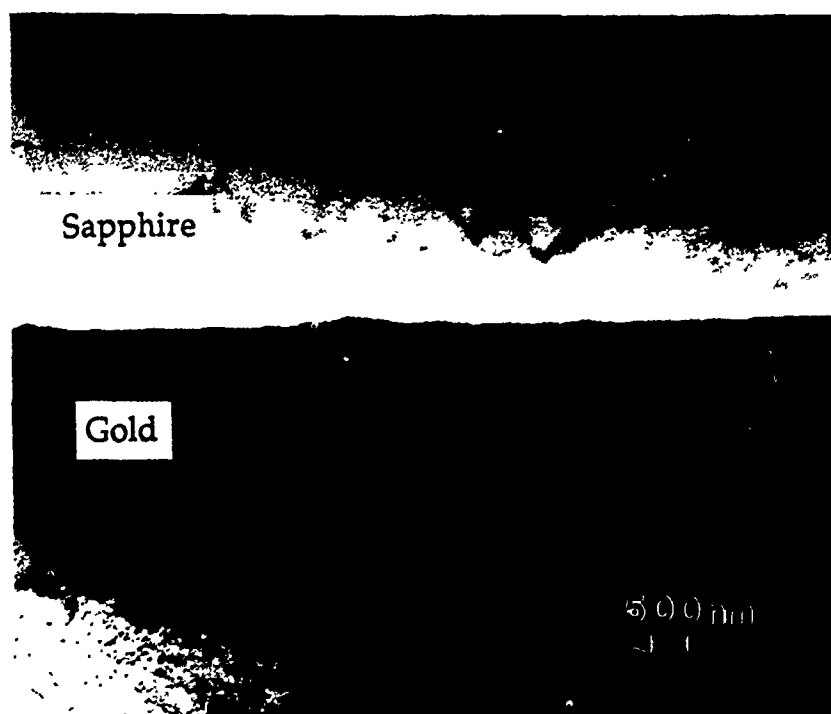
Fig. 10



$$\begin{aligned}\gamma_i &\approx \gamma_{\text{Al}_2\text{O}_3} + \gamma_{\text{Au}} \cos \theta \\ W_{\text{ad}} &= \gamma_{\text{Au}} + \gamma_{\text{Al}_2\text{O}_3} - \gamma_i \\ &\approx \gamma_{\text{Au}} (1 - \cos \theta)\end{aligned}$$



11a



11b

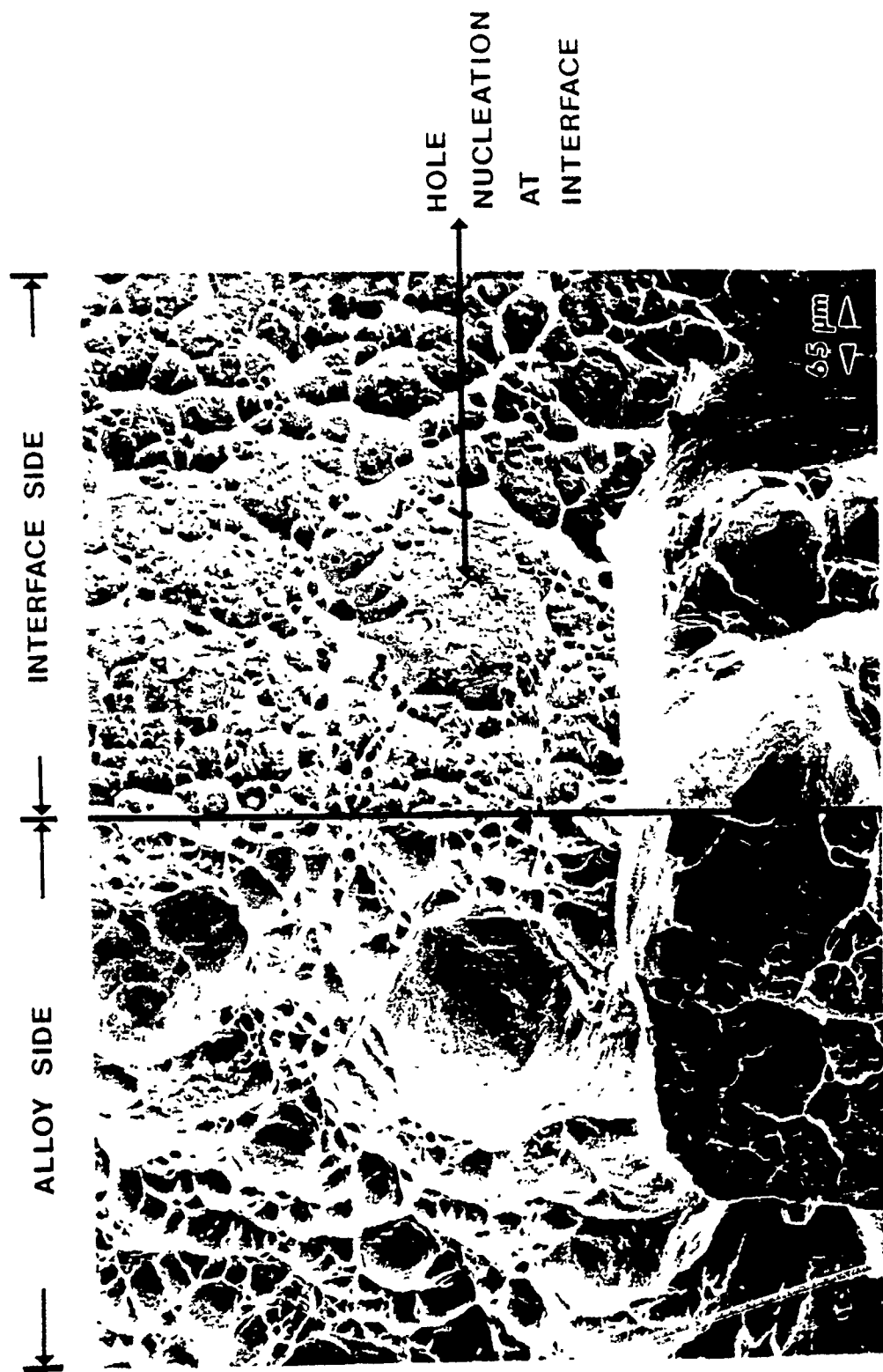


Fig. 12

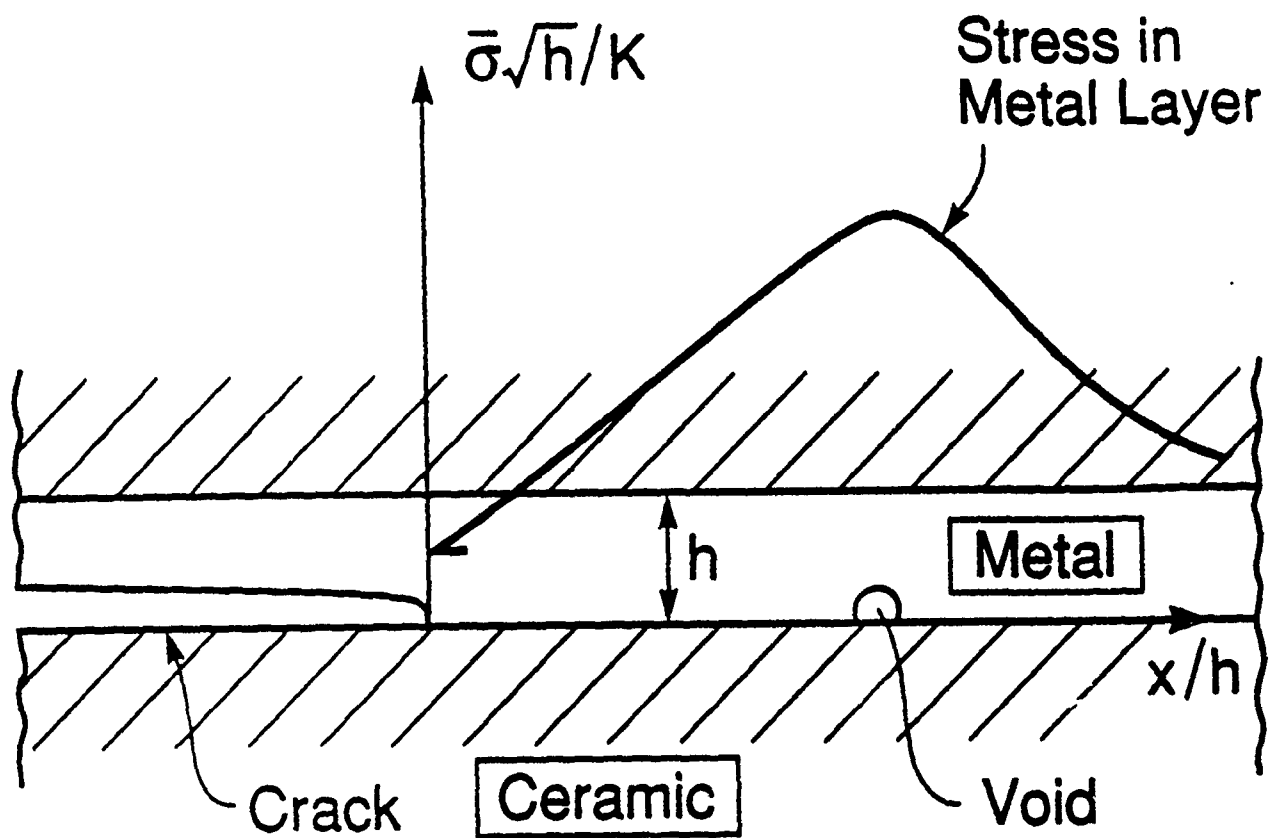


Fig. A1